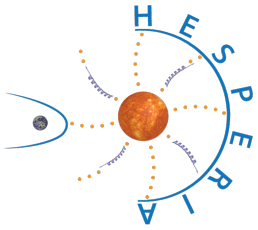

High Energy Solar Particle Events foRecastIng and Analysis
HESPERIA

Deliverable 3.1

Delivery Report of simulation modelling for Fermi/LAT events

EU's Horizon 2020 Research and Innovation Programme

Grant Agreement No. 637324

Start of the Project: 1st May 2015

Project Duration: 2 years

Coordinator: Olga E. Malandraki (NOA)

UNIVERSITAT DE BARCELONA

l'Observatoire de Paris

Lead Beneficiary	University of Turku (UTU)
Authors	Alexandr Afanasiev, Angels Aran, Rami Vainio, Alexis Rouillard, Pietro Zucca, Suvi Barcewicz, Robert Siipola, Blai Sanahuja, and Olga Malandraki

Work Package	WP 3: Modelling of shock-accelerated gamma-ray events
Task	Task 3.4
Deliverable	D3.1
Date for Deliverable: Month, Year	October, 2016

Change Log				
Version	**Date**	**Author(s)**	**Reason for Modification**	**Status**
1	12 Nov 2016	A. Afanasiev, A. Aran, R. Vainio, A. Rouillard, P. Zucca, S. Barcewicz, R. Siipola, B. Sanahuja, & O. Malandraki	N/A	Submitted
2				

Dissemination Level	
Public	X
Confidential, only for members of the consortium (including the Commission Services)	

Contents

List of Figures

List of Acronyms

2D 2-Dimensional

3D 3-Dimensional

CfA Center for Astrophysics

CME Coronal Mass Ejection

cobpoint Connecting with the OBserver POINT

CSA Coronal Shock Acceleration

DSP DownStream Propagation

ESA European Space Agency

ESP Energetic Storm Particle

EUV Extreme UltraViolet

GLE Ground Level Enhancement

GSE Geocentric Solar Ecliptic

HEEQ Heliocentric Earth Equatorial coordinate system

HESPERIA High Energy Solar Particle Events foRecastIng and Analysis

HMI Helioseismic and Magnetic Imaging

ICME Interplanetary Coronal Mass Ejection

IP InterPlanetary

LAT Large Area Telescope

MHD MagnetoHydroDynamics

PFSS Potential Field Source Surface

RTN Radial Tangential Normal

SaP Shock and Particle

SEP Solar Energetic Particle

SEPEM Solar Energetic Particle Environment Modelling

SDE Stochastic Differential Equation

SDO Solar Dynamics Observatory

SOHO Solar and Heliospheric Observatory

SOLPENCO SOlar Particle ENgineering COde

SPACECAST Protecting SPACE assets from high energy particles by developing European dynamic modelling and foreCASTing capabilities

STEREO Solar-Terrestrial Relation Observatory

WKB Wentzel-Kramers-Brillouin

WP Work Package

EXECUTIVE SUMMARY

This report describes the efforts performed in HESPERIA Work Package (WP) 3 to model the Fermi/LAT long-duration pion-decay gamma-ray events starting from the assumption that they are produced by very energetic protons accelerated at coronal/interplanetary shock waves driven by fast coronal mass ejections (CMEs). We employ three different simulation codes in the WP:

- The Shock-and-Particle (SaP) code of the University of Barcelona (UB), which is a combination of two models: a magnetohydrodynamic (MHD) model for CME-driven shock propagation and a focused transport model for interplanetary propagation of energetic particles injected at the shock;
- The Coronal Shock Acceleration (CSA) model of the University of Turku, which computes the coupled evolution of energetic particle distributions and Alfvén waves in a prescribed coronal/interplanetary shock; and
- A new DownStream Propagation (DSP) model, which is a Monte Carlo test-particle model following the diffusive transport of shock accelerated protons between the shock and the Sun, in the turbulent downstream region of the shock.

In addition, we make use of observations of coronal and interplanetary plasma to get the best possible global description of the evolution of the CME-driven shock.

Starting from the full list of HESPERIA Fermi/LAT events we made a downselection of events based on several observational criteria to arrive at two events, 23 January 2012 and 17 May 2012, which were analysed in detail. The first one of the events was a very long (6 hours) Fermi/LAT event but did not show increase of $>$500-MeV proton flux at 1 AU. The second one was a shorter Fermi/LAT event (2 hours), but showed also increases in several ground-based neutron monitors. (The only official ground-level enhancement of the present solar cycle.) In both events, the SaP simulations indicated that the fluxes observed at 1 AU would not immediately explain the Fermi/LAT events at the Sun, but a large fraction of protons producing gamma rays would actually be missing. The CMEs of both events were analysed to get empirical descriptions of shock dynamics, which were used as input to the CSA code. A large number of flux tubes (altogether ten) hosting shocks of different strength and magnetic geometry were simulated with CSA to obtain predictions for their ability to produce high-energy protons. It was discovered that even in a single global coronal shock, different regions may have very different particle acceleration properties. Therefore, it would be natural that the SaP prediction could fall short of the observed flux by Fermi/LAT, since the latter observes the proton flux (or their imprint in gamma rays) also in the most favourable flux tubes whereas the Earth-connected tube is but one of many and not necessarily hosting the best conditions of particle acceleration in the eruption. The CSA prediction of precipitating proton fluence was in both cases far more than enough to explain the gamma ray fluence observed by Fermi/LAT.

In conclusion, this study implies that shocks are a viable candidate to account for the protons producing pion-decay gamma-rays in long-duration solar events observed by Fermi/LAT. We, however, recognise the need for more model development especially in regard of accurate shock modelling and more detailed downstream transport before definitive conclusions can be made. This study provides an extremely encouraging result for the teams to perform this effort in the future.

1 Introduction

The novel gamma-ray observations by Large Area Telescope (LAT) on the Fermi Gamma-Ray Space Telescope spacecraft (Atwood et al. 2009), taken in a systematic way at unprecedentedly high energies, have presented a puzzle to the Solar Energetic Particle (SEP) research community. A fair number of long-duration high-energy (about 100-MeV) gamma-ray events have been observed, which have properties that challenge the traditional ideas that ions producing the gamma rays in the dense parts of the solar atmosphere are accelerated in flares (Ackermann et al. 2014). The Fermi/LAT observations indicate that particles are precipitating to the solar atmosphere for up to a day after the impulsive phase of the flare, which is very difficult to reconcile with a model of impulsive acceleration followed by trapping in the coronal magnetic field. On the other hand, we know that Coronal Mass Ejection (CME)-driven shock waves can emit SEPs accelerated up to hundreds of MeVs (in the extreme cases) for hours or even a day after the onset of the associated solar eruption. Therefore, as an alternative view on the genesis of the long-duration gamma-ray events, coronal shock acceleration needs to be considered. One of the challenges of the shock-acceleration hypothesis is that the SEP events observed in connection with the Fermi/LAT gamma-ray events are not always very large, nor do they extend to very high energies when observed at 1 AU. Therefore, one of the key aspects to understand about these events is the spatial distribution of the accelerated particles at the CME-driven shock wave as well as the relation between the interplanetary and interacting protons. Several things contribute to this relation: 1) In-situ observations are local, i.e., performed in a particular interplanetary flux tube, while high-energy gamma-ray observations are averaged over all field lines connected to the emission region. 2) Particle spectrum at the shock has to be transported to upstream and downstream to arrive at the fluxes of protons at the Sun and at 1 AU. 3) Particles can modify their own transport conditions upstream of the shock via streaming instabilities of Alfvén waves, so the fluxes observed at 1 AU can be partially decoupled from the fluxes at the shock. 4) Compressive and stochastic acceleration in the downstream region close to the CME can modify the precipitating spectrum.

We tackle the problem by conducting simulations of acceleration of protons in the shock and of their transport to 1 AU and back to the Sun for two long-duration gamma-ray events, one of which is associated with a Ground Level Enhancement (GLE) event and the other one is not. In what follows, we describe the events simulated in section 2. In section 3, we provide descriptions of the modelling techniques used, including those for shock modelling and for modelling of particle acceleration and transport. In section 4, we provide simulation results, and in section 5 discussion and conclusions.

2 Events simulated

2.1 Selection of FERMI/LAT events to be simulated

NOA provided a list of 24 high-energy gamma-ray sustained emission events as observed by FERMI/LAT related to solar events. The events dates and solar location are shown in the second and fourth columns of Table 1. A first down-selection for modeling was performed based on the SEP and EM data available during the first months of the project, i.e. in the period of June – October 2015. The selected events were: 7 March 2011 (number 1 in Table 1), 23 January 2012 (n. 6), 27 January 2012 (n. 7) and 17 May 2012 (n. 12). This latter event was finally chosen for modeling based on the synergies with WP4 since it is the GLE event number 71.

Next, we scanned this FERMI/LAT event list considering the events suitability for modeling with the SaP model. The criteria taken into account are the following:

1. That the available SEP data do not show large data gaps preventing the fitting of the intensity-time profiles and that the SEP event shows high-energy protons ($> 50\,\mathrm{MeV}$). Among available data

Table 1: List of Fermi/LAT events: selection/discarding for modeling with SaP

Number	Date, Location	Criteria	Number	Date, Location	Criteria
1	2011/03/07, N30W47	Selected	13	2012/06/03, N15E38	1
2	2011/06/07, S21W54	3	14	2012/07/06, S17W52	2
3	2011/08/04, N19W46	2	15	2013/04/11, N07E13	2
4	2011/09/06, N14W18	3	16	2013/05/13, N11E89	4
5	2011/09/07, N18W32	3	17	2013/05/13, N10E80	4
6	2012/01/23, N33W21	Selected	18	2013/05/14, N10E77	4
7	2012/01/27, N33W85	2	19	2013/05/15, N11E65	4
8	2012/03/05, N16E54	3	20	2013/10/11, N21E106	4
9	2012/03/07, N17E27	3	21	2013/10/25, S08E71	4
10	2012/03/09, N16W02	2	22	2013/10/28, S14E28	1
11	2012/03/10, N18W26	2	23	2014/02/25, N00E78	4
12	2012/05/17, N05W77	2	24	2014/09/01, N12E138	4

sets, it is preferable the use of the narrow-energy channels from the SOHO/ERNE data (Torsti et al. 1995); otherwise, the SEPEM reference data (Jiggens et al. 2012) available up to April 2013 offers the larger number of differential energy channels.

2. That the solar wind and interplanetary magnetic field measurements show time profiles in the upstream region of the SEP events as closer to the modeled Parker Spiral field and stable solar wind conditions as possible.

3. That a main solar source of the SEP event could be related with the observed IP shock at 1 AU, accounting for the continuous evolution of the intensity-time profiles of the observed solar energetic protons at the Earth.

4. That the solar source location is westward than E40, in order to avoid the less favorable eastern magnetic connections with the shock front early in the events, since this is more difficult for the 2D MHD shock propagation model used.

The third and sixth columns of Table 1 show the criterium that the event does not comply with; otherwise, the events are marked as 'Selected'. As can be seen, from these selection criteria 2 events were found the best candidates: 23 January 2012 and 7 March 2011 SEP events. We decided to model first, together with the GLE71 event, the 23 January 2012 based on the larger intensities reached, specially at high energies, with respect to the 7 March 2011 SEP event. The latter event was left as backup, but, constraints posed by working time and computational resources permit only two events to be studied in detail.

2.2 The 23 January 2012 SEP event

2.2.1 Particle and plasma data observations at near-Earth's orbit

The top panel of Figure 1 shows the SEP event on 23 January 2012 as seen by near-Earth spacecraft. Specifically, this panel displays: the 0.3 – 4.9 MeV differential ion intensities (coloured traces indicated in the legend) measured by the LEMS120 telescope and the 175 – 315 keV electron intensities (scaled to 10^{-5}, black curve) measured by the LEMS30 telescope of the ACE/EPAM instrument (Gold et al. 1998); and the 4.2 – 900 MeV differential proton intensities (coloured as indicated in the legend) measured by the GOES13/SEM/EPEAD detector (e.g. Sellers & Hanser 1996)[1]. For this particular event, the differential proton intensities of the SOHO/ERNE LED and HED detectors and of the SOHO/COSTEP/EPHIN detector showed large data gaps preventing the use of these data sets with the SaP model.

The next three panels of Figure 1 show, respectively in black, the solar wind speed, density and temperature as measured by the ACE/SWEPAM instrument (McComas et al. 1998) and in blue the solar wind speed and density measured by the WIND/SWE instrument (Ogilvie et al. 1995)[2]. The ACE/SWEPAM level-2 data presents a data gap through the whole upstream region and the immediate post-shock region of the SEP event. Finally, the three bottom panels show the solar wind magnetic field intensity, polar and azimuthal directions respectively. Black curves correspond to ACE/MAG[3] data (Smith et al. 1998) and blue curves to WIND/SWE data, both in Geocentric Solar Ecliptic (GSE) coordinates.

The vertical solid lines in Figure 1 indicate the passage of interplanetary shocks by WIND. After the shock arrival on day 22, the magnetic field data shows the passage of an interplanetary CME whose end coincides with the onset of the particle event. There is a clear rotation of the components of the IMF (see the panels of θ and ϕ angles) 2 hours after the onset of the particle event that may be affecting the propagation of the particles and the magnetic connection of the observer with the parent shock. After that, the magnetic field changes direction several times but the magnetic field strength keeps rather constant throughout the upstream region. The solar wind speed and density also show stable time profiles.

The IP shock associated with the SEP event arrives on day 24 at 14:40 UT, and the low-energy ion intensities measured by ACE/EPAM exhibit a nice ESP event, peaking at the shock passage. The low-energy channels (< 15 MeV) of GOES-13/EPEAD show a local peak coinciding with the shock arrival time at the Earth, 23.6 minutes later than the shock passage by WIND (information from the Havard-Smithsonian Center for Astrophysics (CfA) Interplanetary shock Database)[4]. This is indicated by the second vertical line shown in Figure 2, just after the shock passage by WIND.

The upstream region of the 2012 January 23rd SEP event, to be modeled with the SaP model, is shown with more detail in Figure 2. In this case we have plotted the proton intensities corresponding to the 10 channels of the SEPEM reference data set (Jiggens et al. 2012). These SEPEM data is based on the GOES/EPEAD data using the effective energy as the representative value of the wide differential channels of GOES, and cross-calibrated with corrected data from the IMP-8/GME instrument (Sandberg et al. 2014). We use this data instead of GOES original channels because it provides the proton intensities for a larger number of proton energies, which is better in order to reduce the freedom in choosing the values of the parameters in the model. Over-plotted are shown the proton intensities from the SOHO/COSTEP/EPHIN detector, which roughly compare with the SEPEM reference data set, if the geometric mean energy is considered as representative of the EPHIN wide energy windows.

Note that the first solid vertical line in Figure 2 does not indicate an IP shock passage but a change of

[1] ACE/EPAM data are 5 minute averages of level 2 data downloaded from the ACE Science Centre (http://www.srl.caltech.edu/ACE/ASC/) and the GOES13/EPEAD data are 5 minutes averages downloaded from the SEPEM application server (http://dev.sepem.oma.be/).

[2] 92-seconds averages from omniweb.gsfc.nasa.gov/ftpbrowser/wind_swe_2m.html

[3] ACE SWEPAM and MAG data correspond to the 64-seconds average merged data set available from the ACE Science Centre.

[4] url: https://www.cfa.harvard.edu/shocks/wi_data/00512/wi_00512.html

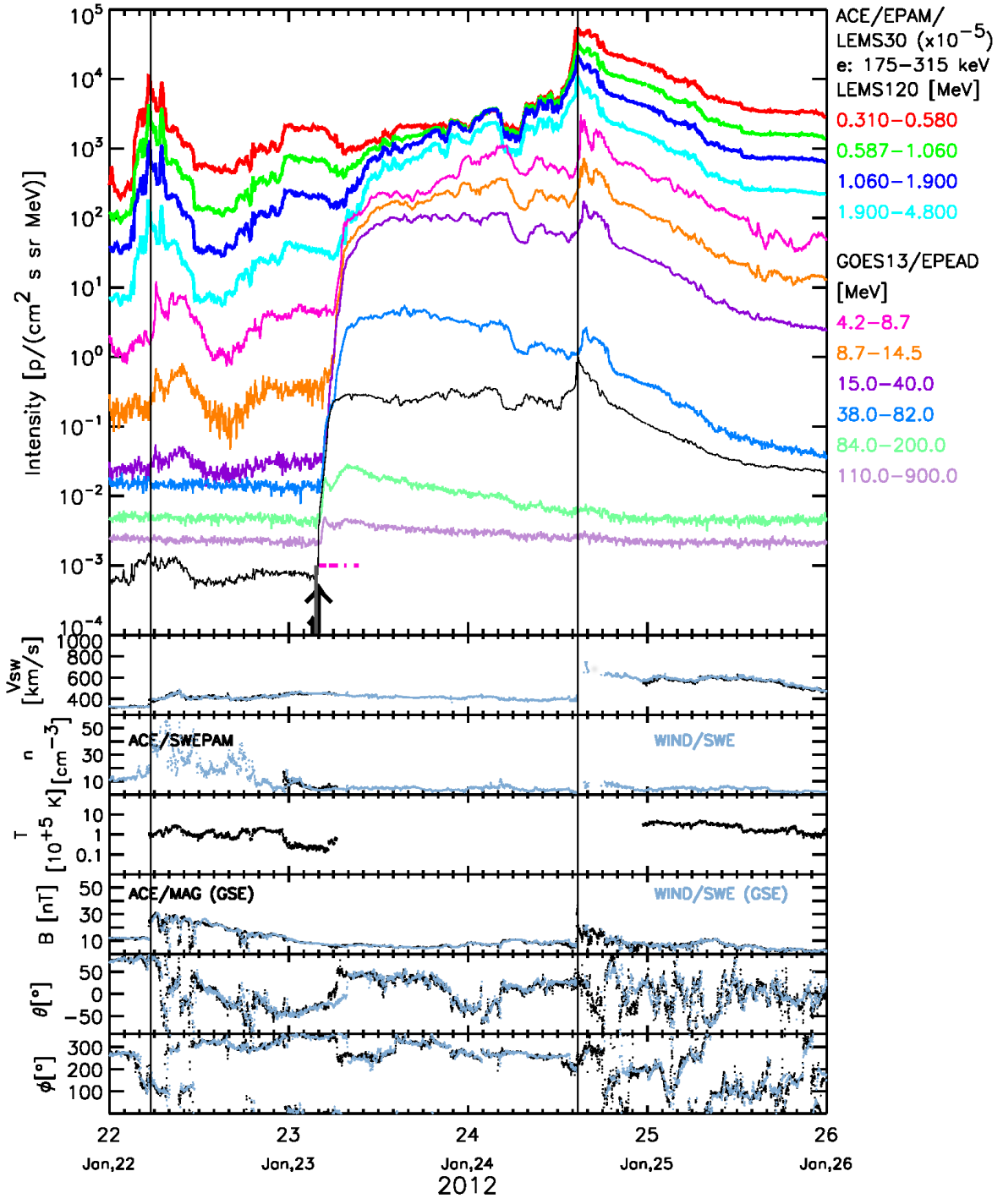

Figure 1: 2012 January 23 SEP event as seen at near-Earth environment. Particle intensities and solar wind data come from different spacecraft, as specified in the insets.

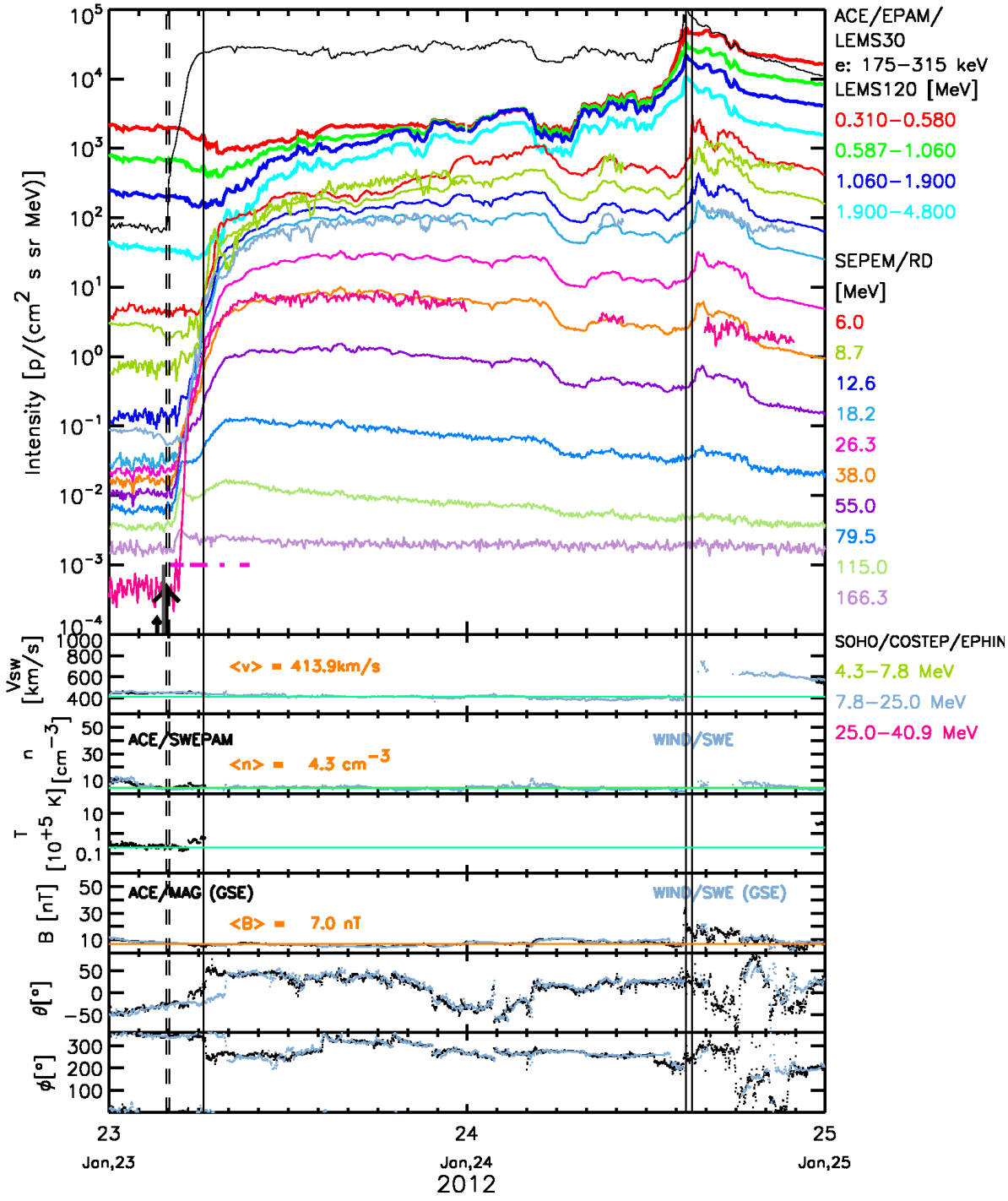

Figure 2: 2012 January 23 SEP event as seen at near-Earth environment. Particle intensities and solar wind data come from different spacecraft, as specified in the insets.

magnetic flux tube (with rotations in both polar and azimuthal angles). In the solar wind and magnetic field intensity (i.e. $|B|$) panels, the horizontal lines mark the mean values in the upstream region. These are the 'target' values for the simulation of the solar wind with the 2D MHD model (Pomoell et al. 2015).

2.2.2 Solar sources

A Halo CME with a 'plane-of-sky' speed of 2175 km s^{-1} was first seen by the SOHO/LASCO/C2 coronagraph at 04:05 UT on the 23rd of January. According to the NASA's SOHO/LASCO CME catalog (http://cdaw.gsfc.nasa.gov/CME_list/), this CME comes from northern latitudes. Based on a extrapolation from the height-time plot, at 03:50 UT the CME was at a height of ∼1.75 $R_\odot$ (see http://cdaw.gsfc.nasa.gov/CME_list/UNIVERSAL/2012_01/htpng/20120123.040005.p326g.htp.html). A slow (684 km s^{-1}) partial Halo CME first detected at 03:12 UT from the same region was rapidly intercepted by the Halo CME, as can be seen in the middle panel of Figure 3. The Halo/partial CME onset times are indicated by big/small arrows in Figures 1 and 2. From the combined images from LASCO and COR1 of STEREO available from the same CME catalog, one can see that the Halo CME shock initially evolves within the closed-loops from the previous CME; this might explain the low intensities of high-energy protons recorded at 1 AU.

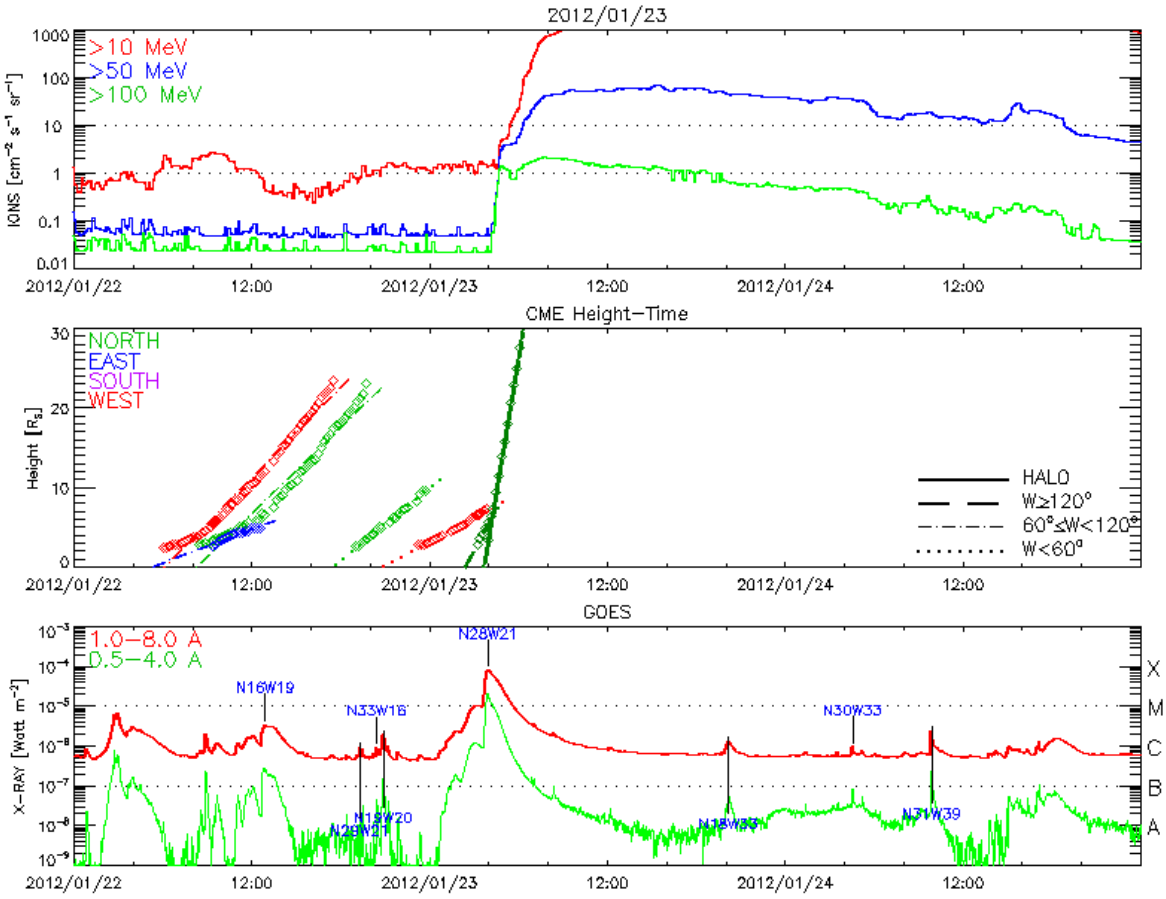

Figure 3: GOES proton integral channels, height-time plot of the CMEs positions from 22 - 24 January 2012 and Soft X-ray emission. Taken from http://cdaw.gsfc.nasa.gov/CME_list/

Temporally associated with these CME eruptions, an X-ray flare was observed from N33W21[5]. The X-ray emission onset was at 03:38 UT on the 23rd (indicated by a grey short vertical line in Figures 1 and 2) and peaked at 03:59 UT with an intensity of M8.7. As can be seen in Figure 3, the X-ray emission reached the M1.0 level at the time of the eruption of the partial halo CME.

The reason to choose this SEP event for modeling was the detection γ-ray emission. Pink horizontal lines in Figures 1 and 2 indicate the times of γ-ray detection by Fermi/LAT (Ackermann et al. 2014).

For the simulation of the SEP event, we will assume that the main source of particles is the shock associated with the Halo CME, with a starting time for the shock propagation at 03:50 UT on day 23. On the other hand, we will consider that the modeling of the SEP propagation starts at the time of the onset of the flare, 12 minutes earlier, 0.2 hours, in order to not rule out the possibility that a small portion of observed particles could come from any solar-fixed source directly.

2.2.3 Low-energy proton anisotropies from ACE/EPAM

External contributor: D. Lario from JHU/APL

Figure 4 shows the isotropic, first order and second order anisotropies obtained for the ion channel of the ACE/EPAM LEMS120 and LEMS30 telescopes (Gold et al. 1998). The computation of the spherical harmonics expansion of the proton distribution function has been performed by Dr. David Lario. A description of the method followed can be found in Sanderson et al. (1985) and Lario et al. (2004).

Assumptions made in the calculation of the particle anisotropies:

- In order to correct for the Compton-Getting effect, we have assumed that the ion intensities obtained by the ACE/EPAM telescopes are dominated by protons. This assumption is validated by many years of observations (Lario et al. 2004).
- In order to compute the proton spectra for the correction of the Compton-Getting effect, only the P6/P'6 to P8/P'8 channels have been considered. Lower-energy channels have been discarded because they are highly contaminated by electrons or they present high background noise.
- Due to the huge data gap in the level-2 solar wind velocity ACE/SWEPAM data (see Figure 1), we have used 92 s averages of the solar wind speed from WIND/SWE. The solar wind speed is given in GSE coordinates, but to transform the data into a frame moving with the solar wind we need the components for the ACE spacecraft (S/C) reference system. Since this information is not available (at least, presently, to us) we have assumed that the solar wind speed is parallel to the X-axis of the S/C coordinate system. Depending on the S/C orientation, this assumption could be not valid.
- To compute the spherical harmonics, we define a coordinate system with the z-axis along the instantaneous IMF direction. For this purpose, we have used level-2 magnetic field vector data, in the ACE S/C reference system, provided by Dr. Olga Malandraki.

In the top panel of Figure 4 we can see the isotropic component, A0 (black curve) for 1.90 – 4.80 MeV protons, compared with the corresponding sector-averaged intensity measured by the ACE/EPAM/LEMS 120 telescope (coloured curve). The two following panels show the first-order harmonic components. In the solar wind frame, the A1/A0 is the parallel (to the IMF) first-order anisotropy. The sign of A1 is defined with respect to the IMF direction. $A_{\perp}$/A0 represent the two (red/blue) first-order components

[5]This position is taken from http://www.lmsal.com/solarsoft/last_events_20120123_2332/gev_20120123_0338.html, based on SECCHI/EUVI beacon data, and corroborated by an image from SDO/AIA. Note that the flare site is N18W25 according to the goes-xray-report_2012-processed.txt file from the NOAA ftp server, which looking the SDO/AIA image seems incorrect).

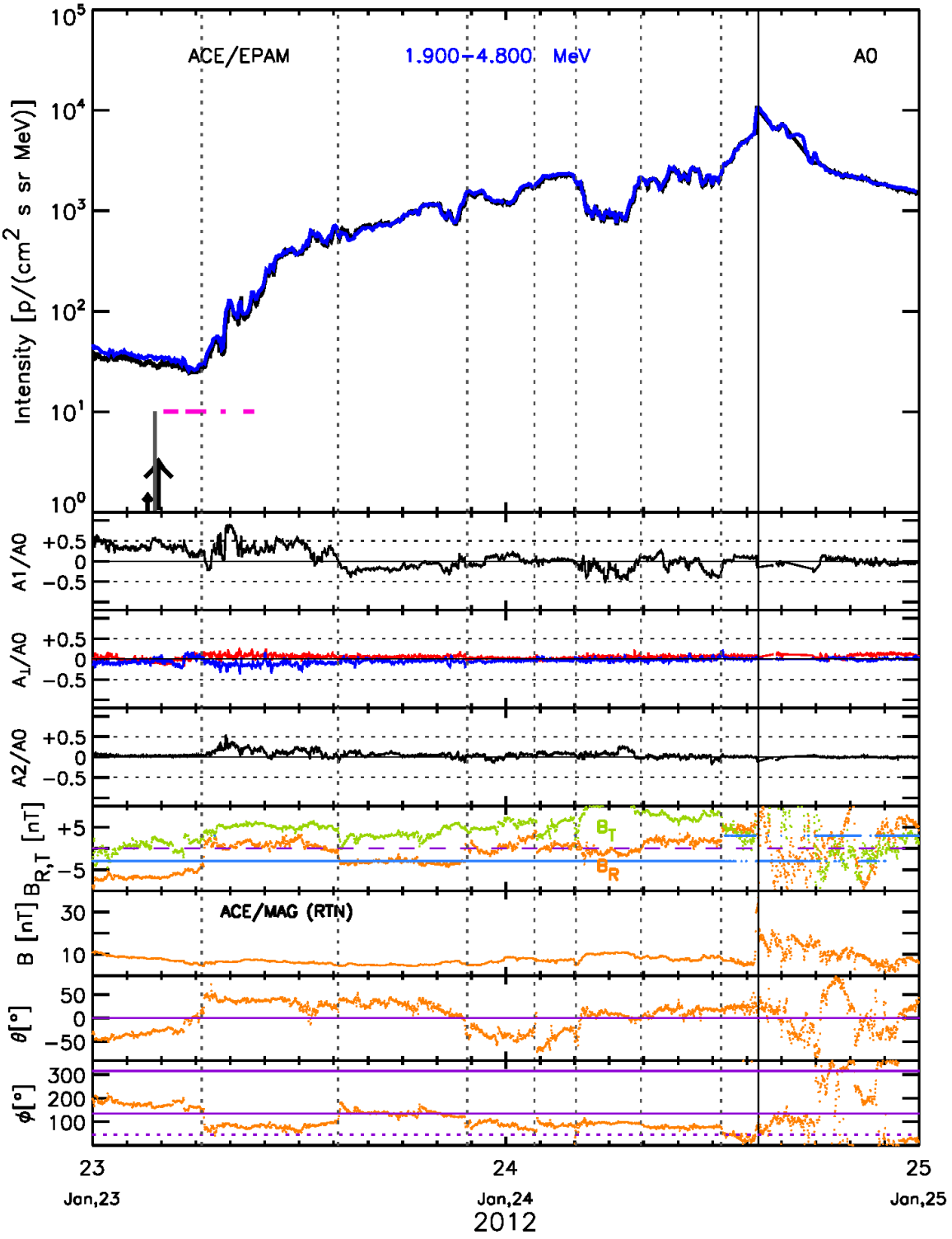

Figure 4: 2012 January 23 SEP event. 1.90−4.80 MeV proton intensity and anisotropies.

perpendicular to the IMF. The next panel shows the second-order harmonic distribution (A2/A0) computed assuming symmetry about the IMF. A positive ratio of A2/A0, when the first order coefficients are close to zero, represents bidirectional ion flows along the IMF.

The four bottom panels show, in the Radial Tangential Normal (RTN) reference frame, the radial (orange) and tangential (olive green) components of the magnetic field, the magnetic field strength, and the polar and azimuthal IMF directions. The blue line in the panel displaying the radial and tangential components shows the polarity sign of the magnetic field[6], which is mostly negative throughout the upstream region, with the exception of the period just prior to the arrival of the shock. The vertical solid line indicates the shock crossing by ACE. The big arrow indicates the first time the associated CME was detected by SOHO/LASCO/C2 and the grey thin bar indicates the onset of the 1 – 8 Å X-ray flare. As in previous plots, the pink horizontal lines indicate the times of γ-ray detection by Fermi/LAT (Ackermann et al. 2014).

As can be seen in the polar and azimuthal angles, the magnetic field changes direction several times during the upstream region of the event, and does not follow the Archimedean spiral topology assumed in the SaP model. These changes are indicated by vertical dotted lines. B_r has a low value (close to 0) in several intervals, indicating that the magnetic field is mostly perpendicular to the radial direction. In the A1/A0 panel we see that after the second dotted line, the flow is mostly anti-sunward. The odd orientation of the magnetic field throughout the upstream region of the event prevents a clear interpretation of the anisotropy data, and most likely, it is also limiting the pitch-angle range scanned by the LEMS telescopes.

Figure 5 shows the magnetic field strength and components in the ACE spacecraft reference frame. On the beginning of day 23, we can see that the magnetic field is still disturbed after the shock and ICME arriving in the first half of day 22nd. This may explain the odd behaviour of the anisotropy components at the beginning of the SEP event, where the perpendicular components are not negligible, and where the values of A1/A0 are rather small (as compared to the A1/A0 values determined at the onset of other events, e.g., 1979 April 24 and 1981 December 8 SEP events, Heras et al. 1995).

Taking into account all these observational difficulties to interpret the computed anisotropies, we will use them in the modelling of the particle transport with SaP only as an indication, but not forcing the model parameters to fit the parallel first-order anisotropy for 0.5 MeV to 4.9 MeV protons.

2.3 The 17 May 2012 SEP event

2.3.1 Particle and plasma data observations from near-Earth spacecraft

Following the same format as for the previous event, the top panel of Figure 6 shows the SEP event on 2012 May 17 as seen by near-Earth spacecraft. The particle intensity-time profiles shown correspond to: the 0.3 – 4.9 MeV ion differential intensities (colored traces indicated in the legend) measured by the LEMS120 telescope and the 175 – 315 keV electron intensities (scaled to 10^{-5}, black curve) measured by the LEMS30 telescope of the ACE/EPAM instrument; the eleven energy channels of the SEPEM reference dataset, covering from energy 6 – 244 MeV proton differential intensities (colored as indicated in the legend); and the 330 – 700 MeV proton differential intensities measured by the GOES13/SEM/HEPAD detector (e.g. Sellers & Hanser 1996). The remaining panels of Figure 6 show the solar wind plasma and magnetic field measurements in the same format as for the 2012 January 23 event.

The vertical solid line in Figure 6 indicates the passage of interplanetary shocks by WIND, on May 20 at 01:20 UT (from CfA shock list). The two vertical dashed lines mark the passage of an Interplanetary Coronal Mass Ejection (ICME) as indicated in the table compiled by Richardson & Cane (www.srl.caltech.edu/ACE/ASC/DATA/level3/icmetable2.html). Note that the passage of this ICME

[6]The magnetic polarity is defined here, for RTN components as $\mathrm{sign}(\overrightarrow{B}) = \mathrm{sign}(B_R - B_T)$.

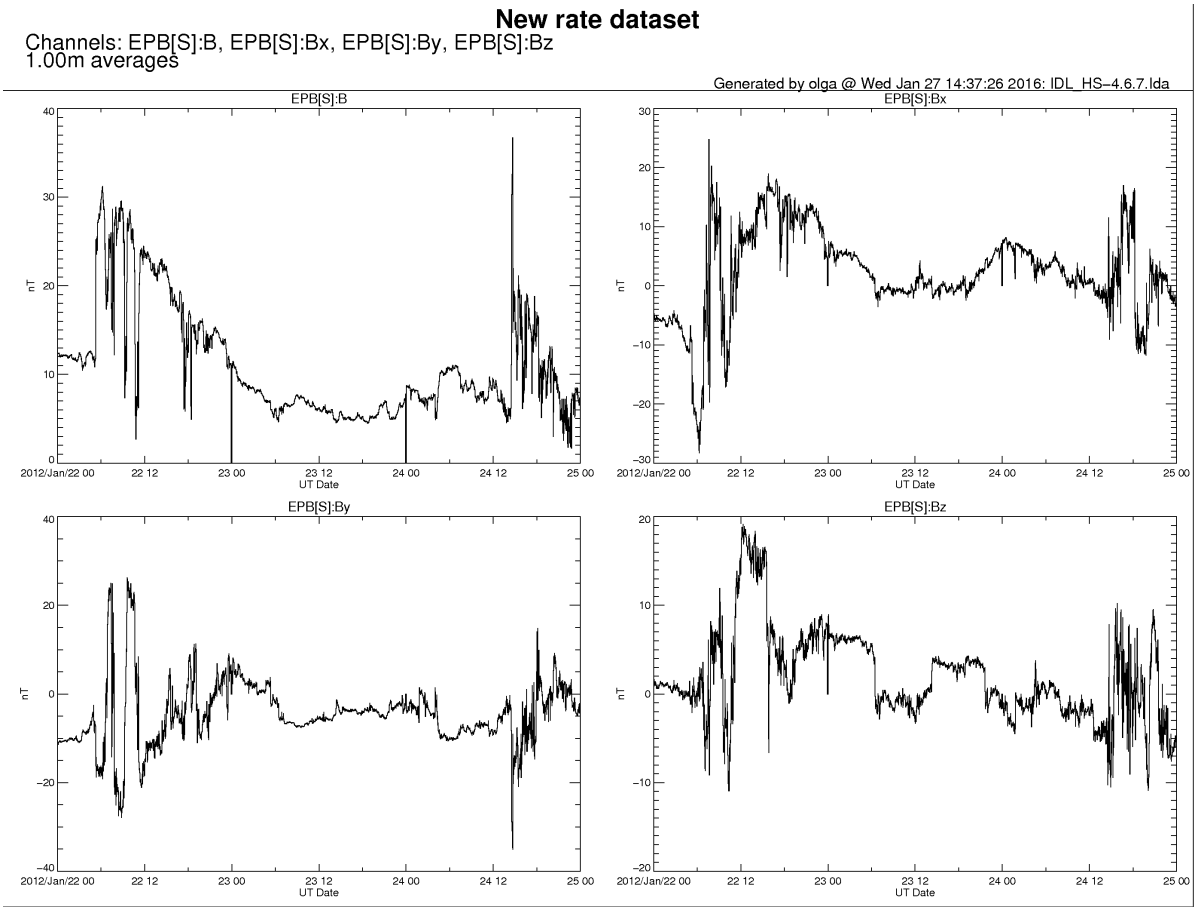

Figure 5: 2012 January 23 SEP event. Magnetic field vector in spacecraft coordinates

coincides with a clear smooth rotation in the θ-direction of the IMF. Hence, during this period the IMF does not show a Parker spiral configuration. In fact, during the first $\sim$ 12 hours on May 17, the radial component of the IMF is nearly null (see the orange curve in the 5th panel of Figure 7). Around 14 h UT on May 17, the IMF shows a rotation both in the azimuthal (bottom panel) and polar (second panel from the bottom) angles until the end of the ICME. This coincides with the dip simultaneously seen by the ACE/EPAM (top panel of Figure 6) and SOHO/ERNE/LED and EPHIN intensities. This dip is also seen in the SEPEM data, and if we consider the time of the solar wind to travel from the ACE to the GOES position, the dip in the SEPEM intensities also coincides with that observed by ACE/EPAM. This suggests that this feature in the intensity-time profiles is due to a local solar wind structure, and it is not related to the source of particles. In the solar wind and magnetic field intensity (i.e. $|B|$) panels, the horizontal orange lines mark the mean values in the upstream region. These are the 'target' values for the simulation of the solar wind with the 2D MHD model (Pomoell et al. 2015).

We have compared the SEPEM data with similar energy channels from the SOHO/ERNE LED and HED detectors as well as with SOHO/COSTEP/EPHIN detector. The proton differential intensities measured by these particle detectors onboard SOHO show a data gap on May, 17 between 7 h and 15 h UT. ERNE, EPHIN and SEPEM intensities (after subtracting the high background level of the SEPEM data) coincide during the decay phase of the intensity-time profiles (from the beginning of May 18) whereas during the rising phase of the event, SOHO and SEPEM data do not coincide. This may be explained by several factors: (i) the onset of the $<$ 55 MeV protons in the SEPEM data is clearly contaminated by higher-energy protons (due to the lack of an anti-coincidence shielding in the GOES/SEM/EPEAD

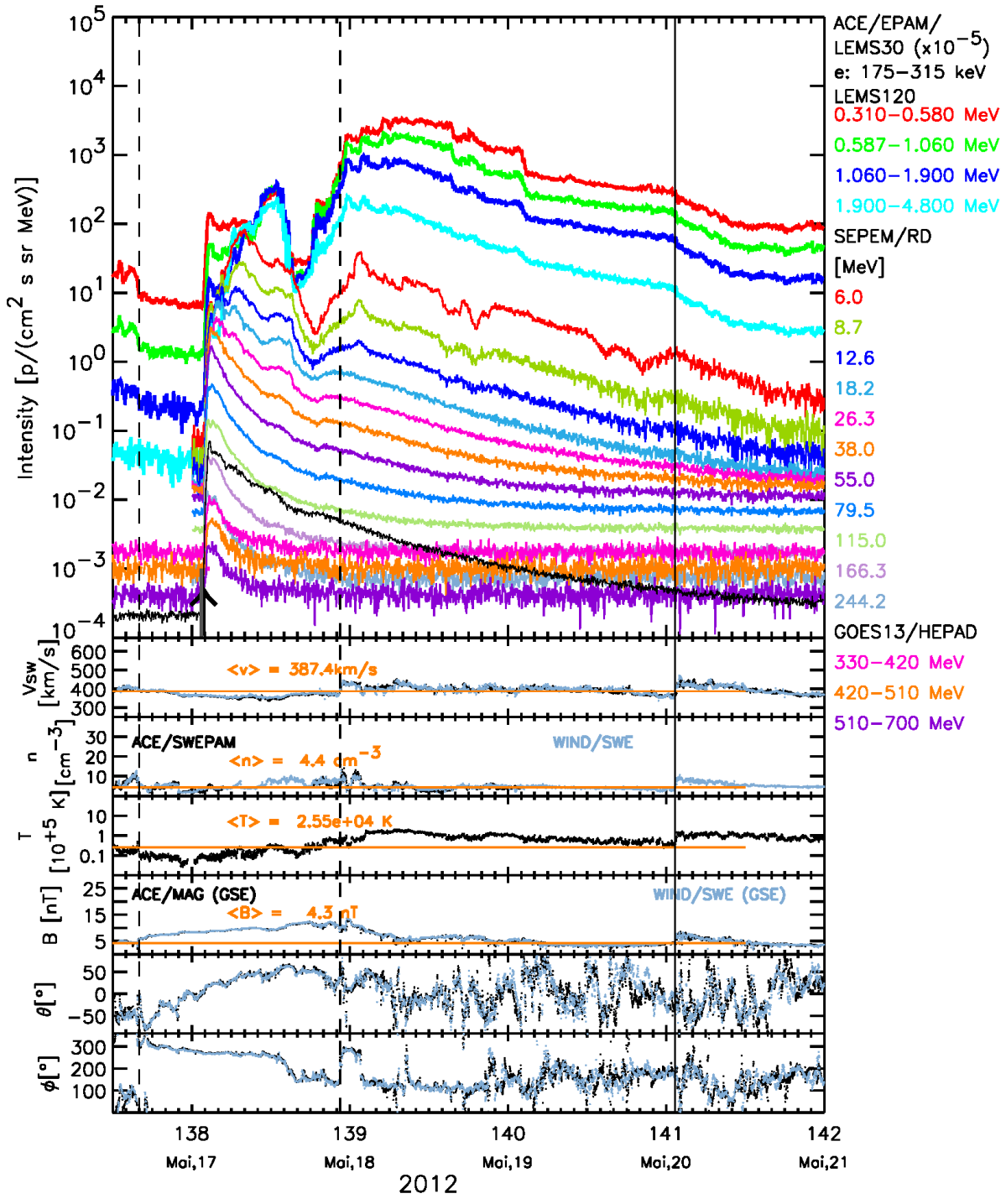

Figure 6: 2012 May 17 SEP event as seen at near-Earth environment. Particle intensities and solar wind data come from different spacecraft, as specified in the insets.

instrument); (ii) the non-Parker orientation of the magnetic field, which is perpendicular to the view direction of the instruments onboard SOHO, may prevent the measurement of the full angular distribution of particles, showing a delay in the onset with respect to the SEPEM/GOES data which observes the omnidirectional distribution; (iii) from the analysis of pulse height data from the ERNE/HED instrument, we concluded that particles showing in channels 51-131 MeV are dominated by particles penetrating the detector from the bottom (i.e., they come through the S/C) so their energies are, in fact, much higher than in the on-board analysed data; which translates into reduced intensities at the two highest energy channels of HED. Taking into account the enumerated facts, in order to simulate the May SEP event with SaP we will use the SEPEM data that does not present any data gap and reaches higher proton energies, but taking care of the too-early onset of the intensities for < 55 MeV protons.

2.3.2 Solar sources

A Halo CME with a 'plane-of-sky' speed of 1512 km s^{-1} was first seen by the SOHO/LASCO/C2 coronagraph at 01:48 UT on the 17th of May 2012 and at a height of $3.5\,R_\odot$. According to the NASA's SOHO/LASCO CME catalog (http://cdaw.gsfc.nasa.gov/CME_list/), this CME originates from near the west limb. Based on an extrapolation from the height-time plot, at 01:38 UT the CME was at a height of $\sim$1.75 $R_\odot$ (see http://cdaw.gsfc.nasa.gov/CME_list/UNIVERSAL/2012_05/htpng/20120517.014805.p261-g.htp.html).

Temporally associated with this CME eruption, an X-ray flare was observed from N05W77. The soft X-ray emission onset was at 01:25 UT on May 17 and peaked at 01:47 UT reaching an intensity level of M5.1. The onset time of the CME and the onset time of the X-ray flare are marked by an arrow and a short grey vertical line, respectively, in Figure 6. As in previous plots, the pink horizontal line close to the arrow indicates the time of γ-ray detection by Fermi/LAT (Ackermann et al. 2014), emission that in this case is much shorter in time duration than the γ-ray emission of the January event.

For the simulation of the SEP event, we will assume that the main source of particles is the shock associated with the Halo CME, with a starting time for the shock propagation at 01:18 UT on day 17. In the same way as for the previous event, we will consider that the modeling of the SEP event propagation starts at the time of the onset of the flare, 13 minutes earlier, 0.22 hours, in order to not rule out the possibility that a small portion of observed particles could come from any solar-fixed source directly.

2.3.3 Low-energy proton anisotropies from ACE/EPAM

External Contributor: D. Lario from JHU/APL

Figure 7 shows the same information as Figure 4 but for the 2012 May 17 event. In this figure we can see that the different anisotropy components abruptly change during the day on May 17, following the changes of direction of the IMF.

Note, that after $\sim$ 02 UT on May 18, the azimuthal component of the IMF roughly follows the nominal Parker spiral orientation, and that the polar angle of the IMF fluctuates around $\theta = 0^\circ$. Hence, the IMF recovers a large-scale configuration closer to the nominal one until to the shock arrival (indicated by the vertical solid line on May 20). The polarity sign is in this case positive except for the early phase of the SEP event (see the blue line in the panel displaying the radial and tangential components of the IMF in Figure 7).

As in the previous case, the orientation of the magnetic field during the initial phase of the SEP event, prevents a clear interpretation of the anisotropy data, and might be also limiting the pitch-angle range scanned by the LEMS telescopes. Hence, we will use this data in the fits of the particle intensities with SaP only after May 18.

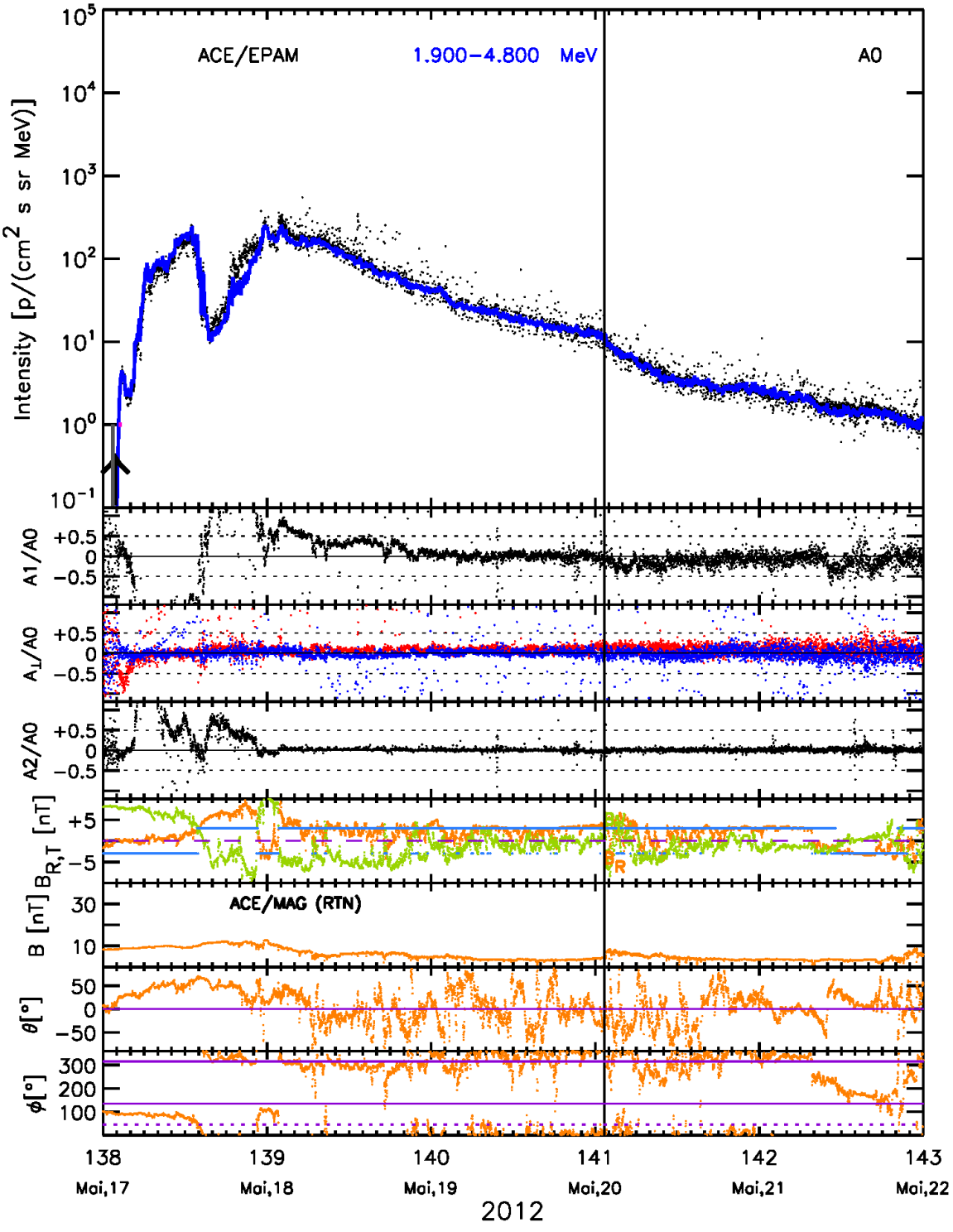

Figure 7: 2012 May 17 SEP event. 1.90 – 4.80 MeV proton intensity and anisotropies.

3 Model descriptions

3.1 The Shock and Particle (SaP) model

The Shock and Particle (SaP) model aims at simulating particle intensity-time profiles of SEP events, in particular those associated with coronal and InterPlanetary (IP) shocks acting as particle sources. For such a purpose, the SaP model follows a modular approach consisting in the following elements:

- A model to describe the IP shock propagation from the Sun to the observer's position.
- An algorithm to automatically extract the position of the point at the shock front magnetically connected with the observer, i.e. the Connecting with the OBserver POINT (cobpoint) after Heras et al. (1995).
- A particle transport model to describe the propagation of particles from the Sun or the cobpoint up to the observer's location.

The first version of the SaP model of the University of Barcelona was developed by Heras et al. (1992, 1995) and it combined a focused transport equation with the results of a 2.5-Dimensional MHD shock propagation model (Wu et al. 1983) by including a mobile source of particles at the cobpoint position. This was the first time when the concept of cobpoint was introduced. The next version of SaP, developed by Lario et al. (1998), introduced a major upgrade to the solving of the particle transport equation by including the solar wind convection and the adiabatic deceleration effects, the simultaneous fit of the particle intensities at low-energies and an improved algorithm to extract the cobpoint and shock parameters from the MHD model. This later version of SaP, in addition to quantify the injection rate of shock-accelerated particles and its spectrum, permitted the derivation of a a relation between the injection rate function of shock-accelerated protons escaping from the shock, Q, and the normalized compression ratio of the radial velocity across the shock front at the cobpoint. This is a unique result that enabled developing the first physics-based application for space weather to describe the intensity-time profiles of gradual proton events, SOlar Particle ENgineering COde (SOLPENCO) (Aran et al. 2006).

Another version of SaP (Aran et al. 2007) included an upgrade of the MHD shock propagation model in which the background solar wind can be adjusted to the observed large-scale solar wind conditions and the shock propagation, starting at 18 $R_\odot$, was extended up to 2 AU. In addition the particle transport model included the simultaneous fit of the proton intensities from low to high-energy channels, and the code was automated in a way that can be run for multiple scenarios. But the next major upgrade of the SaP model was developed under the European Space Agency (ESA) Solar Energetic Particle Environment Modelling (SEPEM) project (Aran et al. 2011). In this latter version, the MHD model was replaced by a new 2-Dimensional (2D) MHD model whose inner boundary starts at 1.03 $R_\odot$ and extends to 1.7 AU; in this way, the shock propagation could be followed from 4 $R_\odot$, to accommodate the initial CME-disturbance model (centred at 1.75 $R_\odot$). This MHD model was developed by C. Jacobs and S. Poedts from the Katholieke Universitet Leuven. In addition, a new method to extract the cobpoint and the shock information was developed (Aran et al. 2011; Rodríguez-Gasén et al. 2011). From this version of SaP, the SEPEM/SOLPENCO2 model was developed to describe the variation of gradual SEP event peak intensities and fluences with the heliospheric radial distance (Crosby et al. 2015). Further, there is a version of the SaP model that uses a 3D MHD model (Rodríguez-Gasén et al. 2011, 2014); however, the large amount of computational time required to simulate an observed SEP event renders its use difficult.

In HESPERIA, we use the latest version of the SaP model that is thoroughly described in Pomoell et al. (2015) and that was developed in the frame of the Protecting SPACE assets from high energy particles by developing European dynamic modelling and foreCASTing capabilities (SPACECAST) Project of the European Union 7th Framework Programme (FP7/2007-2013) under the Grant Agreement No.262468. The improvement of this version of SaP with respect to the version by Aran et al. (2011) is that the

new 2D MHD model uses a coronal energy source term to accelerate the solar wind instead of using a polytropic equation of state. In this way, the simulation of the shock propagation is improved since the polytropic assumption affects the shock propagation by increasing the plasma compression rather than heating it (Pomoell & Vainio 2012).

The physics and the equations used in the SaP model are fully described in Pomoell et al. (2015), Aran et al. (2007), Lario et al. (1998) and references therein. Here, we describe the steps to perform the modeling of the SEP events from the Sun to the near Earth environment:

1. Once the observational plasma and SEP data is analyzed and selected for the simulation, the first step is to derive the large-scale conditions of the solar wind in which the SEP event develops. Then the simulation of the 1.5D MHD solar wind model is run until the observed solar wind density, n, radial velocity, v_r and temperature, T are matched. With this, the free parameters of the solar wind model are fixed (the density and the temperature at $1.03\,R_\odot$; the parameters describing the source function, and the adiabatic index).

2. The 2D MHD wind is created by replicating the 1.5 D wind in the azimuthal direction. In this step, the solar rotation and the magnetic field are included. The radial component of the magnetic field at $1.03\,R_\odot$, is obtained from the 1 AU observed field and assuming a Parker Spiral configuration for the IMF.

3. A CME/shock model is then used. The parameters describing the shock model are indicated in Table 2. The initial disturbance is centered at r_{cme} and has a thickness in the radial direction of d_{cme} and of a_{cme} in the azimuthal direction. The parameter A controls the shape of the exponential profile of the density (ρ_{cme}) and speed (v_{cme}) of the initial disturbance in the radial direction whereas $\Delta\Phi$ controls its shape in the angular direction. The values of the free parameters are set by a process of trial and error until the time of the shock arrival at the observer, and the jumps in density, magnetic field, speed and temperature are reproduced as well as possible.

4. From the shock propagation simulation, the location of the cobpoint and other information related to the shock is extracted by an automated algorithm (see the Appendix A in Pomoell et al. 2015). The location of the cobpoint, r_{cob} and ϕ_{cob}, and the transit speed of the shock are the input parameters to the particle transport model. The evolution of the cobpoint is obtained from the MHD model with a temporal step of 10 minutes.

5. Once the position of the cobpoint is known[7], the fitting to the proton-intensity time profiles is performed. First, a reference energy, E_0 is selected and the corresponding intensity-time profile (and first order parallel anisotropy-time profile if available) is fitted. In this way the local source function at the cobpoint, $G(t,E_0)$ is determined as well as the proton mean free path, $\lambda_{\parallel 0}$. The mean free path scales with the particle rigidity, R, as $\lambda_\parallel = \lambda_{\parallel 0}(R/R_0)^{2-q}$ (Hasselmann & Wibberenz 1970), where we take $q = 1.6$ (e.g. Kunow et al. 1991). The integration grid extends in time, radial distance, particle pitch-angle and momentum. The grid steps taken in the present simulation are: t, μ and r are $\Delta t = 0.01$ hours; $\Delta r = 0.01$ AU and $\Delta\mu = 1/8$. In radial distance the inner (RI) and outer boundaries (RE) are separated 7 AU. RE is placed sufficiently far from RI and from the observer's position in order to ensure that it has no effect on the distribution of particles. At the beginning of the simulation, until the connection with the shock front is established, RI= 0.01 AU and RE= 7.00 AU. After this, the whole grid in the r-direction is translated to the radial position of the grid that is closest to the next cobpoint position, r_{cob}, provided by the MHD model.

[7]Due to the trial and error process to fit the observed time of the shock arrival to the observer's position and the observed shock plasma jumps, the tasks of points 1 to 4 take several weeks. Therefore, in order to prevent possible delays in the project, we initially opted to start the particle transport simulations and the shock simulations at the same time. For this, initially, the cobpoint position was derived from the MHD simulations performed during the SEPEM project, which were already available at the beginning of the project and provide a good initial estimate for the cobpoint as can be seen in the events modeled in Pomoell et al. (2015).

Table 2: Overview of the parameters in the shock model.

ρ_{cme}	v_{cme}	A	r_{cme}	d_{cme}	$\Delta\Phi$	a_{cme}
free	free	$15\ R_{\odot}^{-1}$	$1.75\ R_{\odot}$	$0.5\ R_{\odot}$	free	160°

6. Next, the simultaneous fit of the intensity-time profiles for the other energy channels is performed by varying the spectral index, γ, of the G function until the simulated profiles reproduce the observed intensities (and anisotropies). Next, the discrete values of $G(t,E)$ are fit using a polynomial function (or using splines, in the case of abrupt decreases in the temporal evolution of G) in order to obtain a continuous evolution of the particle injection rate, $G(t,E)$.

7. Finally, the polynomial fits of G for each of the modeled energy channels are provided as inputs to the University of Turku team.

3.2 Coronal Shock Acceleration (CSA) model

The Coronal Shock Acceleration (CSA) model is a Monte Carlo simulation model describing acceleration of ions in coronal shocks, taking into account ion-induced generation of Alfvén waves in the solar wind upstream of the shock. A comprehensive description of CSA is given in Battarbee (2013) and simulation results regarding various aspects of the model can be found in e.g., Vainio & Laitinen (2007; 2008), Battarbee et al. (2011; 2013), Vainio et al. (2014), Afanasiev et al. (2015). For that reason, we will provide here only a short description of the code.

CSA simulates coupled evolution of particles and Alfvén waves on a single radial magnetic field line. The intersection of the field line with the shock is taken as the lower boundary of the spatial simulation domain. The shock is treated as a MagnetoHydroDynamics (MHD) discontinuity, the gas and magnetic compression ratios of which are computed through Rankine-Hugoniot relations, using the shock's speed and obliquity and the ambient solar wind parameters at the shock position. CSA requires to specify an analytic model for either the shock-normal speed, V_s, or the shock speed along the magnetic field line, $V_{s,||} = V_s/\mu_s$, where μ_s is the shock-normal cosine (cosine of the angle between the magnetic field vector and the shock normal). The model that was used to perform CSA simulations in High Energy Solar Particle Events foRecastIng and Analysis (HESPERIA) is:

$$V_{s,||}(t) = V_{s0}(t+t_0)^{\gamma}, \tag{1}$$

where t is time, $V_{s,0}$, t_0 and γ are model parameters, which we fix by using the empirical shock modelling results (see section 4). Regarding the shock's obliquity, CSA uses the following model for the shock-normal cosine μ_s as a function of time:

$$\mu_s(t) = \frac{\mu_{s0} + \mu_{s1}\, q t}{1 + q t}, \tag{2}$$

where the parameters μ_{s0} and μ_{s1} are the initial and asymptotic (at $t \to \infty$) values of the shock-normal cosine and q specifies its rate of change.

CSA also requires analytic models for the ambient solar wind parameters such as the magnetic field, the plasma density and the plasma temperature. The magnetic field B is given as

$$B(r) = B_0 \left(\frac{r_{\oplus}}{r}\right)^2 \left[1 + b_f \left(\frac{R_{\odot}}{r}\right)^6\right], \tag{3}$$

where r is the heliocentric distance, $R_\odot$ is the solar radius, $r_\oplus = 1\,AU$, and B_0 and b_f are the input parameters. The b_f parameter allows one to account for a super-radial expansion of the associated magnetic flux tube close to the solar surface. The plasma density model that was used to perform CSA simulations in HESPERIA is

$$n(r) = n_2 \left(\frac{r_\oplus}{r + r_1} \right)^2 + n_8 \left(\frac{R_\odot}{r + r_1} \right)^8, \tag{4}$$

where n_2, n_8 and r_1 are the input parameters. The parameter r_1 was included in order to allow better fitting of the empirical shock modelling results (see section 4 for details). The plasma temperature T is given as

$$T(r) = 1.72 \times 10^6 \left(\frac{R_\odot}{r} \right)^{0.144}. \tag{5}$$

Ions and electrons are considered to have the same temperature and they both contribute to the plasma pressure.

The treatment of wave-particle interactions in CSA is based on quasi-linear theory, assuming only outward-propagating Alfvén waves, i.e., waves propagating away from the Sun, if viewed in the plasma frame, as the shock itself. Particles experience elastic pitch-angle scattering in the frame of waves, which is governed by the quasi-linear pitch-angle diffusion coefficient:

$$D_{\mu\mu} = \frac{\pi}{4} \Omega \frac{f_{\rm res} P(f_{\rm res})}{B^2} \left(1 - \mu^2\right), \tag{6}$$

where $P(f)$ is the wave power spectrum, $f_{\rm res} = \Omega V/(2\pi v)$ is the resonant wave frequency, v and μ are the particle speed and pitch-angle cosine as measured in the wave-rest frame, V is the Alfvén wave propagation speed as measured in the solar-fixed frame and Ω is the ion cyclotron frequency. If considered in other reference frames, e.g. in the plasma frame, pitch-angle scattering leads to the energy exchange between particles and waves. Pitch-angle scattering of particles off outward-propagating waves, as viewed in the plasma frame, can give rise to growth of waves. Under quasi-linear approximation, the wave growth is given as

$$\Gamma(f_{\rm res}) = \frac{\pi}{2} \Omega \frac{pS(r,p,t)}{n_{\rm p} V_{\rm A}}, \tag{7}$$

where $S(r,p,t) = 2\pi \int_{-1}^{+1} p^2 \mu v f(r,p,t)$ is the particle streaming, $n_{\rm p}$ is the proton density and $V_{\rm A}$ is the Alfvén speed.

Particles are followed in the guiding-center approximation. Alfvén waves are followed in the Wentzel-Kramers-Brillouin (WKB) approximation, with an additional diffusion term in frequency accounting for wave energy cascading.

The treatment of the particle-shock interactions consists in testing particles that hit the shock for reflection/transmission from/through the shock front. A particle transmitted into the downstream region is followed there (without advancing the simulation time) until it either returns to the upstream or reaches a distance $r_{\rm ds} = 2\lambda_2$ behind the shock (λ_2 is the particle mean free path in the downstream). In the latter case, the particle's weight[8] is modified by multiplying it with the probability of return (Jones & Ellison 1991) and the particle is re-injected into the simulation at $r_{\rm ds}$ downstream of the shock, with the pitch-angle cosine randomly picked-up from the flux-weighted isotropic downstream distribution (see, e.g. Vainio & Laitinen, 2008).

[8] In Monte Carlo simulations of SEP acceleration, because of a large number of real particles in the process, one has to deal with Monte Carlo particles that are "packages" of real particles. Each Monte Carlo particle is assigned a weight $w = N/N_{\rm MC}$, where N is the number of physical particles and $N_{\rm MC}$ is the total number of Monte Carlo particles in the simulation.

3.2.1 Shock modelling

The shock and shock's upstream plasma parameters along individual magnetic field lines, which then can be used in CSA simulations, are obtained on the basis of semi-empirical modelling. In the case of 17 May 2012 event, we use the modelling results obtained by A. Rouillard (Institut de Recherche en Astrophysique et Planétologie, Université de Toulouse, Toulouse, France) and co-workers (Rouillard et al. 2016). Their modelling technique is based on analysis of white-light and Extreme UltraViolet (EUV) images of the corona from Solar and Heliospheric Observatory (SOHO), Solar-Terrestrial Relation Observatory (STEREO) and Solar Dynamics Observatory (SDO) spacecraft, and the Potential Field Source Surface (PFSS) modelling of the coronal magnetic field using magnetograms obtained with Helioseismic and Magnetic Imaging (HMI) instrument onboard SDO. Applying the geometric fitting of the eruption images obtained from multiple vantage points, one can triangulate the 3-Dimensional (3D) expanding shock front and, correspondingly, obtain its 3D kinematics. In combination with the PFSS model, this provides the magnetic field direction and magnitude at all points on the shock surface, i.e. the 3D magnetic geometry of the shock. The white-light and EUV images are also utilised to derive the electron density in the ambient corona. The full description of the technique in application to this event is given in Rouillard et al. (2016). In the case of 23 January 2012 event, we applied a similar but technically more simplified approach (the results are given in section 4.1).

3.3 DownStream Propagation (DSP) model

The DownStream Propagation (DSP) model is a Monte Carlo simulation model that has been devised to simulate proton transport from the shock's downstream back to the Sun. This simple model is motivated by the focus on the most favourable conditions in terms of the injection into the downstream and delivery of shock-accelerated protons for the γ-ray production. The model is based on Parker's equation, which assumes quasi-isotropic particle distributions and, thus, diffusive transport,

$$\frac{\partial f}{\partial t} + \mathbf{u}\cdot\nabla f - \tfrac{1}{3}p(\nabla\cdot\mathbf{u})\frac{\partial f}{\partial p} = \nabla\cdot(\boldsymbol{\kappa}\cdot\nabla f), \tag{8}$$

where $f = \langle \mathrm{d}^6N/(\mathrm{d}^3x\,\mathrm{d}^3p)\rangle$ is the isotropic part of the particle distribution function, $\mathbf{u}$ is the velocity of the background fluid (solar wind plasma) and $\boldsymbol{\kappa}$ is the diffusion tensor. In Eq. (8), the second term on the left-hand side describes advection of particles with the solar wind, the third term describes adiabatic cooling due to the solar wind expansion and the the right-hand side term describes spatial diffusion of particles. Hence, DSP describes the propagation of particles in the test-particle approximation.

Assuming that particles are confined within a magnetic flux tube, which gives $\boldsymbol{\kappa} = \kappa\mathbf{bb}$ ($\mathbf{b}$ is a unit vector along the magnetic field) and that $\mathbf{u}\,||\,\mathbf{b}$, Parker's equation can be reduced to

$$\frac{\partial f}{\partial t} + u\frac{\partial f}{\partial z} - \tfrac{1}{3}p\frac{1}{A}\frac{\partial(Au)}{\partial z}\frac{\partial f}{\partial p} = \frac{1}{A}\frac{\partial}{\partial z}\left(A\kappa\frac{\partial f}{\partial z}\right), \tag{9}$$

where z is the (curvilinear) coordinate measured from the solar surface along the field and $A(z)$ is the cross-sectional area of the flux tube. Changing to $F = 4\pi p^2 A f$, one can obtain

$$\frac{\partial F}{\partial t} + \frac{\partial}{\partial z}\left[\left(u + \frac{1}{A}\frac{\partial(Au)}{\partial z}\right)F\right] - \frac{\partial}{\partial p}\left(\tfrac{1}{3}p\frac{1}{A}\frac{\partial(Au)}{\partial z}F\right) = \frac{1}{2}\frac{\partial^2}{\partial z^2}(2\kappa f). \tag{10}$$

Equation (10) is equivalent to the following Stochastic Differential Equation (SDE) set:

$$\begin{aligned} \mathrm{d}z &= \left(u + \frac{1}{A}\frac{\partial(Au)}{\partial z}\right)\mathrm{d}t + \sqrt{2\kappa}\,\mathrm{d}W_t \\ \mathrm{d}p &= -\tfrac{1}{3}p\frac{1}{A}\frac{\partial(Au)}{\partial z}, \end{aligned}$$

where dW_t is a stochastic differential normally distributed with zero mean and variance dt. These SDEs were solved for each Monte Carlo particle in the simulation, using the standard explicit Euler-Maruyama method.

The simulation is performed in an expanding 1-D spatial simulation box in the shock's downstream, i.e., the box is confined by the solar surface from one side and by the moving shock front from the other side, and, thus, expands with time along the magnetic field line. The shock is taken to be parallel and is treated as a reflecting wall, so no particles, which are already in the simulation box, can escape to the upstream. (This is equivalent to assuming that the diffusion coefficient at the shock is equal to zero.) For the plasma speed u and the diffusion coefficient κ in the simulation box, the following linear models are adopted:

$$U(z,t) = \frac{U_0 z}{V_S t}, \tag{11}$$

$$\kappa(z,p,t) = \frac{p\lambda_0}{3m_p}\frac{V_S t - z}{V_S t}, \tag{12}$$

where U_0 is the plasma speed immediatly behind the shock front and V_S is the shock speed, both measured in the solar-fixed frame, m_p is the proton mass and λ_0 is the particle mean free path at the solar surface. One can see from Eqs. (11) and (12) that the plasma speed decreases linearly from $u = u_0$ at the shock (where $z = z_S = V_S t$) to $u = 0$ at the Sun ($z = 0$), and the mean free path recovers from $\lambda = 0$ at the shock to $\lambda = \lambda_0$ at the Sun. To be consistent with the reflecting boundary at the shock, the amount of particles being injected into the simulation from the shock is determined by the net particle flux to the far downstream. This flux is given by

$$\begin{aligned} \mathcal{F} &= \int d^3p'\,\mu' v'\, f(p',\mu') \\ &= \int d^3p\, u_2\, f(p), \end{aligned} \tag{13}$$

where primed symbols designate quantities as measured in the shock frame, whereas unprimed ones (with the exception of u_2), like above, designate quantities as measured in the downstream plasma frame. In derivation of the second expression in Eq. (13), we made use of $d^3p/\gamma = d^3p'/\gamma'$ and the assumption about isotropic particle pitch-angle distribution in the downstream plasma frame. Thus, the flux of particles per unit momentum-space volume to the far downstream is

$$\frac{d\mathcal{F}}{d^3p} = u_2\, f(p)$$

Then,

$$\frac{d\mathcal{F}}{d^3p'} = u_2\frac{\gamma}{\gamma'}f(p) = u_2\left(1 - \frac{\mu' v' u_2}{c^2}\right) f(p',\mu').$$

Using

$$\begin{aligned} f(p',\mu') &= f(p) = f(\sqrt{p'^2 - 2\mu' p'\gamma' m u_2 + m^2\gamma'^2 u_2^2}) \\ &\approx f_0(p') - \gamma' m u_2 \frac{\partial f_0}{\partial p'}\mu', \end{aligned}$$

one can obtain to the first order in u_2/c

$$\begin{aligned} \frac{d\mathcal{F}}{dp'} &= 2\pi u_2 p'^2 \int_{-1}^{1}\left(1 - \frac{\mu' v' u_2}{c^2}\right) f(p',\mu')\, d\mu' \\ &= 4\pi u_2 p'^2 f_0(p') - \frac{4\pi}{3} u_2 p'^3 \frac{\partial f_0}{\partial p'}\frac{u_2^2}{c^2}, \\ &\approx 4\pi u_2 p'^2 f_0(p'). \end{aligned} \tag{14}$$

We use Eq. (14) to relate the amount of injected particles with the particle intensity $\mathrm{d}J/\mathrm{d}E = p'^2 f_0(p')$ at the shock provided by CSA or with the source function Q provided by SaP. If the particle intensity at shock is given as input, the number of particles per unit momentum injected at a distance z from the Sun into a magnetic flux tube of the cross-sectional area $A(z)$ in time $\mathrm{d}t$ is

$$\frac{\mathrm{d}N}{\mathrm{d}p'} = 4\pi u_2 A(z) \frac{\mathrm{d}J}{\mathrm{d}E} \mathrm{d}t, \tag{15}$$

If the source function Q (or $G = QA(z)$) from SaP is given as input, then the particle distribution function f_0 in the downstream can be obtained through the following considerations. Let us consider simple streaming along the field described by

$$\frac{\partial f}{\partial t} + \mu v \frac{\partial f}{\partial z} = 0.$$

Using the upwind finite-difference scheme, we can write

$$\frac{f_{j+1}^{n+1} - f_{j+1}^{n}}{\Delta t} + \mu v \frac{f_{j+1}^{n} - f_{j}^{n}}{\Delta z} = 0,$$

Now, let us specify that the spatial grid node j is in the downstream and $j+1$ corresponds to the shock. Then the effect of the source function Q at the shock can be modelled as convection from the downstream. Thus,

$$f_{j+1}^{n+1} = f_{j+1}^{n} \left(1 - \frac{\mu v \Delta t}{\Delta z}\right) + \frac{\mu v \Delta t}{\Delta z} f_{j}^{n},$$

where the first term represents the convection of particles further away from the shock and the second term is the source function Q_μ corresponding to some value of μ:

$$Q_\mu \Delta t = \frac{\mu v \Delta t}{\Delta z} f_j^n.$$

We average Q_μ over μ-space, assuming that f_j^n is isotropic and taking the SaP model for Q_μ:

$$Q_\mu = Q(1+\mu)$$

Thus, we derive:

$$\int_{-1}^{+1} Q_\mu d\mu = 2Q = \int_{0}^{+1} \frac{\mu v}{\Delta z} f d\mu = \frac{1}{2} \frac{v f}{\Delta z},$$

where the indices are omitted, and correspondingly

$$f = 4 \frac{\Delta z}{v} Q. \tag{16}$$

Note that Eq. (16) somewhat overestimates f because in SaP the particle injection is assigned not only to the positive nodes of the μ-grid but also to the negative nodes and, hence, some fraction of Q is immediately removed from the simulation. In order to account for this feature, we introduced a correction factor a_f, such that

$$f = 4 a_\mathrm{f} \frac{\Delta z}{v} Q, \tag{17}$$

and computed its value to be 0.881. This value is obtained by performing a linear regression of particle intensities (at the shock when it crosses the observer at 1 AU) obtained directly from a SaP simulation on particle intensities calculated, using Eq. (16), from the provided values of Q.

The proton injection into the downstream is modelled in the following way. We introduce an injection time step $\delta t_{\rm inj}$ and deposit a certain number of Monte Carlo particles into the simulation box at each $\delta t_{\rm inj}$. A Monte Carlo particle is characterised by its weight w, as it is not a real particle but a representative of a group of real particles. To obtain weights of injected Monte Carlo particles at a given time t_0, we compute values of the spectrum $\mathrm{d}N/\mathrm{dp}'$ at the momentum grid points, using Eq. (15), and interpolate those spectral values by power laws between the grid points. Then the weight of a Monte Carlo particle with momentum p' between the grid points p'_j and p'_{j+1} is given by

$$w = \frac{1}{N_{\rm MC}} \int\limits_{p'_j}^{p'_{j+1}} \frac{\mathrm{d}N}{\mathrm{d}p'}\,\mathrm{d}p', \tag{18}$$

where $\mathrm{d}N/\mathrm{d}p' \propto p'^{-q_j}$ and $N_{\rm MC}$ is the number of Monte Carlo particles assigned to the interval $[p'_j, p'_{j+1}]$. Note that the particle momentum p' is randomly chosen from p'^{-q_j} distribution in this interval.

The Monte Carlo particles injected at a given time t_0 are placed into a small spatial area $\delta z = u_2 \delta t_{\rm inj}$ behind the front, to mimic their advection by the bulk plasma during $\delta t_{\rm inj}$. Then, each of these particles is propagated by solving the SDEs until it hits the Sun, i.e., precipitates, or up to $t = t_{\rm max}$. Note that the extension of the simulation box (due to the shock propagation) while propagating particles is taken into account. At the next moment $t_0 + \delta t_{\rm inj}$, the shock front is shifted ahead by $V_{\rm S}\delta t_{\rm inj}$ from its position at time t_0.

The cross-sectional area $A(z)$ of the flux tube at distance z from the Sun, entering Eqs. (15) and (**??**) is determined by scaling down the cross-sectional area A_0 at 1 AU, which is taken as an input parameter. In the shock's downstream, the flux tube cross-sectional area is determined by

$$A(z) \propto \frac{(1+\tilde{z})^2}{1 + b_{\rm f}(1+\tilde{z})^{-6}}, \tag{19}$$

where $\tilde{z} = z/r_\odot$ is given in units of the solar radius $r_\odot$. The input parameter $b_{\rm f}$ controls the expansion of the flux tube: $b_{\rm f} = 0$ describes the radial expansion of the flux tube and $b_{\rm f} > 0$ corresponds to the super-radial expansion.

At the start of the simulation, the shock is placed at the heliocentric distance $r_{\rm S0}$, which corresponds to $z_{\rm S0} = r_{\rm S0} - r_\odot$. This determines the initial "shock" time $t_{\rm S0} = z_{\rm S0}/V_{\rm S}$. The simulation goes on until the "shock" time reaches $t_{\rm S,max} = t_{\rm S0} + t_{\rm max}$, where $t_{\rm max}$ is the γ-ray event duration. During the simulation, we collect Monte Carlo particles absorbed at the solar surface and, based on their momenta, precipitation times and weights, compute the integrated momentum (energy) spectrum and flux of absorbed protons.

4 Results of modelling

4.1 The 23 January 2012 event

4.1.1 Modelling of the SEP event from the solar corona to the near-Earth space

In order to derive the injection rate of shock accelerated protons that escape from the interplanetary shock and reach the near-Earth environment, we have used the SaP model described in Section 3.1. For the two selected events, we have first reproduced the average solar wind conditions observed at 1 AU from the onset of the SEP event up to the associated interplanetary shock crossing by the Earth. For this, we use the solar wind model by Pomoell et al. (2015) as described in Section 2.1.

Table 3: Solar wind initial parameters for the 2012 January 23 event.

Event	ρ_0 [kg/m^3]	T_0 [K]	S_0 [W/m^3]	L [R$_\odot$]	γ	B_{r0} [T]
Jan12	$1.169 \cdot 10^{-13}$	$1.22 \cdot 10^{6}$	$0.335 \cdot 10^{-7}$	0.735	1.55	$-2.15 \cdot 10^{-4}$

Simulation of the solar wind and of the IP shock propagation

Figure 8 shows the heliocentric radial distance profile for the solar wind density and temperature (top panels), the radial and azimuthal components of the solar wind velocity (middle panels) and for the radial and azimuthal components of the simulated interplanetary magnetic field (bottom panels).

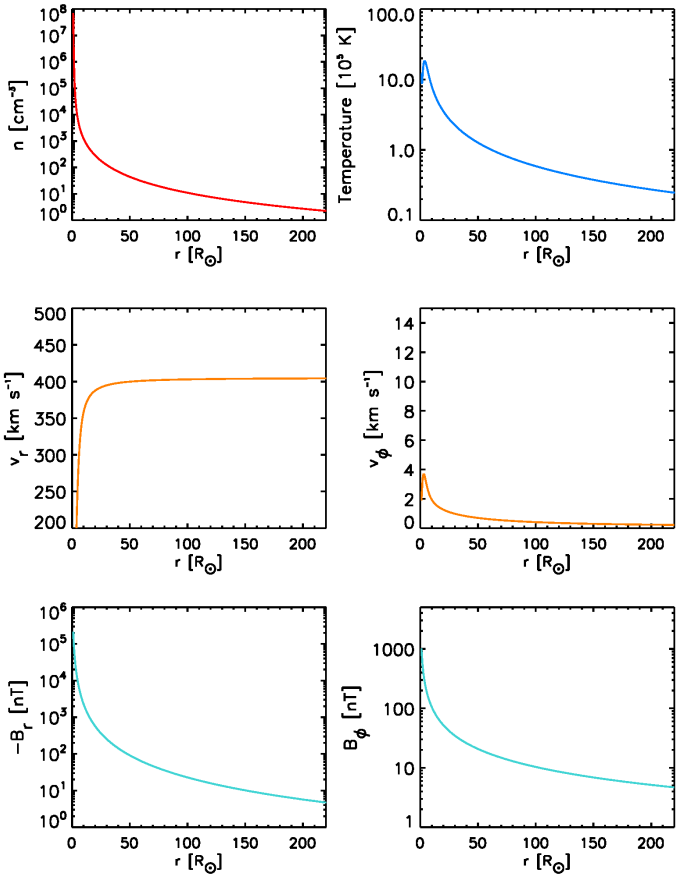

Figure 8: Solar wind plasma variables as a function of the heliocentric radial distance for the 2012 January 23 event

.

The initial parameters at the low corona (at $1.03\,R_\odot$) to generate this solar wind are listed in Table 3.

Once the background solar wind is stabilized, the CME-shock propagation is simulated by superimposing a perturbation on the wind. The initial 'CME' free parameters that better reproduce the time of the shock arrival to 1 AU and the observed plasma jumps are: $\rho_{cme} = 0.3 \times 10^{-13}$ kg m^{-3}, $v_{cme} = 1650$ km s^{-1}, and $\Delta\phi = 0.25 a_{cme}$. Figure 9 shows that the simulated solar wind (blue curves) reproduces well the large scale solar wind conditions (red and orange curves) during the upstream region of the SEP event, especially prior to the shock passage. The time of the shock arrival is also reproduced

as well as the observed jump in the magnetic field strength (bottom left panel). The simulated jumps in number density and solar wind speed are, in this case, slightly higher than observed; whereas the jump in temperature (bottom right) is presumably highly overestimated by the model. Note that due to the data gap in the ACE data, the value of the average temperature in the upstream region has been taken from the plot provided by the IP shocks data base of the University of Helsinki (http://ipshocks.fi/database), based on WIND data. The value of the temperature is $T = 2.5 \times 10^4$ K. A similar value is estimated by the CfA interplanetary shock list. The plasma observations downstream of the shock are not reproduced by the 2D MHD model, except for the magnetic field (bottom left panel of Figure 9).

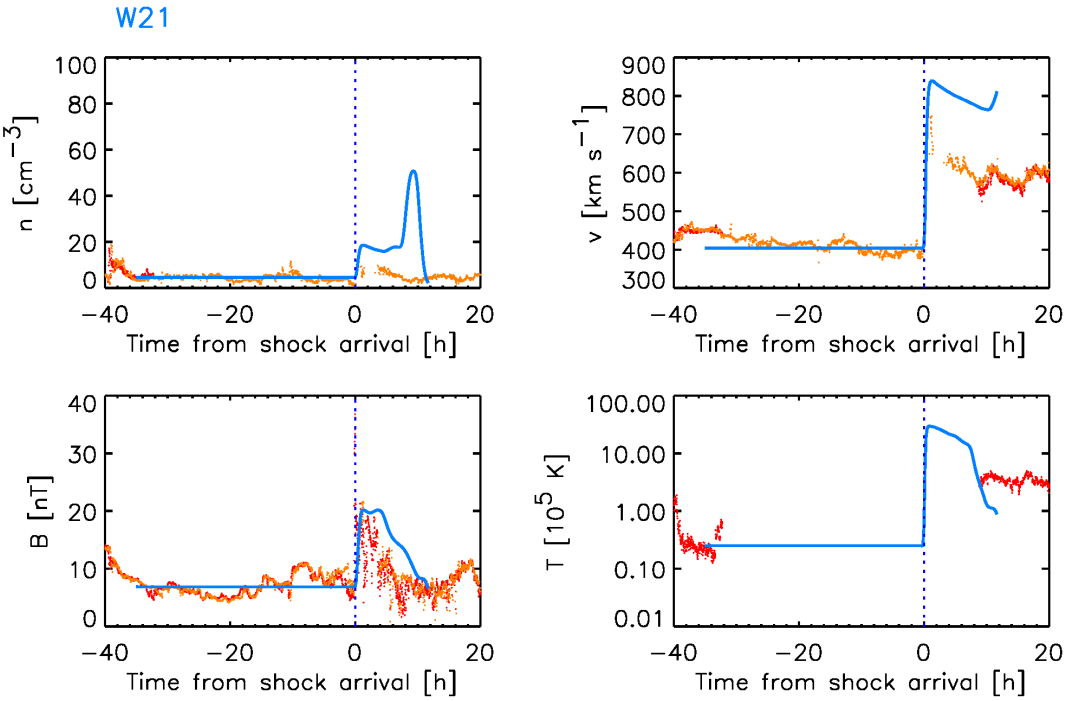

Figure 9: 2012 January 23 event. From left to right, top to bottom: the solar wind density and radial velocity, and the magnetic field strength and the solar wind temperature measured by the ACE spacecraft (red curves) and the WIND spacecraft (orange curves). The corresponding values from the simulation are plotted in blue. Time is counted from the time of the interplanetary shock passage by the ACE spacecraft and it is marked by a dotted vertical line.

The next step is to determine the position of the cobpoint and the transit speed of the shock every ten minutes from the MHD simulation. These are the input parameters required for the particle transport simulation. The extraction of the cobpoint and of the shock characteristics is performed in an automated way as described in Pomoell et al. (2015). In addition to the cobpoint evolution, from the MHD simulation of the shock propagation we obtain: the shock normal, the shock speed, the transit speed of the shock and the upstream and downstream values (along the shock normal) of the plasma density and velocity and of the magnetic field, as well as the θ_{Bn} angle. The left panel of Figure 10 shows the radial velocity contour plot of the MHD simulation at $t = 28.67$ hours. The 1 au observer (grey circle) is placed 21° east from the direction of propagation of the shock (towards the negative X-axis, at $Y = 0$). The simulated IMF line connecting the observer with the shock front (upstream) and the cobpoint with the Sun (downstream) is displayed in grey. The cobpoint is marked by the black circle at the intersected point of the shock front. The shock normal and radial directions along the position of the cobpoint are indicated by black-solid and magenta-dashed lines, respectively. The right panel of Figure 10 shows the values of different parameters (black solid lines) evaluated along the shock-normal direction through the

cobpoint (the zero point in the X-axis, which is the distance from the cobpoint expressed in $R_\odot$) used to determine the final position of the upstream and downstream locations where the plasma jumps are computed. The upstream point is marked by the squares and the downstream point by circles. The final downstream point is the one closest to the upstream point.

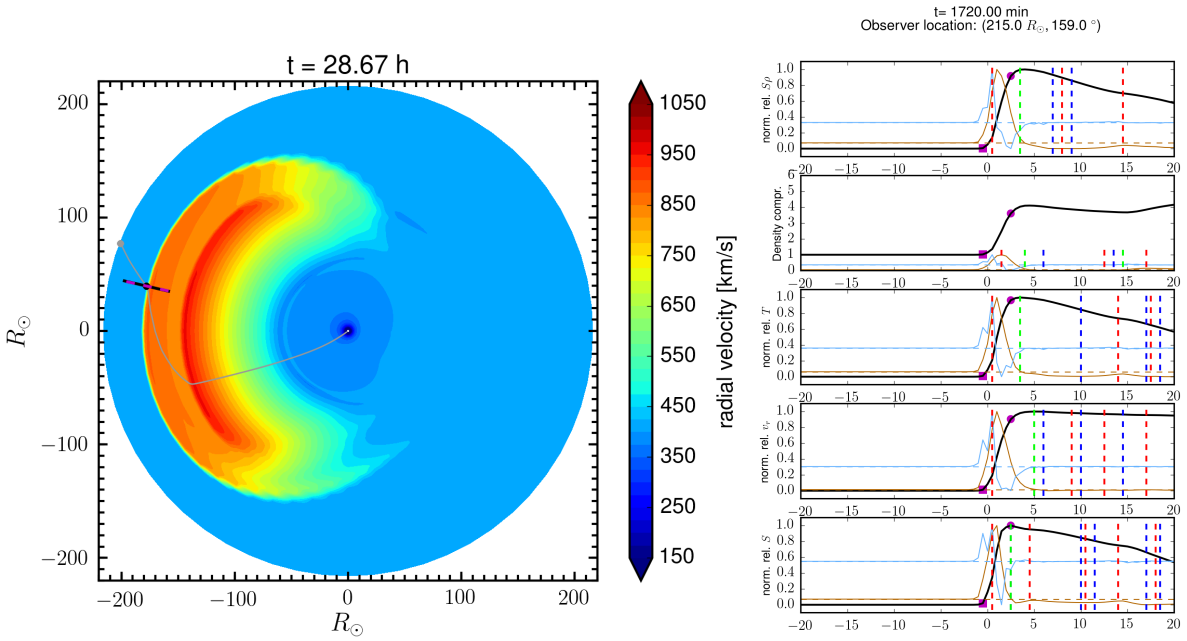

Figure 10: 2012 January 23 event. Left: Contour plot of the plasma radial velocity (color bar) at $t = 28.67$ h. The IMF line crossing the observer's (grey circle) position is indicated in grey. The cobpoint (black circle) and the normal (pink dashed line) and the radial (black line) directions through the cobpoint are also shown. Right (from top to bottom): Values of the normalized relative entropy density, compression ratio, normalized relative temperature, normalized radial velocity and normalized relative entropy along the shock normal for the cobpoint corresponding to the same snapshot. Squares mark the upstream position and circles the downstream location. The X-axis indicates the distance from the cobpoint position in $R_\odot$.

Simulation of the particle transport to Earth's orbit

In order to derive the rate of the protons injected (per unit area) by the shock into the magnetic flux tube that connects the observer with the simulated shock front, the G injection rate, we have fitted the observed intensity and anisotropy -time profiles for 0.3 – 4.9 MeV protons by using the ACE/EPAM data analyzed in Section 2.2 and the intensity-time profiles of the 10 proton energies provided by the SEPEM reference data (shown in Figure 2).

Since proton enhancements observed in this SEP event in the GOES/HEPAD energy channels 330 – 420 MeV, 420 – 510 MeV and especially in the 520 – 700 MeV channel are not clear, we have produced synthetic intensity-time profiles for these channels by extrapolating the particle injection rate $G(t,E)$ from the highest energies in the SEPEM reference dataset rather than by trying to fit the observed intensities at these energies.

In order to perform this fitting, we have followed the method explained elsewhere (e.g. Aran et al. 2007; Pomoell et al. 2015). Figures 11, 12 and 13 show the resulting modeled intensity and parallel first-order anisotropy -time profiles (blue sky curves) for the 14 simulated and the 3 extrapolated energy channels. Red curves are the corresponding observations. The two vertical solid blue lines indicate

the times of the shock arrival to ACE and to GOES. The orange dotted vertical line indicates the onset of the associated X-ray flare and the remaining dotted purple lines indicate changes in the direction of the IMF as in previous figures of Section 2.2. For this event, we have subtracted the pre-event background intensities in order to compare observations with the modeled intensity profiles (except for the GOES/HEPAD data, to show that there was not an SEP enhancement detected). For each energy, the subtracted intensity levels are indicated by small green horizontal lines.

The shock-connection time is $t_c = 0.45$ hours and the radial position of this first cobpoint is $r_c = 4.7 R_\odot$. The energy of reference taken to perform the fitting of the intensity-time profiles is $E_0 = 8.7$ MeV. To model this event, we have assumed a constant radial proton mean free path, and hence, $\lambda_\parallel$ increases with the heliocentric radial distance ($\lambda_\parallel = \lambda_r \sec^2 \psi(r)$, where ψ is the angle between the IMF and the radial direction). Assuming a Parker Spiral form for the IMF we have taken:

$$\lambda_{\parallel 0} = \lambda_{r0} \left(\frac{r^2 + \Gamma^2}{(1\ \mathrm{AU})^2 + \Gamma^2} \right)$$

where $\Gamma = v_{sw}/\Omega_\odot = 223.4 R_\odot$, with $v_{sw} = 414$ km s^{-1}, and $\Omega_\odot = 2.6662 \times 10^{-6}$ s^{-1}, and $\lambda_{r0} = 0.25$ AU. In this way $\lambda_{\parallel 0} = 0.25$ AU at 1 AU and decreases with decreasing distance to the Sun.

As we mentioned in Section 2.2, an Energetic Storm Particle (ESP) component can be clearly seen in ACE/EPAM data. For higher energies, proton intensities show a local peak at the time of the shock passage (< 18 MeV). This is preceded by a smooth increase of the intensity after a change of flux tube at $\sim$13:30 UT on day 24 (see the blue trace of the ϕ panel of Figure 2). We consider this increase as a small ESP ramp. Taking this into account, we have assumed a region ahead of the shock with enhanced turbulence for $E \leq 12.6$ MeV. Such foreshock region is modeled from the first connection with the shock and has a width of 0.07 AU. It is divided in two parts. An inner region, 0.03 AU wide, with stronger scattering, $\lambda_{rc0} = 0.01$ AU and and outer region with $\lambda_{rc0} = 0.03$ AU. The energy scaling within the foreshock is given by $\lambda_{\parallel c} = \lambda_{\parallel c0}(R/R_0)^\alpha$, $\alpha = +2$ (Heras et al. 1992).

After we have obtained the evolution of $G(t, E_0)$ by fitting the intensity-time profile at E_0, we simultaneously fit the intensity-time (and first-order anisotropies) for the other energy channels by assuming that G scales with energy as $G(E) = G(E_0)(E/E_0)^{-\gamma}$. For this particular event we had to use different values of γ with time and for different energy ranges, which means that the injection energy spectrum does not follow a power-law shape. In the case of the extrapolated energies, we have assumed the same energy spectra as for the 166 MeV protons. The initial discrete values of $G(E,t)$ obtained from the fitting are shown by colored circles in Figure 14. Next, in order to get a continuous evolution of G with time, we fit a polynomial for each energy to the values of G. The fittings shown above are obtained with these polynomial fits (black curves in Figure 14).

Note that in terms of the injection rate in the phase-space, Q, the shock associated with this SEP event is more efficient at injecting protons onto the IMF that the shocks of the 2000 April 4 and 2006 December 13 SEP events presented in Pomoell et al. (2015).

Output provided for the DSP model

In order to investigate whether up to which extent the shock portion connected to the observer at 1 AU may explain the observed γ-ray emission, we use the injection rate G as input for the DSP model. For this, the coefficients of the fits (black curves) to the values of G shown in Figure 14 and the range of their applicability are provided to the team of UTU together with the first connection point.

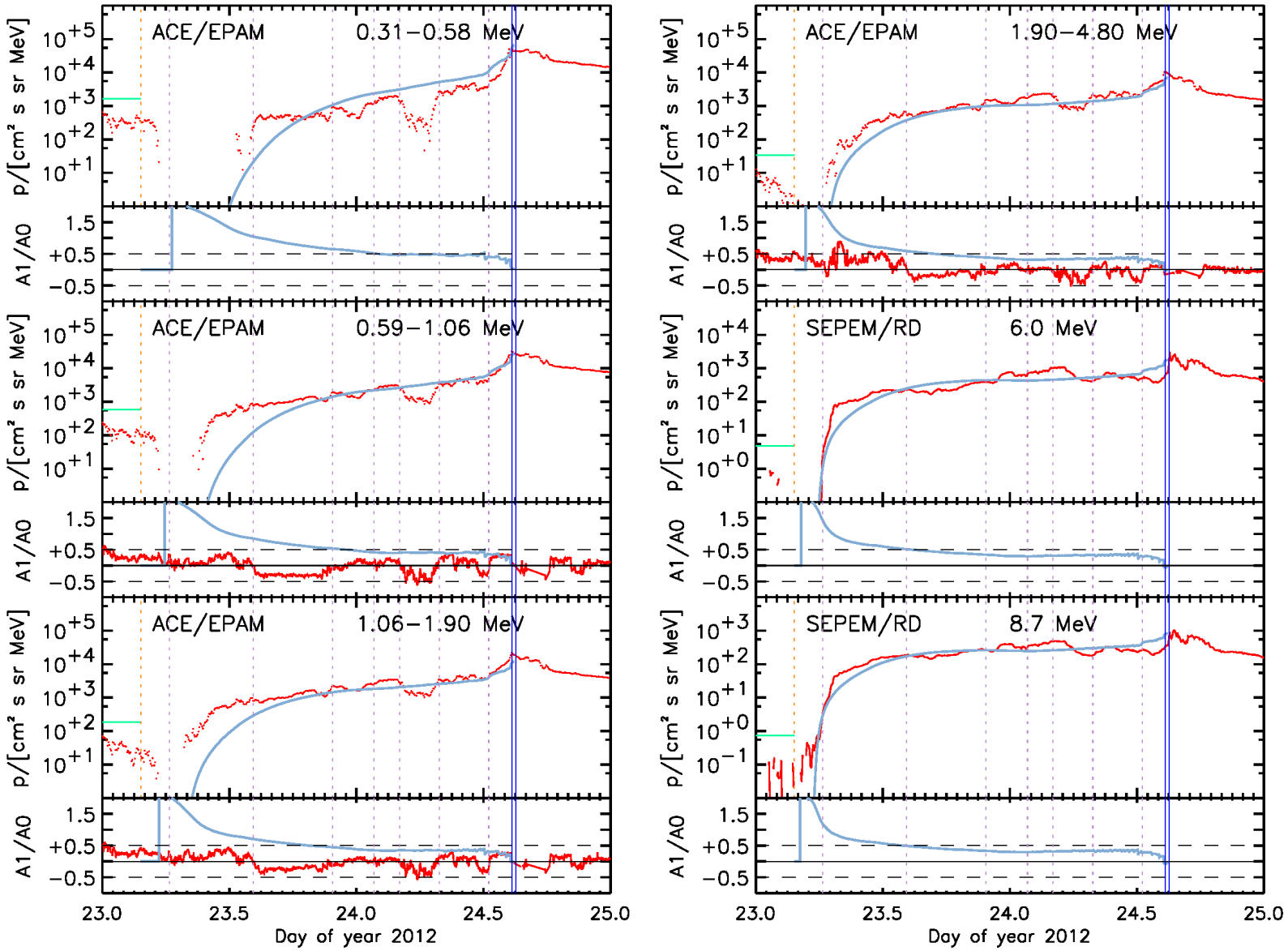

Figure 11: Fitted (blue sky curves) intensity-time profiles and parallel first-order anisotropies (A1/A0) for 0.3 − 8.7 MeV protons. Comparison with ACE/EPAM and SEPEM reference data (red curves).

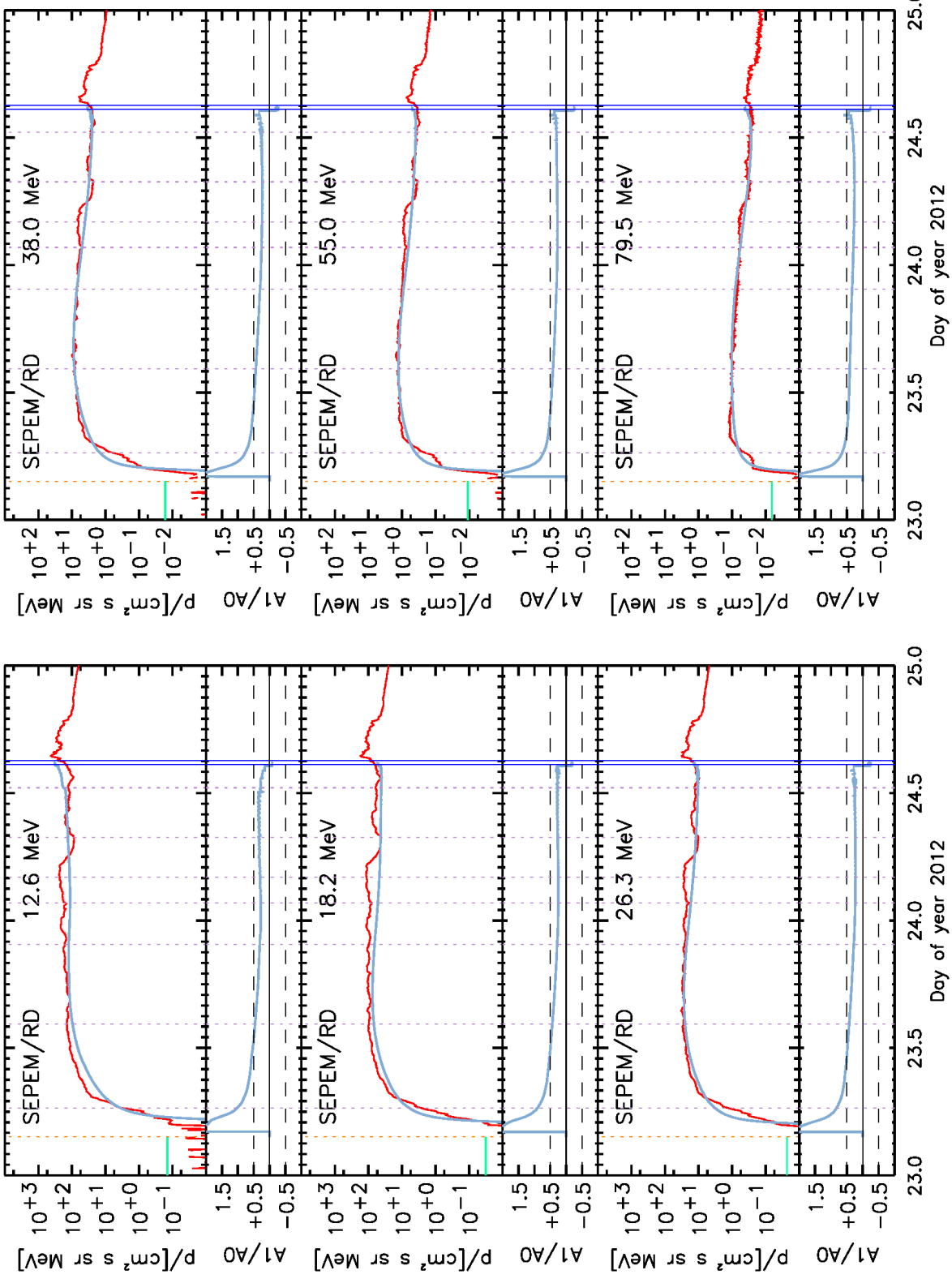

Figure 12: Fitted (blue sky curves) intensity-time profiles and parallel first-order anisotropies (A1/A0) for 12.6 – 79.6 MeV protons. Comparison SEPEM reference data (red curves).

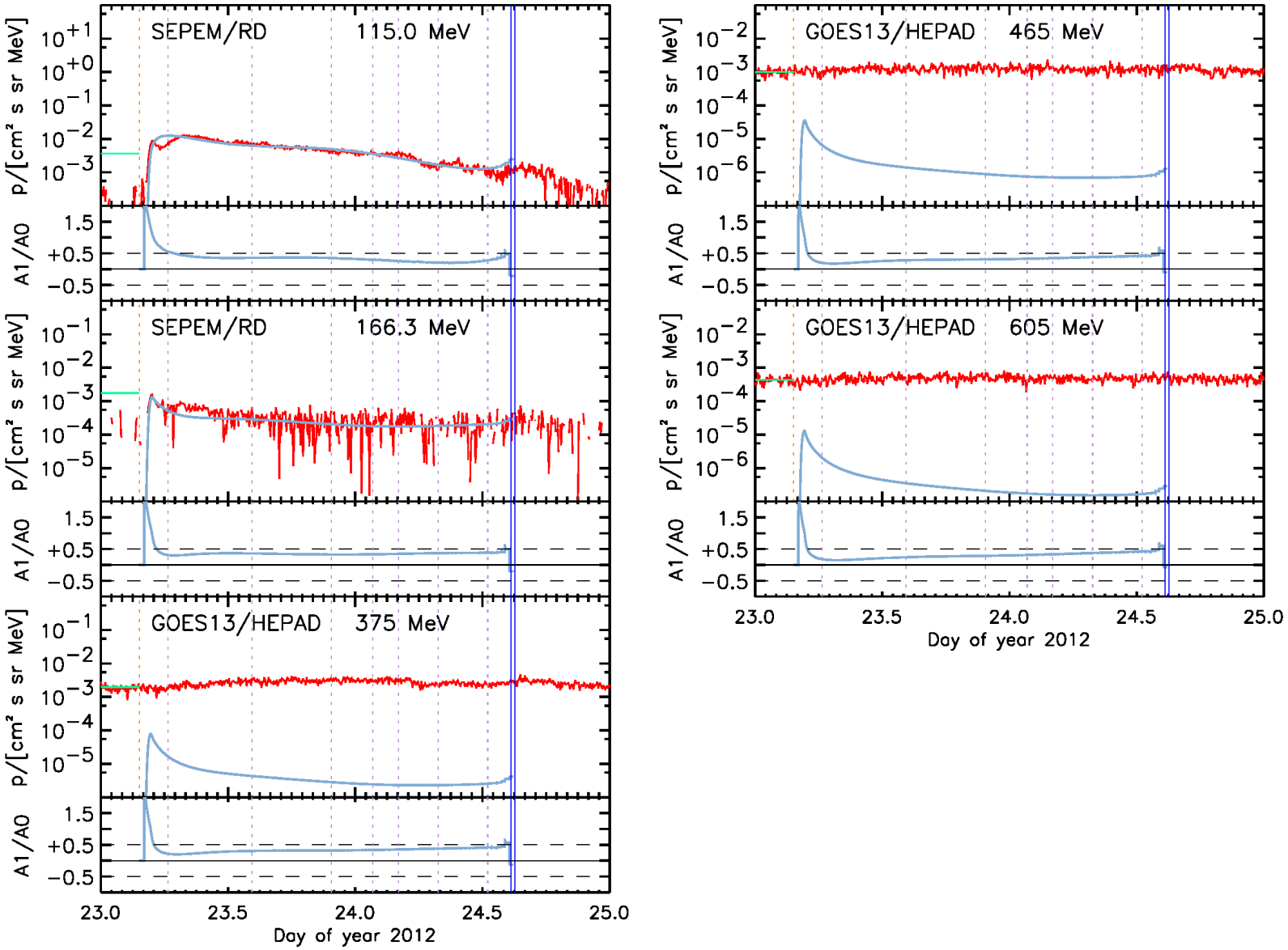

Figure 13: Fitted (blue sky curves) intensity-time profiles and parallel first-order anisotropies (A1/A0) for 115 MeV and 166 MeV protons. Comparison with SEPEM reference data (red curves). For E $>$ 166 MeV, we show the model extrapolated intensities (blue sky curves) for the GOES/HEPAD data (red curves).

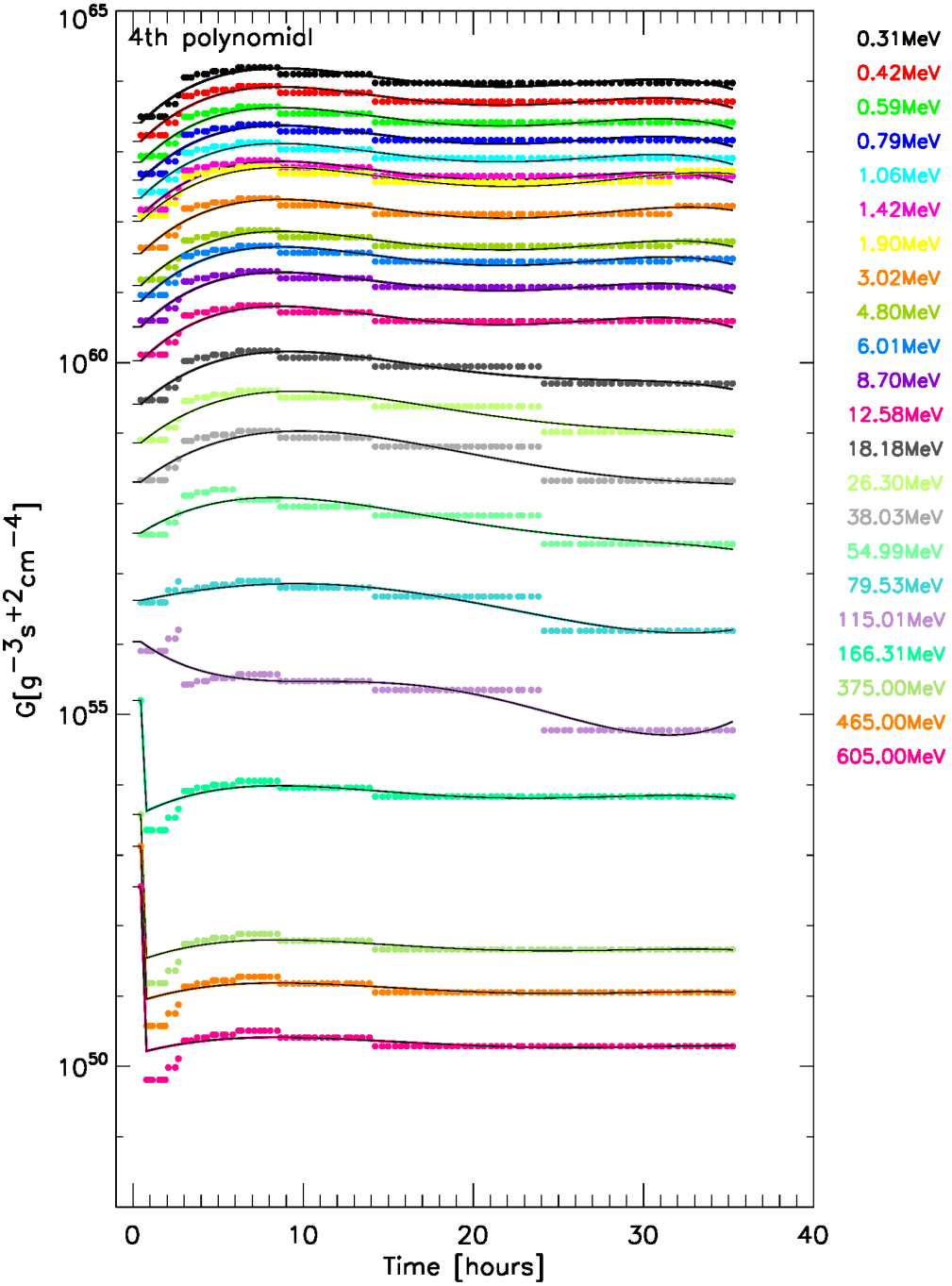

Figure 14: Evolution of the proton injection rate, G, for each simulated energy (color coded). Black lines correspond to the polynomial and linear fits delivered as input to the DSP model.

4.1.2 Modelling of proton acceleration in the shock

Shock modelling

We shall first describe the modelling performed to infer the shock and shock's upstream plasma parameters, which then were utilised in the CSA simulations of particle acceleration in this event.

On the time of the 23 January 2012 event, the STEREO A and B spacecraft together with the SOHO spacecraft provided a 3D view of the Sun, being located at 108° ahead of the Earth and 113° behind the Earth, respectively. We have utilised images provided by the white-light coronagraphs to infer kinematics of the CME associated with the SEP event. For a set of images corresponding to a particular time, the CME front was fitted in each image by a circle (Fig. 15). For each fitted circle, its radius and coordinates of the origin (in the heliocentric Cartesian coordinate system of the image) were determined. After that, the circle parameters obtained from fitting the STEREO A and B data were projected onto the Heliocentric Earth Equatorial coordinate system (HEEQ) and the obtained time sequences of the HEEQ coordinates X, Y and Z of the circle origins and of the projected circle radii R were fitted by linear functions (Fig. 16). The fits obtained give the 3D kinematics of the eruption sphere. We emphasize here that this method is somewhat subjective and not as accurate as the one employed by A. Rouillard for the GLE 71, but since we had no information on the density structure of the ambient medium available by the time of the start of the modeling, we decided that the errors we make on the CME shock dynamics by the use of this method are probably small compared to other uncertainties in the data.

The next step was to perform the PFSS modelling of the coronal magnetic field. This was done using the routines available in solarsoft[9]. Example modelling results are presented in Fig. 17.

The combination of the PFSS model with the geometrical model of the eruption provided us with values of the magnetic field B and of the shock parameters (the shock speed along the field line $V_{s,||}$ and the shock-normal cosine $\mu_s = \cos\theta_{Bn}$) along different magnetic field lines at the shock at different heights from the solar surface. Those values were correspondingly fitted by the following functions:

$$V_{s,||}(t) = V_{s0}(t+t_0)^{\gamma}, \tag{20}$$

$$\mu_s(t) = \frac{\mu_{s0} + \mu_{s1}\, qt}{1+qt}, \tag{21}$$

and

$$B(r) = B_0 \left(\frac{r_\oplus}{r}\right)^2 \left[1 + b_f \left(\frac{R_\odot}{r}\right)^6\right], \tag{22}$$

where $r_\oplus = 1\,AU$, and V_{s0}, t_0, γ, μ_{s0} , μ_{s1}, q, B_0 and b_f are the fitting parameters.

To perform particle acceleration simulations, we have chosen one field line (shown in Fig. 17, bottom row), which gives quite a fast increase in the Alfvénic Mach number with distance from the Sun (Fig 18), assuming that the plasma density is given by

$$n(r) = n_2 \left(\frac{r_\oplus}{r}\right)^2 + n_8 \left(\frac{R_\odot}{r}\right)^8, \tag{23}$$

with $n_2 = 10\,\mathrm{cm}^{-3}$ and $n_8 = 8\times 10^8\,\mathrm{cm}^{-3}$. The shock parameters as well as the magnetic field magnitude corresponding to this field line are presented in Fig. 19.

[9] http://www.lmsal.com/derosa/pfsspack/

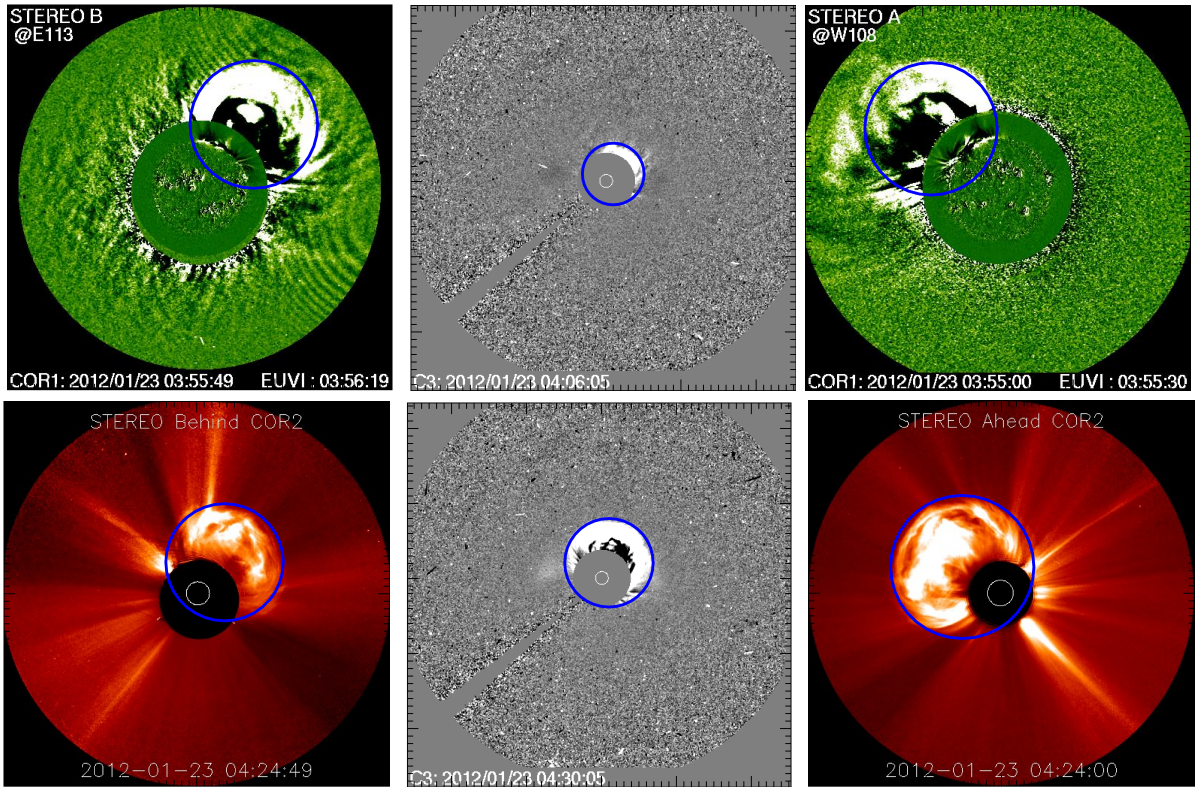

Figure 15: Images of the CME as observed by STEREO A and B and SOHO at the closest times to 04:00 UT (upper row) and 04:27 UT (bottom row) 23 January 2012, with fitted circles (in blue) superimposed.

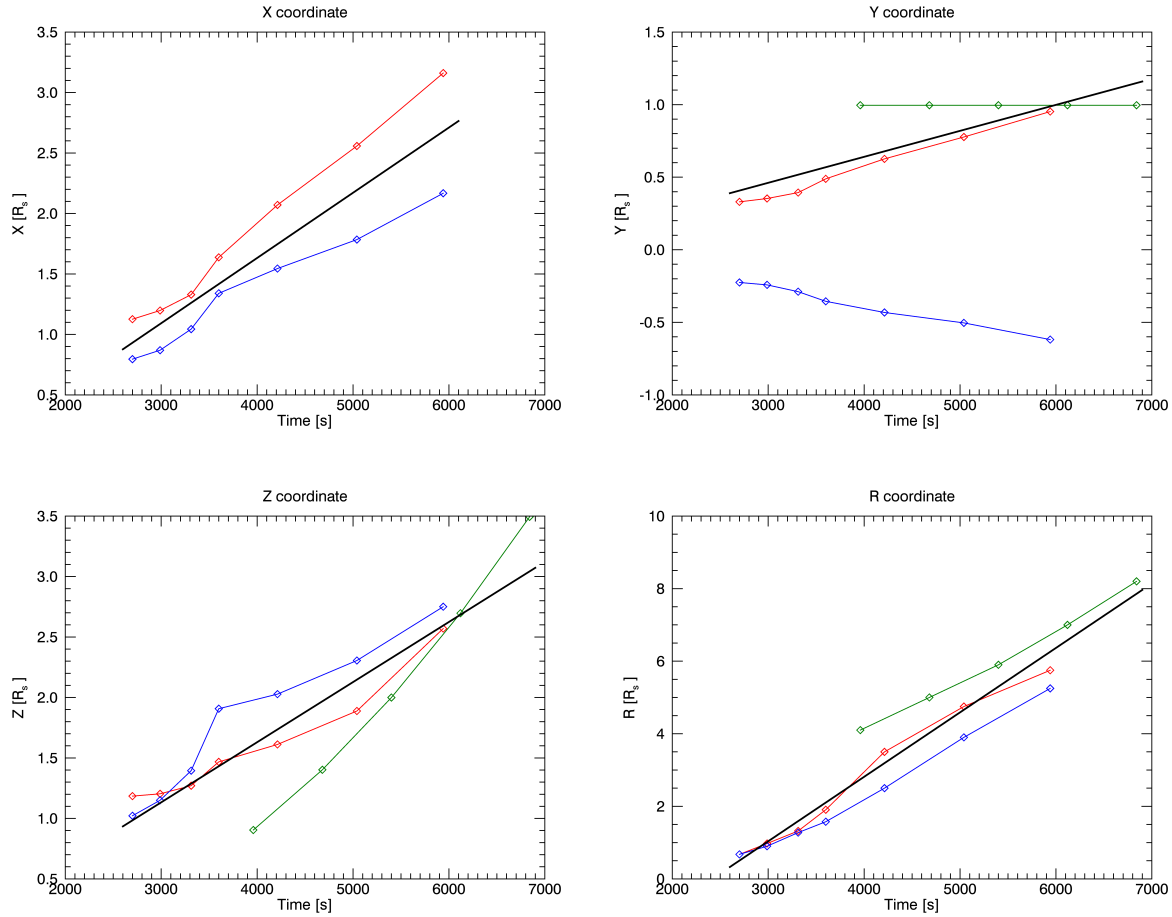

Figure 16: HEEQ coordinates of the origins and radii of fitting circles used to fit the CME front as observed by STEREO and SOHO versus time with the linear fit superimposed. The STEREO A data are depicted by red, STEREO B data by blue and SOHO data by green. The fit is shown with black line. Note that when fitting the Y-coordinate, the STEREO B data were not taken into account.

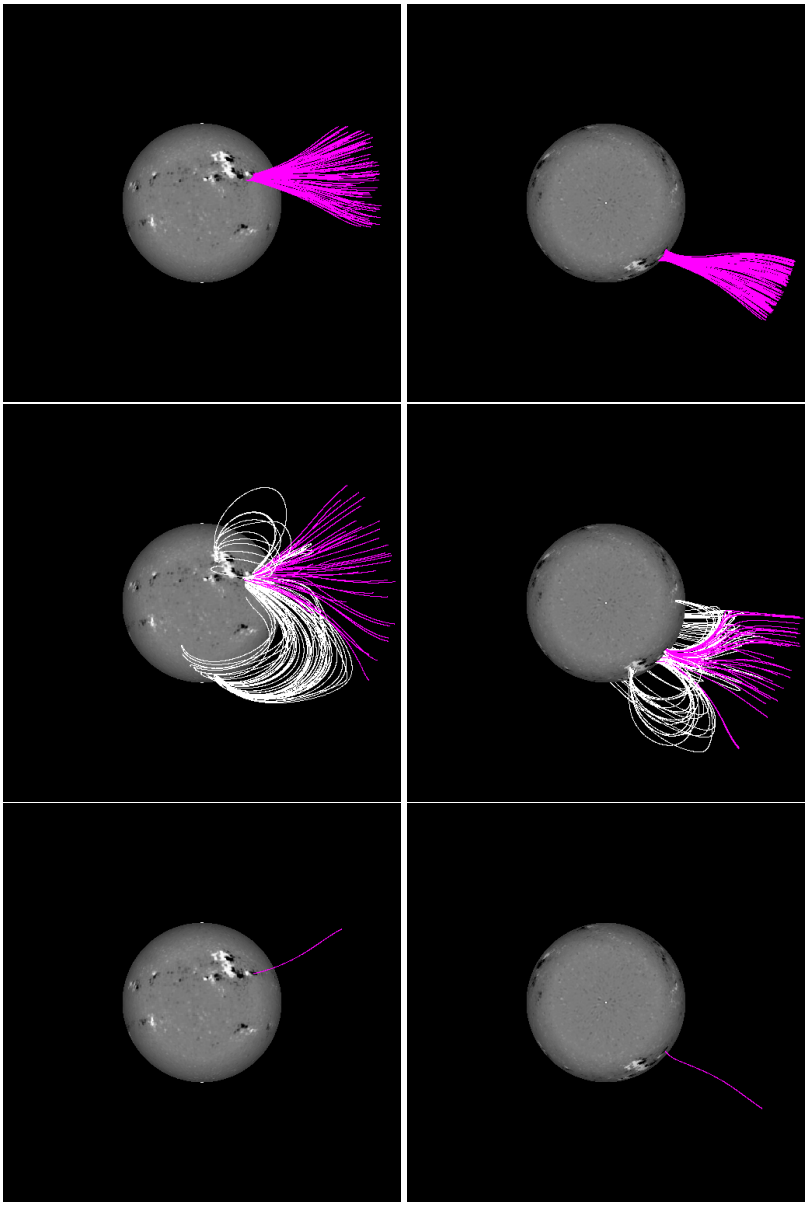

Figure 17: Coronal magnetic field lines computed with the PFSS model as viewed from the Earth (left column) and from above the solar north pole (right column). The upper row of images shows a bunch of open field lines rooted in the active region, the middle row of images shows open field lines together with closed field lines and the bottom row shows the field line used to carry out a CSA simulation.

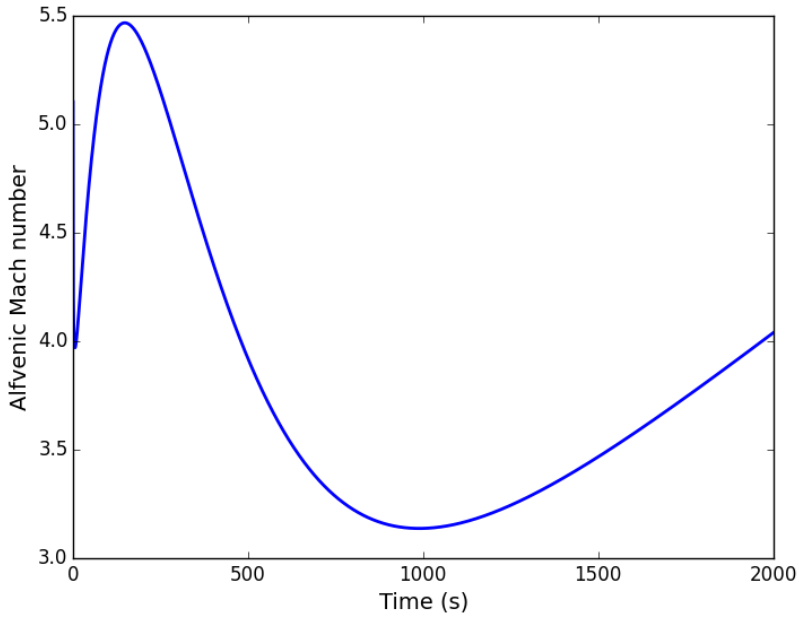

Figure 18: Alfvénic Mach number versus the shock propagation time along the magnetic field line selected for the particle acceleration simulation with CSA.

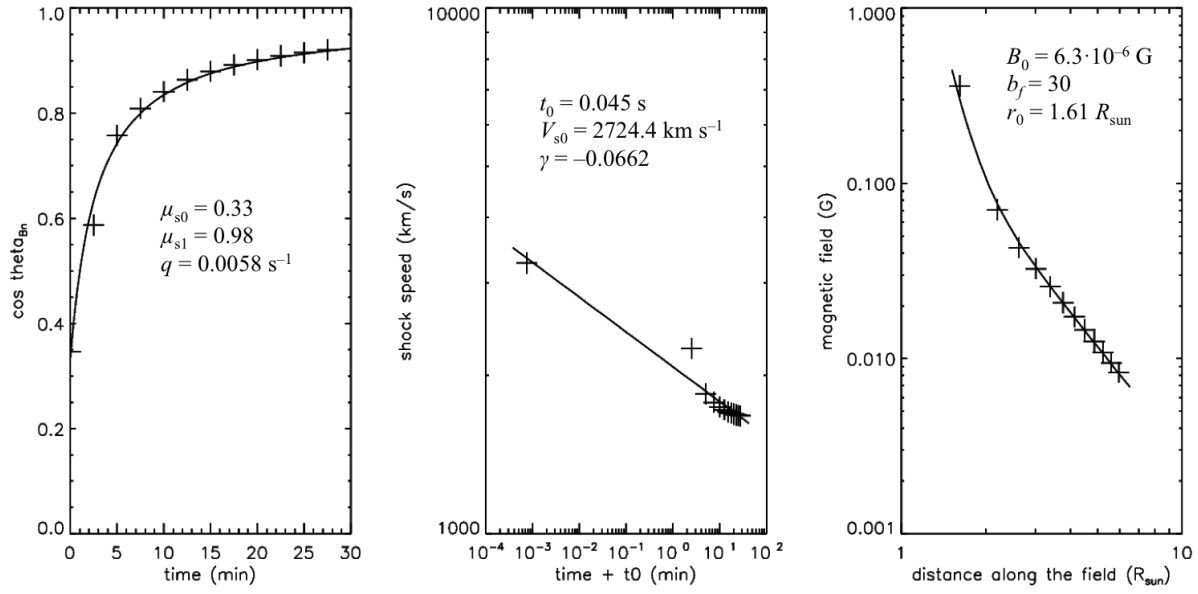

Figure 19: The shock-normal cosine μ_s, the shock speed along the field line $V_{s,||}$ and the magnetic field B with the fits superimposed for the selected magnetic field line.

The development of the accelerated proton population, resulting from the CSA simulation for the selected magnetic field line is presented in Fig. 20. It can be seen that the maximum particle energy (over 1 GeV) is achieved at $\sim$ 1130 seconds from the start of the simulation, and by end of the simulation the maximum energy *at the shock* decreases to $\sim$ 500 MeV.

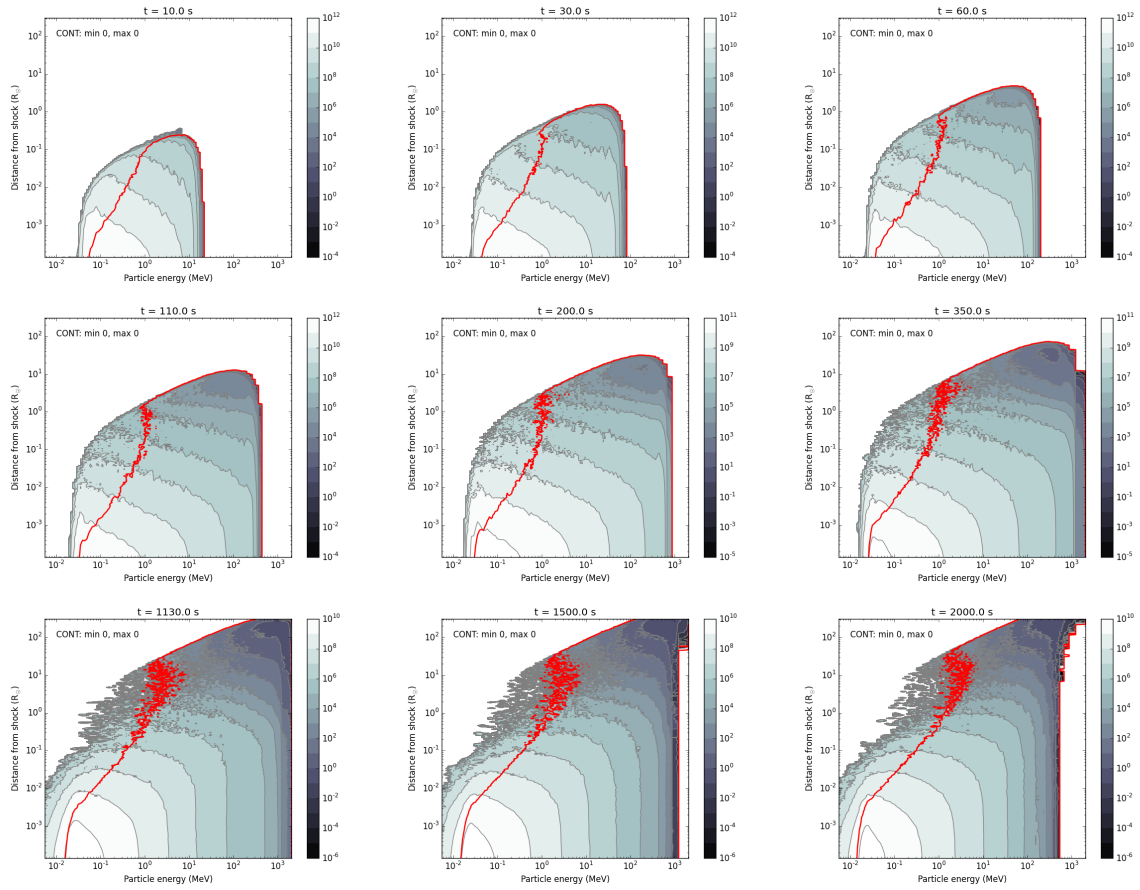

Figure 20: Development of the accelerated proton distribution in the foreshock as obtained in the CSA simulation for the 23 January 2012 event. The contours give the particle intensity in $\mathrm{cm}^{-2}\,\mathrm{sr}^{-1}\,\mathrm{s}^{-1}\,\mathrm{MeV}^{-1}$. The red contour outlines the region in which intensity of the injected/accelerated particles exceeds intensity of the background plasma particles.

4.1.3 Modelling of the proton transport back to the Sun

Figure 21 presents results of simulations of the proton transport back to the Sun with the particle intensities at the shock taken from the CSA simulation. Three simulations have been performed that correspond to different values of the model parameters that affect the particle transport: the proton mean free path at the solar surface λ_0 and the expansion coefficient of the magnetic flux tube b_f (this parameter characterises the flux-tube mirror ratio). One can see that the flux of precipitating particles with energies above 300 MeV decreases by several orders of magnitude within 1 hour and hence the corresponding energy spectrum is almost identical to the injected spectrum (at least for $\lambda_0 > 1.6 R_\odot$). Some extension of the flux in time can be achieved for much shorter λ_0. This immediately affects the energy spectrum of precipitating particles.

Figure 22 shows a simulation of the proton transport back to the Sun, obtained using the G-source function derived from the SaP simulations. In this case, the proton flux (> 300 MeV), after a quick rise, rather slowly decreases within an hour and then falls down abruptly by more than two orders of magnitude, following the G-source function behaviour at high energies.

In the simulations, we computed the number of precipitating protons (> 500 MeV) to compare it with the one available from the observations (see Table 4). This number was computed as follows. First, we counted the actual number N_{sim} of precipitating particles with energies above 500 MeV in a simulation,

where the particle source size (at the shock) is determined by the flux-tube angular size (solid angle) Ω_0 at the solar surface. We took $\Omega = 1\,\mathrm{sr}$. The number of protons to use for comparison with the observed one was obtained by applying a filling factor a: $N_{\mathrm{precip}} = aN_{\mathrm{sim}}$, which accounts for the fact that only a fraction of field lines have favourable conditions for particle acceleration to energies over 500 MeV. We took $a = 10\%$, which agrees with the analysis performed for the 17 May 2012 event, where the acceleration conditions were evaluated for more than 100 individual field lines.

Table 4: The number of precipitating protons with $E > 500\,\mathrm{MeV}$, obtained in simulations for the 23 January 2012 event. The corresponding number derived from the observation of gamma-emission in this event is $N_{\mathrm{obs}} = 0.3 \times 10^{29}$.

b_f	λ_0	CSA	SaP
0	1.6	0.82×10^{32}	0.73×10^{24}
1.5	0.16	0.12×10^{32}	-
3	3.2	0.60×10^{32}	-

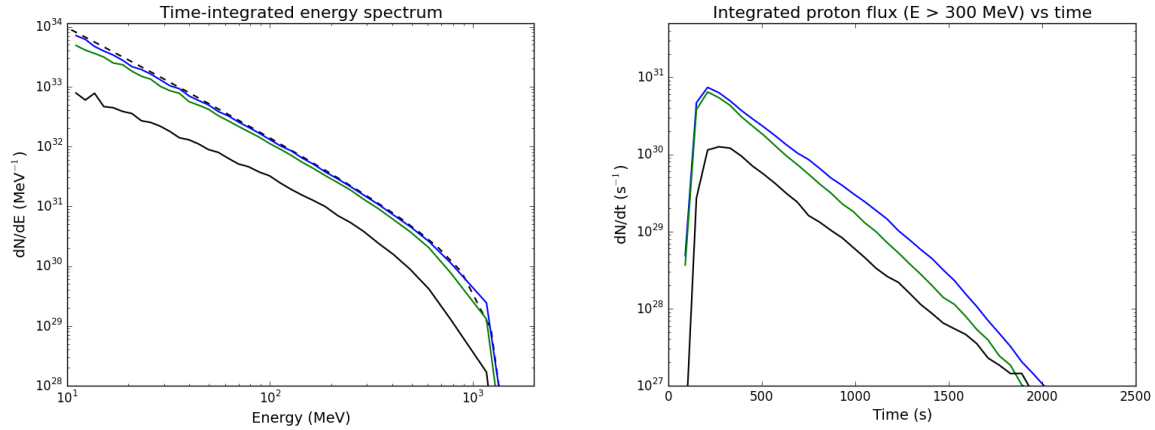

Figure 21: Left panel: Time-integrated energy spectra of protons precipitated at the Sun,resulting from DSP simulations with the particle intensities at the shock provided by CSA (integration was performed over the γ-ray burst duration of 6 hours). The black dashed line shows the event-integrated injected proton spectrum. Right panel: Cross-section integrated fluxes of precipitated protons with $E > 300\,\mathrm{MeV}$. The values of the transport model parameters are $\lambda_0 = 1.6R_\odot$, $b_\mathrm{f} = 0$ (blue lines); $\lambda_0 = 3.2R_\odot$, $b_\mathrm{f} = 3$ (green lines) and $\lambda_0 = 0.16R_\odot$, $b_\mathrm{f} = 1.5$ (black lines).

Table 5: Solar wind initial parameters for the 2012 May 17 event.

Event	ρ_0 [kg/m^3]	T_0 [K]	S_0 [W/m^3]	L [R$_\odot$]	γ	B_{r0} [T]
May12	$1.169 \cdot 10^{-13}$	$1.18 \cdot 10^{6}$	$0.35 \cdot 10^{-7}$	0.70	1.55	$1.26 \cdot 10^{-4}$

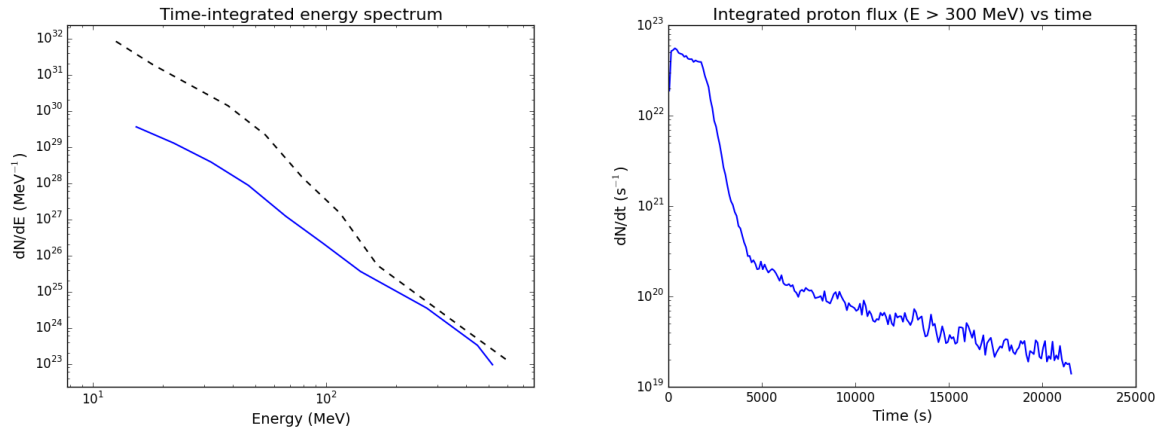

Figure 22: Same as in Fig. 21 but obtained using G-source function from SaP. The values of the transport model parameters in this simulations are $\lambda_0 = 1.6 R_\odot$, $b_f = 0$.

4.2 The 17 May 2012 event

4.2.1 Modelling of the SEP event from the solar corona to the near-Earth space

Simulation of the solar wind and of the IP shock propagation

Table 5 lists the initial input parameters for the solar wind simulation of the 2012 May 17 event that better fit the observed average values of the solar wind plasma variables and magnetic field indicated in Figure 6 by orange traces. Figure 23 shows the resulting heliocentric radial distance profiles for the solar wind density and temperature (top panels), the radial and azimuthal components of the solar wind velocity (middle panels) and for the radial and azimuthal components of the simulated interplanetary magnetic field (bottom panels).

Figure 9 shows that the simulated solar wind (blue curves) reproduces well the observed large scale solar wind conditions (in red for ACE data and in orange for WIND data) for the 40 hours prior to the shock passage. For this event, the transit time of the shock (i.e. the time from the onset of the CME to the shock arrival at WIND) is 72 hours. As can be seen in Figure 9 the simulated shock reproduces the time of the shock arrival, as well as the observed jumps in density, velocity and temperature. However, the magnetic field jump is not reproduced in this case. The main reason for this is the combination of two facts: (i) the near-Earth observer is connected to the right flank of the shock and (ii) the modelled initial disturbance (as described in Section 3.1) does not include any type of flux-rope or magnetic structure that could enhance the magnetic field jump. The initial 'CME' free parameters that better reproduce the time of the shock arrival to 1 AU and the observed plasma jumps are: $\rho_{cme} = 0.3 \times 10^{-13}$ kg m^{-3}, $v_{cme} = 1000$ km s^{-1}, and $\Delta\phi = 0.50 a_{cme}$.

Proceeding as in the previous event, we have extracted from the shock propagation simulation the position of the cobpoint and the shock characteristics at its position. The left panel of Figure 25 shows

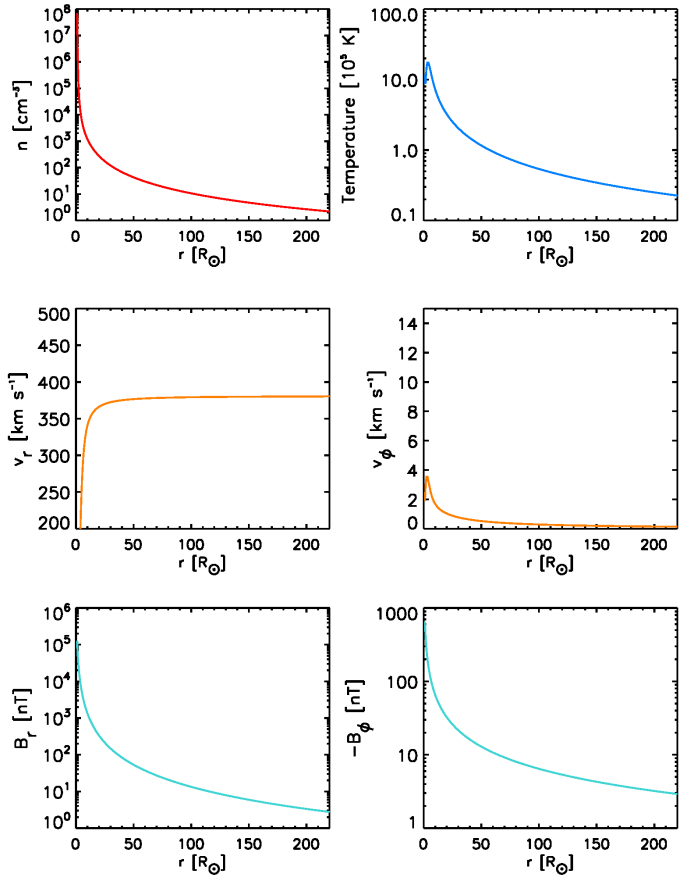

Figure 23: Solar wind plasma variables as a function of the heliocentric radial distance for the 2012 May 17 event.

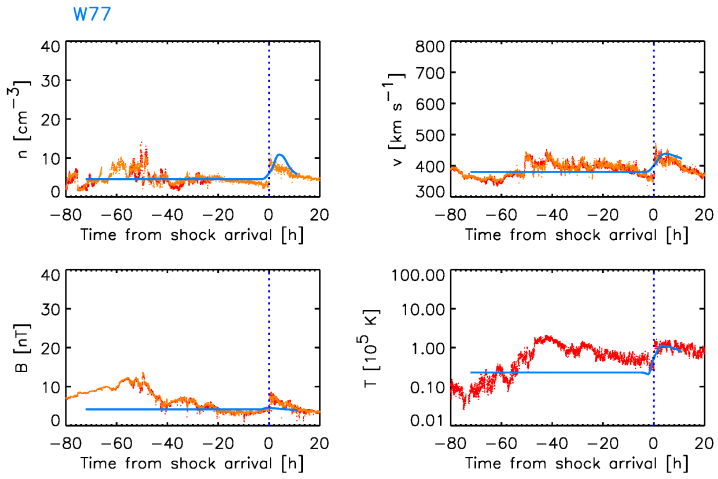

Figure 24: 2012 May 17 event. From left to right, top to bottom: the solar wind density and radial velocity, and the magnetic field strength and the solar wind temperature measured by the ACE spacecraft (red curves) and the WIND spacecraft (orange curves). The corresponding values from the simulation are plotted in blue. Time is counted from the time of the interplanetary shock passage by the WIND spacecraft and it is marked by a dotted vertical line.

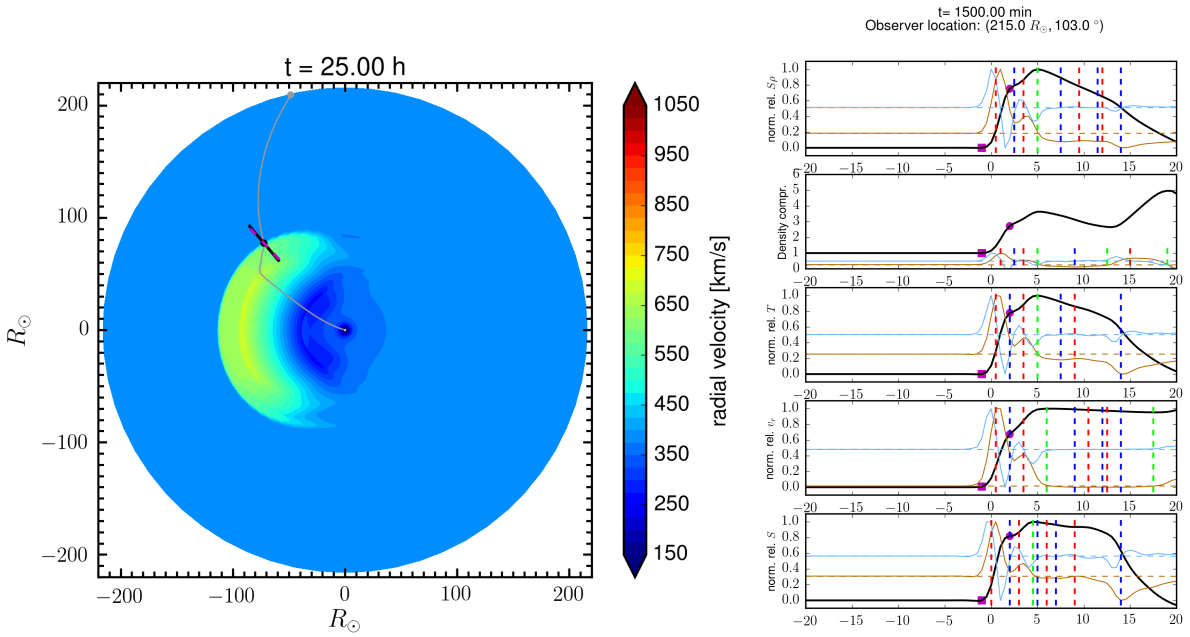

Figure 25: 2012 May 17 event. Left: Contour plot of the plasma radial velocity (color bar) at $t = 25.00$ h. The IMF line crossing the observer's (grey circle) position is indicated in grey. The cobpoint (black circle) and the normal (pink dashed line) and the radial (black line) directions through the cobpoint are also shown. Right (from top to bottom): Values of the normalized relative entropy density, compression ratio, normalized relative temperature, normalized radial velocity and normalized relative entropy along the shock normal for the cobpoint corresponding to the same snapshot. Squares mark the upstream position and circles the downstream location. The X-axis indicates the distance from the cobpoint position in $R_\odot$.

the radial velocity contour plot of the MHD simulation at $t = 25.00$ hours. The near-Earth observer (grey circle) is placed 77° east from the direction of propagation of the shock (towards the negative X-axis, at Y=0). The information shown in this figure follows the same format as in Figure 10. We can see that at this time, the radial and normal directions are slightly different. The right panel of Figure 10 shows the values of different parameters (black solid lines) evaluated along the shock-normal direction through the cobpoint.

Simulation of the particle transport to Earth's orbit

For this event we have fitted the intensity-time profiles shown in Figure 6; that is, the differential intensities for 0.59 – 700 MeV protons. Figures 26, 27 and 28 show the resulting modeled intensity and parallel first-order anisotropy -time profiles (blue sky curves) for the 17 simulated energy channels. Red curves are the corresponding observations. The two vertical solid blue lines indicate the times of the shock arrival to WIND and to GOES. The orange dotted vertical line indicates the onset of the associated X-ray flare. We have subtracted the pre-event background intensities from the the observations, in order to compare observations with the modeled intensity profiles. For each energy, the subtracted intensity levels are indicated by small green horizontal lines. The vertical blue-sky lines mark the time that the highest energy proton of the corresponding energy channel would take to travel from the Sun to the spacecraft position under scatter-free conditions and following the simulated nominal magnetic connection. As can be seen in Figure 26, both the ACE observations and the SEPEM data at the low-energies exhibit contamination from electrons or higher-energy protons. This is also true for the < 55 MeV

channels shown in Figure 27.

The shock-connection time is $t_c = 0.472$ hours and the radial position of this first cobpoint is $r_c = 3.5 R_\odot$. The energy of reference taken to perform the fitting of the intensity-time profiles is the same as for the previous case, $E_0 = 8.7$ MeV and the momentum of reference $p_0 = 128.07$ MeV/c. The proton parallel mean free path modeled increases with the radial distance with the same dependence as simulated for the 2012 January 23 SEP event, but taking the pre-event observed solar wind speed: $v_{sw} = 387$ km s^{-1}. For this event, the values of λ_{r0} that yield a better fitting of the particle intensities and anisotropies are: for $t < 8$ h, $\lambda_{r0} = 0.65$ AU and for $t \geq 8$ h, $\lambda_{r0} = 0.35$ AU.

After we have obtained the evolution of $G(t, E_0)$ by fitting the intensity-time profile at E_0, we simultaneously fit the intensity-time (and first-order anisotropies) profiles for the other energy channels by assuming that G scales with energy as $G(E) = G(E_0)(E/E_0)^{-\gamma}$. Note that although we express here the functionality of G with the particle energy[10], the particle transport code performs the scaling with the momentum of the particles, then given by, $G(p) = G(p_0)(p/p_0)^{-\gamma_p}$. In the case of the May event, the energy spectra evolution is simple:

For $E < 35$ MeV, if $t \leq 4$ hours, $\gamma_p = 5.0$ and if $t > 4$ hours, $\gamma_p = 6.8$

For $E > 35$ MeV and $E < 80$ MeV, $t \leq 3.0$ hours , $\gamma_p = 5.2$ and if $t > 3.0$ hours, $\gamma_p = 6.8$

For $E > 80$ MeV and $E < 120$ MeV, $t \leq 3.0$ hours , $\gamma_p = 5.6$ and if $t > 3.0$ hours, $\gamma_p = 6.8$

For $E > 120$ MeV, $t \leq 2.0$ hours , $\gamma_p = 5.6$ and if $t > 2.0$ hours, $\gamma_p = 6.8$

Figure 29 shows the evolution of G for each of the energy channels modeled, in the same format as for the previous event. In this case, we have applied two polynomial fits for > 35 MeV protons to account for the two clearly differentiated regions in the $G(t)$ profiles.

As can be seen in Figure 29, most of the > 38 MeV protons are injected(accelerated) close to the Sun (event at low-energies) and during the first 4 hours, and the interplanetary shock contribution to the acceleration and injection of these high-energy protons fast decreases after that and becomes negligible when the shock approaches 1 AU. The latter is also true for the lower energies, the values of G decrease fast for the whole energy range, suggesting that the shock was only efficiently injecting particles onto the magnetic flux connected to the Earth at the very beginning of the event. Later on, the shock becomes not efficient at accelerating particles presumably due to the magnetic connection that slides towards the flank of the shock front as it propagates out toward 1 AU. This is clearly seen in the third panel of Figure 30, where the downstream-to-upstream normalised radial velocity ratio, VR (see e.g., Pomoell et al. 2015, for details), decreases fast during the first hour, according to the 2D MHD simulation; suggesting that the shock becomes rapidly weak, for the magnetic connection with the Earth. Note that in the shock propagation simulation, we have assumed that the shock is narrow in the azimuthal direction. The first magnetic connection, predicted by the model is 18° east of the shock nose; therefore if the connection were actually of the Parker spiral type the Earth could be well missing an important part of the protons produced at the shock. Being this narrow a shock, the way the magnetic connection is established with the shock front plays a crucial role in order to estimate the high-energy proton production by the shock. The simulation of a narrow efficient shock front near the equatorial plane, also coincides with the results of the 3D analysis of the shock provided by A. Rouillard (see discussion in the next section).

Output provided for the DSP model

As for the previous event, the UTU-team is provided with the coefficients of the fits (black curves) to the values of G shown in Figure 14 and the range of their applicability together with the first connection

[10]This is a simplification that we usually use because in most of the events modeled in the past the proton energies were not near-relativistic as it is in the case of the last energy channels

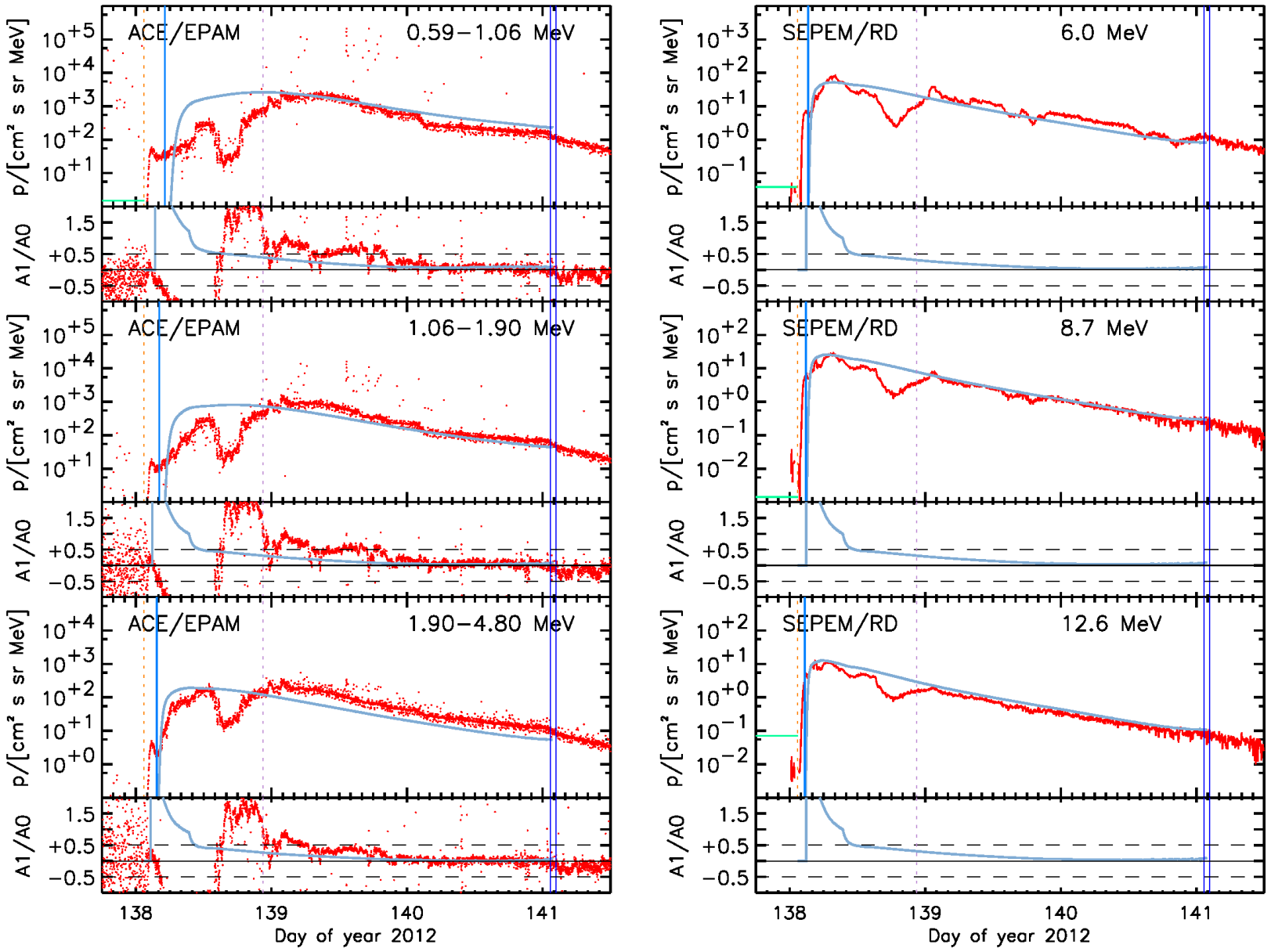

Figure 26: Fitted (blue sky curves) intensity-time profiles and parallel first-order anisotropies (A1/A0) for 0.59 – 12.6 MeV protons. Comparison with ACE/EPAM and SEPEM reference data (red curves).

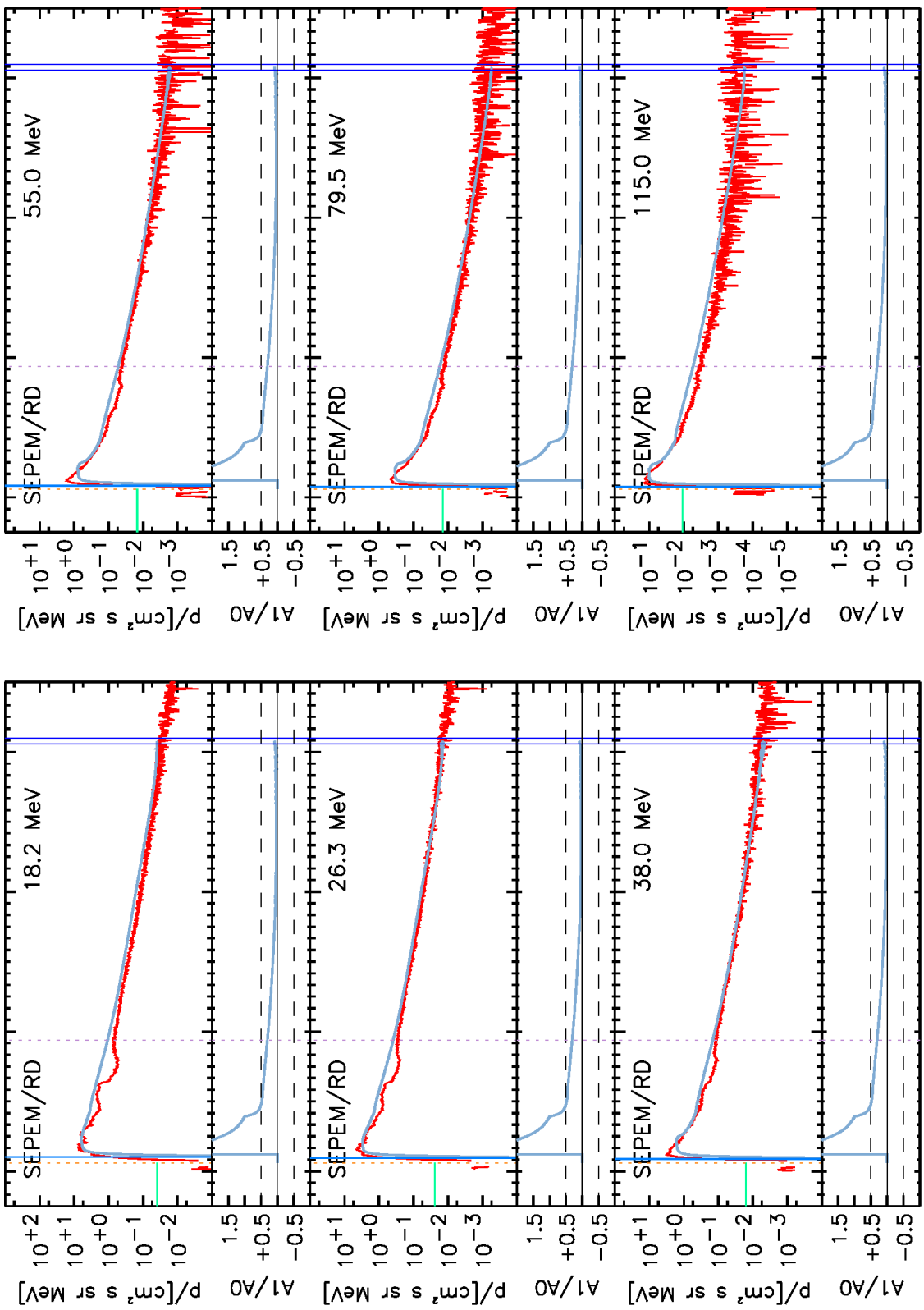

Figure 27: Fitted (blue sky curves) intensity-time profiles and parallel first-order anisotropies (A1/A0) for 18.2 – 115.0 MeV protons. Comparison SEPEM reference data (red curves).

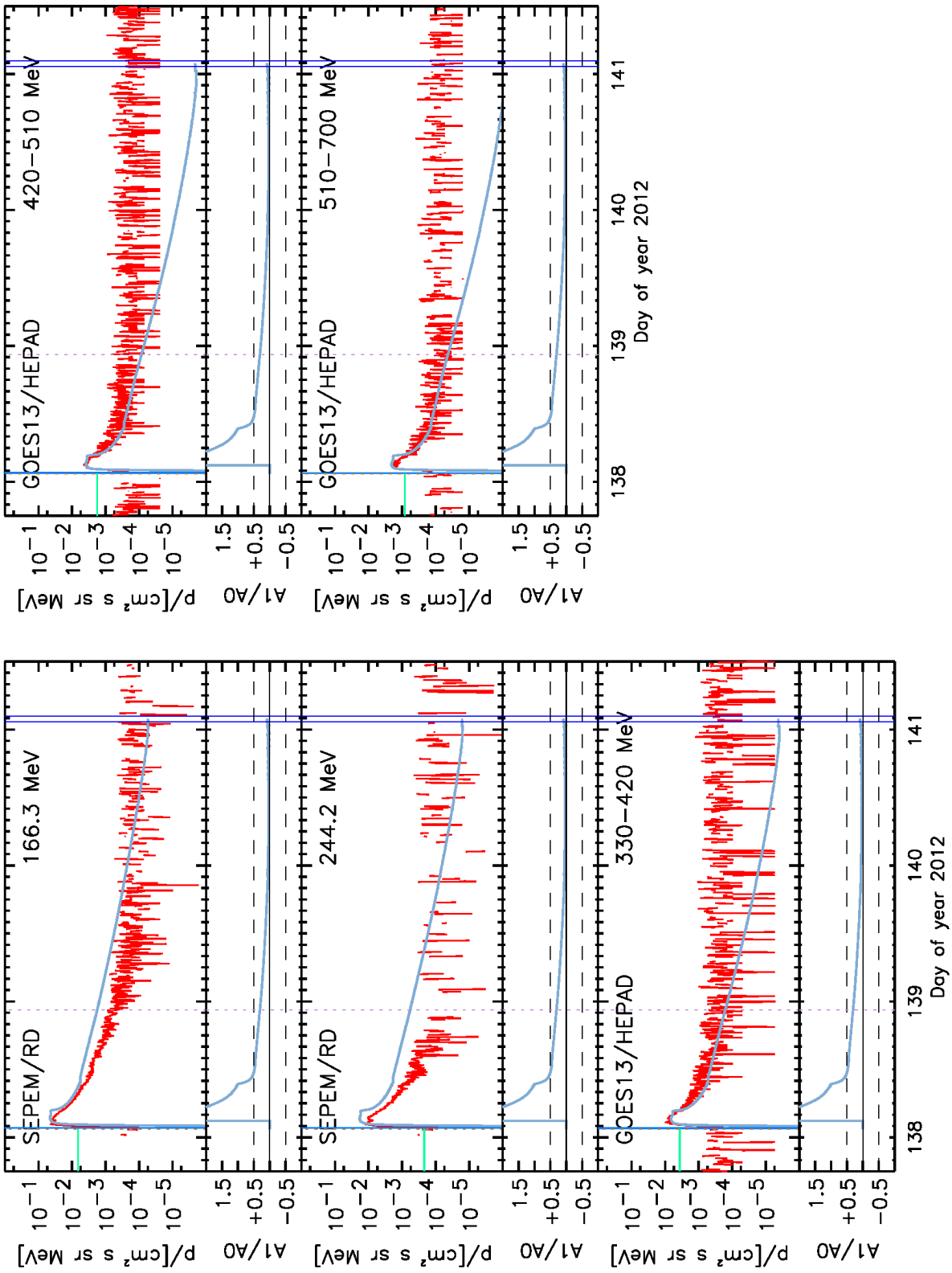

Figure 28: Fitted (blue sky curves) intensity-time profiles and parallel first-order anisotropies (A1/A0) for 166.3 – 700 MeV protons. Comparison with SEPEM reference data and GOES/HEPAD.

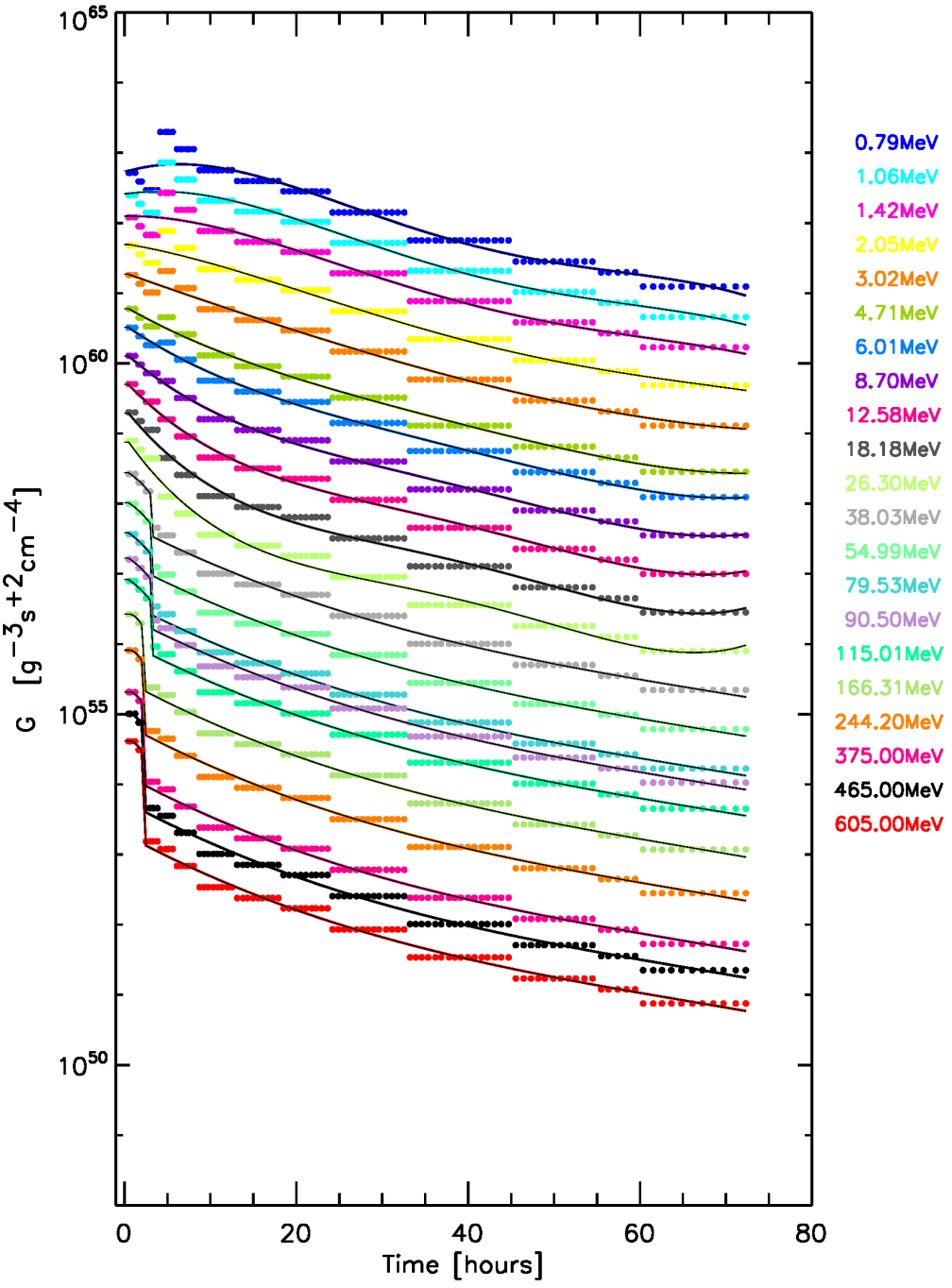

Figure 29: Evolution of the proton injection rate, G, for each simulated energy (color coded). Black lines correspond to the polynomial and linear fits delivered as input to the DSP model.

point, in order to investigate whether up to which extent the shock portion connected to the observer at 1 AU may explain the observed γ-ray emission.

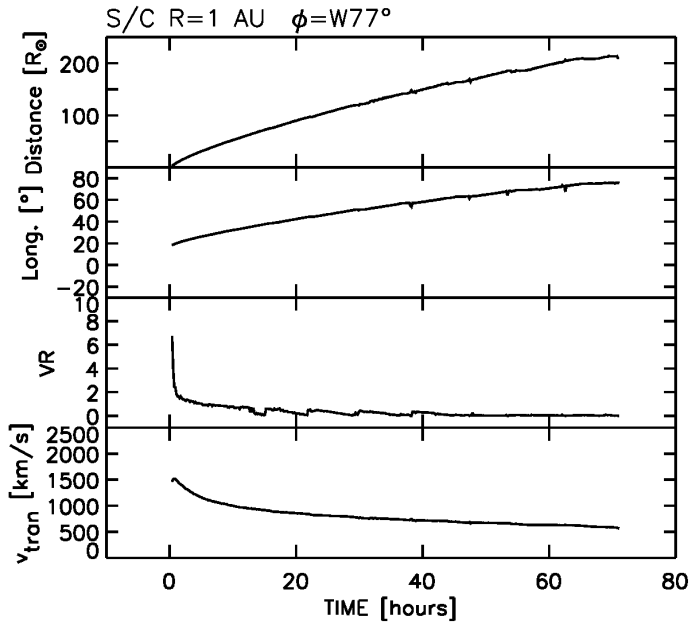

Figure 30: 2012 May 17 event. From top to bottom: evolution of the radial distance of the cobpoint, of its angle with respect to the nose of the shock, the evolution of the VR parameter at the cobpoint location and of the transit speed of the shock to each cobpoint position.

4.2.2 Modelling of proton acceleration in the shock

To carry out CSA simulations of proton acceleration in the 17 May 2012 event, we have used, as input, results of the semi-empirical modelling of the shock in this event (Rouillard et al. 2016). Those results are given in the form of sequences of values of plasma and shock parameters for different heights along individual magnetic field lines that were intersected by the shock during the first hour of the event. The plasma parameters include the magnetic field B and the plasma density n, and the shock parameters include the shock-normal speed $V_{\rm sn}$ and the shock-normal angle $\theta_{\rm Bn}$. In total, the data for 200 field lines were available and were fitted using the functions adopted in CSA. Those are

$$B(r) = B_0 \left(\frac{r_\oplus}{r}\right)^2 \left[1 + b_f \left(\frac{R_\odot}{r}\right)^6\right], \tag{24}$$

for the magnetic field, where $r_\oplus = 1\,AU$, and B_0 and b_f are the fitting parameters;

$$n(r) = n_2 \left(\frac{r_\oplus}{r+r_1}\right)^2 + n_8 \left(\frac{R_\odot}{r+r_1}\right)^8, \tag{25}$$

for the plasma density, where n_2, n_8, and r_1 are the fitting parameters;

$$\mu_{\rm s}(t) = \frac{\mu_{\rm s0} + \mu_{\rm s1}\, qt}{1+qt}, \tag{26}$$

for the shock-normal cosine $\mu_{\rm s} = \cos\theta_{\rm Bn}$, where $\mu_{\rm s0}$, $\mu_{\rm s1}$ and q are fitting parameters; and

$$V_{\rm s}(t) = V_{\rm s0}(t+t_0)^\gamma, \tag{27}$$

for the shock speed along the magnetic field $V_{\rm s} = V_{\rm sn}/\mu_{\rm s}$, where $V_{\rm s0}$, t_0 and γ are the fitting parameters. For further analysis, good-quality fits were selected and divided into 3 classes according to the prevailing Alfvénic Mach number during the first hour of the event: W class ($M_A < 3$) corresponding to weak shocks, M class ($3 < M_A < 7$) corresponding to moderate shocks, and S class ($M_A > 7$) corresponding to strong shocks. Examples of the data sets along with the corresponding fits for the field lines representing each class are shown in Figs. 31-33.

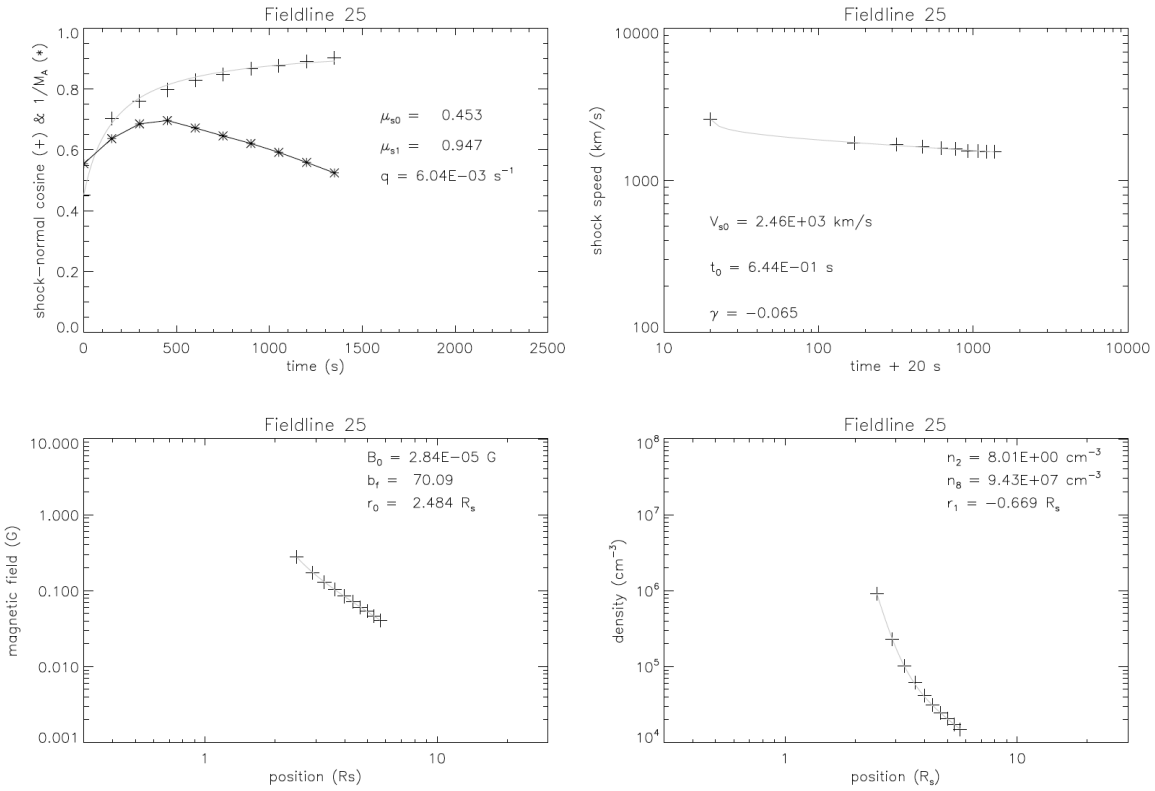

Figure 31: Example data set obtained with the semi-empirical shock modeling approach in the 17 May 2012 event, plotted together with the corresponding fits. The upper left panel shows the shock-normal cosine $\cos(\theta_{\mathrm{Bn}})$ ("plus" symbols) and the inverse Alfvénic Mach number M_{A}^{-1} (asterisks) versus time; the upper right panel shows the shock speed along the magnetic field line V_{S} versus time. Note that time is counted from the moment when $M_{\mathrm{A}} > 1.5$. The bottom left panel shows the magnetic field magnitude B versus radial shock position and the bottom right panel shows plasma density n versus radial shock position. The values of the fitting parameters are indicated at the corresponding panels. According to our classification (see text), this is an example of the W-class field lines as $M_{\mathrm{A}} < 3$.

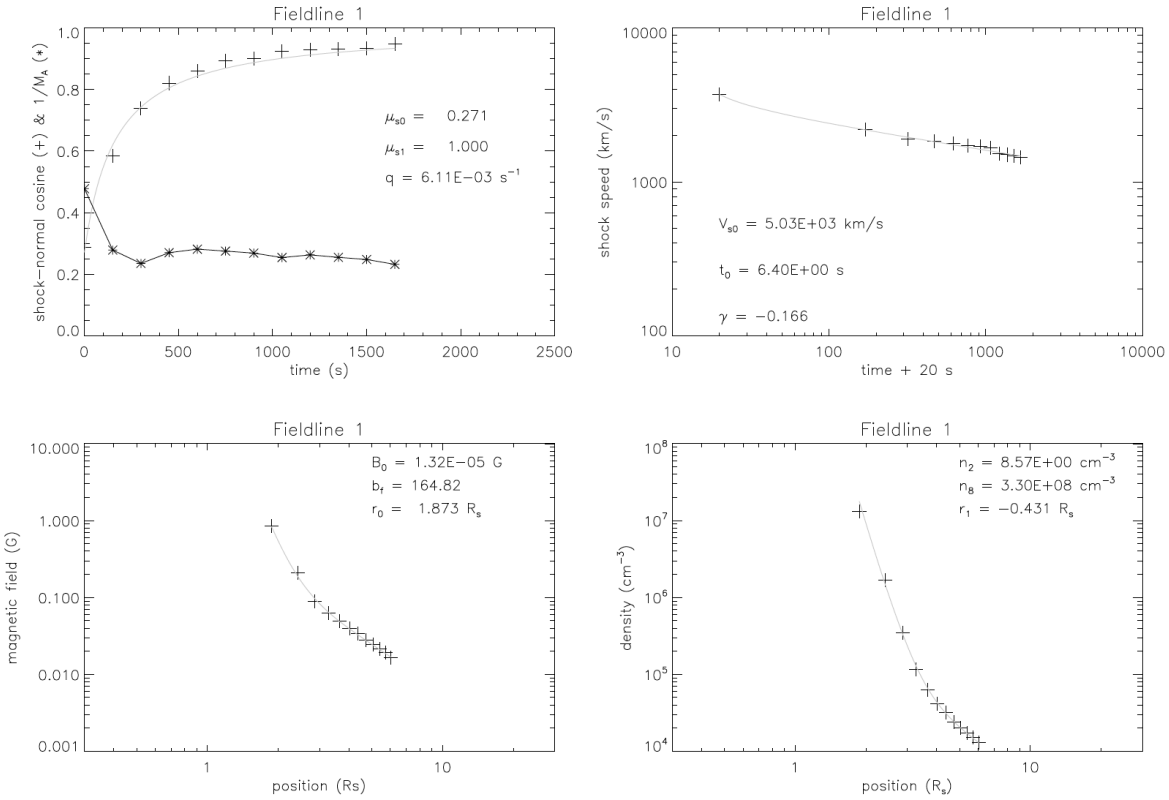

Figure 32: Same as in Fig. 32 but for a field line of the W class as $M_{\rm A} \approx 4$ at $t > 150\,$s.

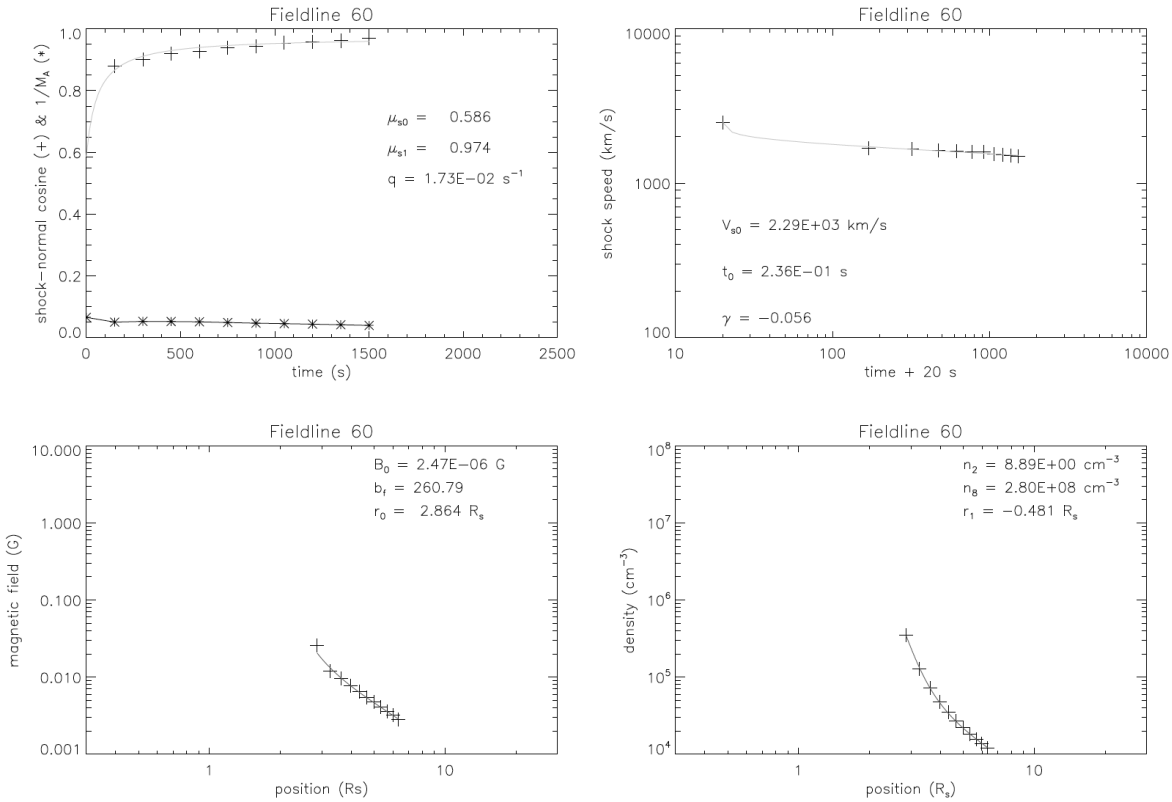

Figure 33: Same as in Fig. 32 but for a field line of the S class as $M_{\rm A} > 7$.

We have selected 9 field lines (3 field lines of each class) having good quality fits, for which we performed CSA simulations. In all the simulations, the seed particle population was modeled by a κ-distribution with $\kappa = 2$, combined with a exponential cut-off energy fixed at $E_{\rm c} = 1\,$MeV. The density of the seed particles was set to 100% of the solar wind density, which corresponds to the assumption that the suprathermals are actually the suprathermal tail of the ambient solar wind. The overview of the simulations is given in Table 6, in which the last three columns provide correspondingly the overall maximum particle energy $E_{\rm max}$ achieved in a simulation, the time $t_{\rm max}$ when the overall maximum energy was achieved, and the difference, $\Delta E_{\rm max} = E_{\rm f,max} - E_{\rm max}$, where $E_{\rm f,max}$ is the maximum particle energy as evaluated at the end of the simulation (note that the maximum particle energy was evaluated every 10 seconds in all carried out simulations). Thus, $\Delta E_{\rm max}$ characterizes the evolution of the spectral cut-off energy at the shock after the overall maximum energy has been reached. It can be seen that the field lines corresponding to stronger shocks are associated with larger particle energies achieved. The negative values of $\Delta E_{\rm max}$ indicate that acceleration efficiency of the shock starts going down at some moment. Figure 34 shows an example of the evolving accelerated proton population in a simulation and Fig. 35 shows three proton energy spectra at the shock, obtained at $t = 2000\,$s, corresponding to the field lines belonging to different classes, i.e. corresponding to different shock strengths. Table 6 and Fig. 35 indicate that only the field lines corresponding to high Mach numbers can contribute to the production of $> 300\,$MeV protons capable of producing γ-emission when precipitating in the chromosphere. For that reason, futher we focused on field lines #60 and #106.

Table 6: Overview of CSA simulations for the 17 May 2012 event. The first column gives the field line number, the second the field line class, the third the simulation time, the forth the starting shock position, the fifth the distance reached by the shock by the end of a simulation, the sixth the overall maximum particle energy achieved in the simulation, the seventh the time when the overall maximum energy was achieved, and the eighth column gives the difference between the maximum particle energy as evaluated at the end of a simulation and the overall maximum energy in the simulation.

#	Class	$t_{\mathrm{sim}}\,(\mathrm{s})$	$r_0\,(R_\odot)$	$r_{\mathrm{max}}\,(R_\odot)$	$E_{\mathrm{max}}\,(\mathrm{MeV})$	$t_{\mathrm{max}}\,(\mathrm{s})$	$\Delta E_{\mathrm{max}}\,(\mathrm{MeV})$
25	W	3600	2.48	10.47	6.2	10	−0.16
72	W	3600	2.83	10.87	17.6	2530	−12.0
27	W	2000	2.43	7.01	31.6	330	−0.8
64	M	2000	2.80	7.27	161.8	2000	0.0
1	M	2000	1.87	6.75	315.2	790	−31.7
5	M	2000	2.62	7.01	317.5	610	−16.1
106	S	2000	2.60	6.94	795.5	940	−2.3
60	S	3600	2.86	10.80	1315.8	3600	0.0
33	S	820	2.20	4.49	1793.6	820	0.0

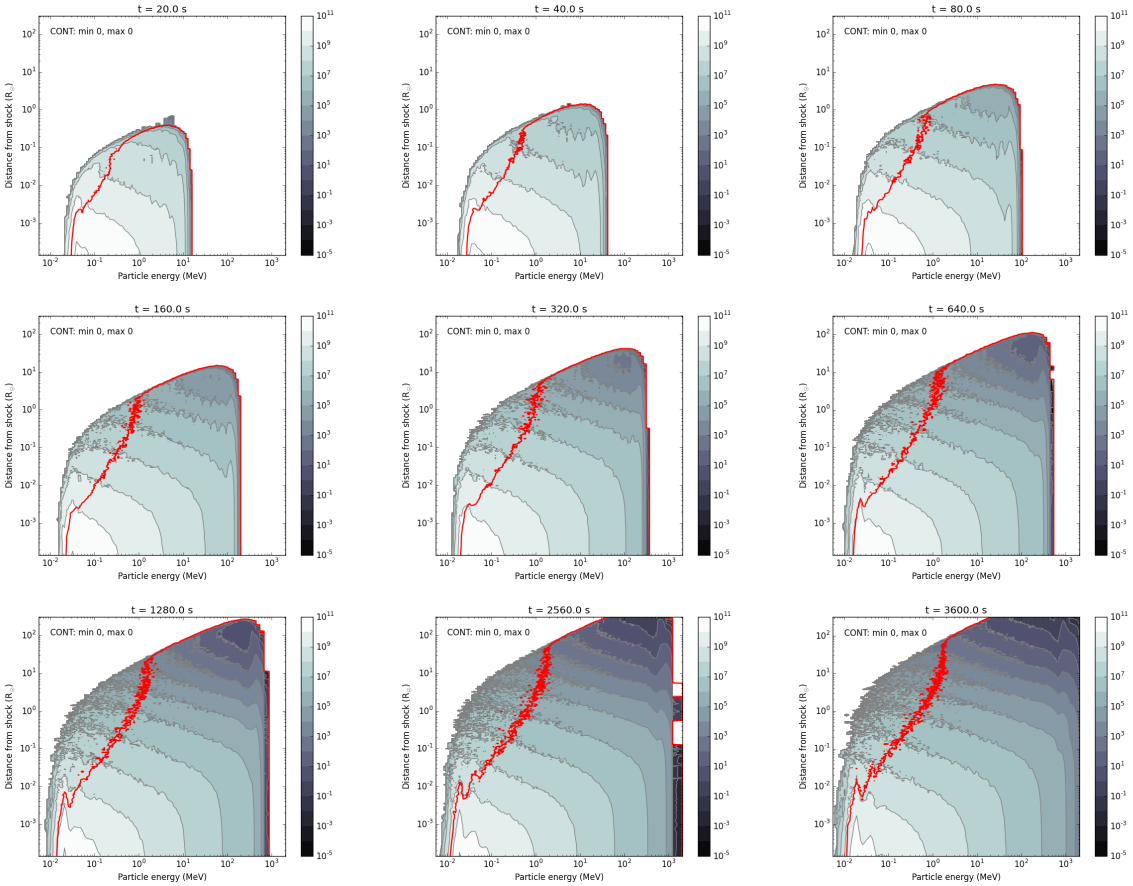

Figure 34: Development of the accelerated proton distribution in the foreshock, as obtained for the plasma and shock parameters along magnetic field line #60, shown in Fig. 33 (c.f. Fig. 20).

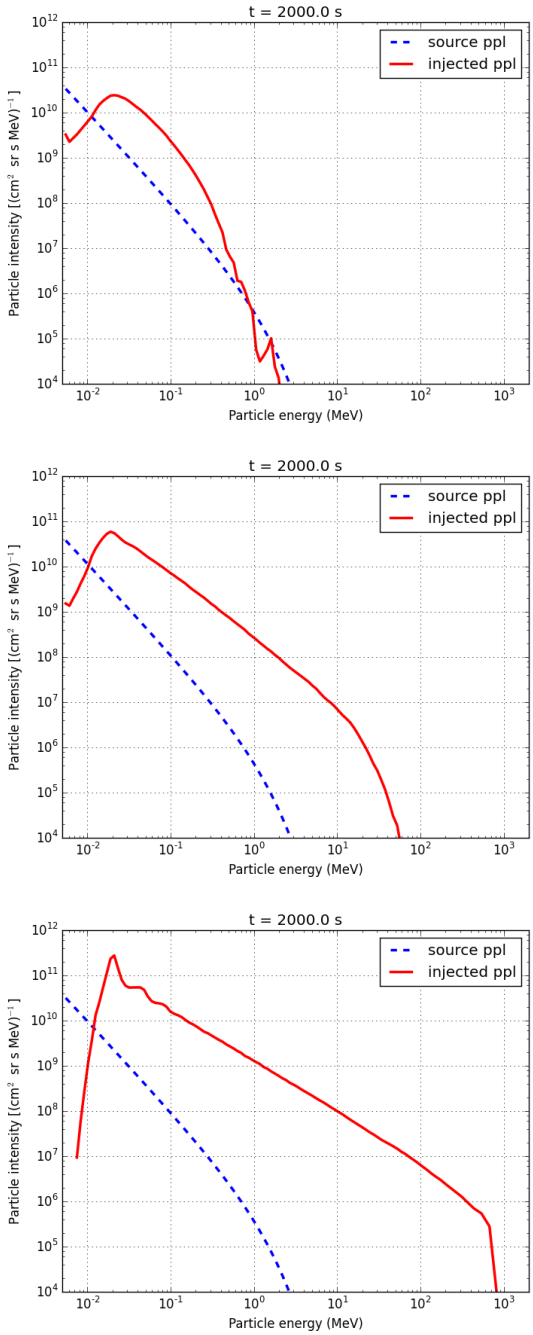

Figure 35: Proton energy spectra (shown in red) as obtained at $t = 2000\,\mathrm{s}$, corresponding to the field lines of different classes (presented in Figs. 31-33): Field line #25 (top), field line #1 (middle), and field line #60 (bottom). The dashed blue lines show the spectrum of the background plasma protons.

4.2.3 Modelling of the proton transport back to the Sun

To simulate the transport of protons from the shock back to the Sun, using DSP code with the input of CSA-modelled particle intensities (particle energy spectra) at the shock, we need to have the intensities during the whole period of γ-emission event, which, in the case of 17 May 2012 event, is about 2 hours. Because the CSA simulations are limited to 2000 and 3600 s in the case of field lines #106 and #60 respectively, we had to extrapolate the CSA-modelled intensities. To make such extrapolations, the CSA

spectra in both cases were presented as functions of momentum p instead of energy E and fitted by the following function:

$$\frac{dJ}{dE} = C\left(\frac{p}{m_{\mathrm{p}}c}\right)^{-q} \exp\left[-\left(\frac{p}{p_{\mathrm{c}}}\right)^{\delta}\right], \tag{28}$$

where the normalisation coefficient C, the cut-off momentum p_{c} and the spectral indices q and δ are the fitting parameters. The whole sequence of spectra was fitted (the spectra are available from $t = 10$ s with the cadence Δt of 10 s). The subsequent inspection of the obtained time dependencies of the fitting parameters (see Figs. 36 and 37) revealed uncertainties in values of the fitting parameters (especially in the δ parameter). These uncertainties were caused by somewhat sparse momentum grid at the highest momenta, which led to significant variations in δ. We found that better results can be achieved if the spectra at later times in the simulations (last 500 s) are fitted by Eq. (28) with fixed δ. The obtained time dependencies of the spectral parameters were then fitted by

$$C(t) = C_0\left(\frac{t}{t_0}\right)^{a_0}, \tag{29}$$

$$q(t) = q_0 + q_1 t, \tag{30}$$

and, in the case of field line #106,

$$p_{\mathrm{c}}(t) = p_0 + p_1 t, \tag{31}$$

and, in the case of field line #60,

$$p_{\mathrm{c}}(t) = p_0\left(\frac{t}{t_{\mathrm{p}}}\right)^{a_{\mathrm{p}}}. \tag{32}$$

Here C_0, t_0, a_0, q_0, q_1, p_0, p_1, t_{p} and a_{p} are the fitting parameters. The fitting results are presented in Fig. 38. The obtained fits of the time series of the spectral parameters were applied together with Eq. (28) to extrapolate the particle intensities beyond the times reached in the CSA simulations.

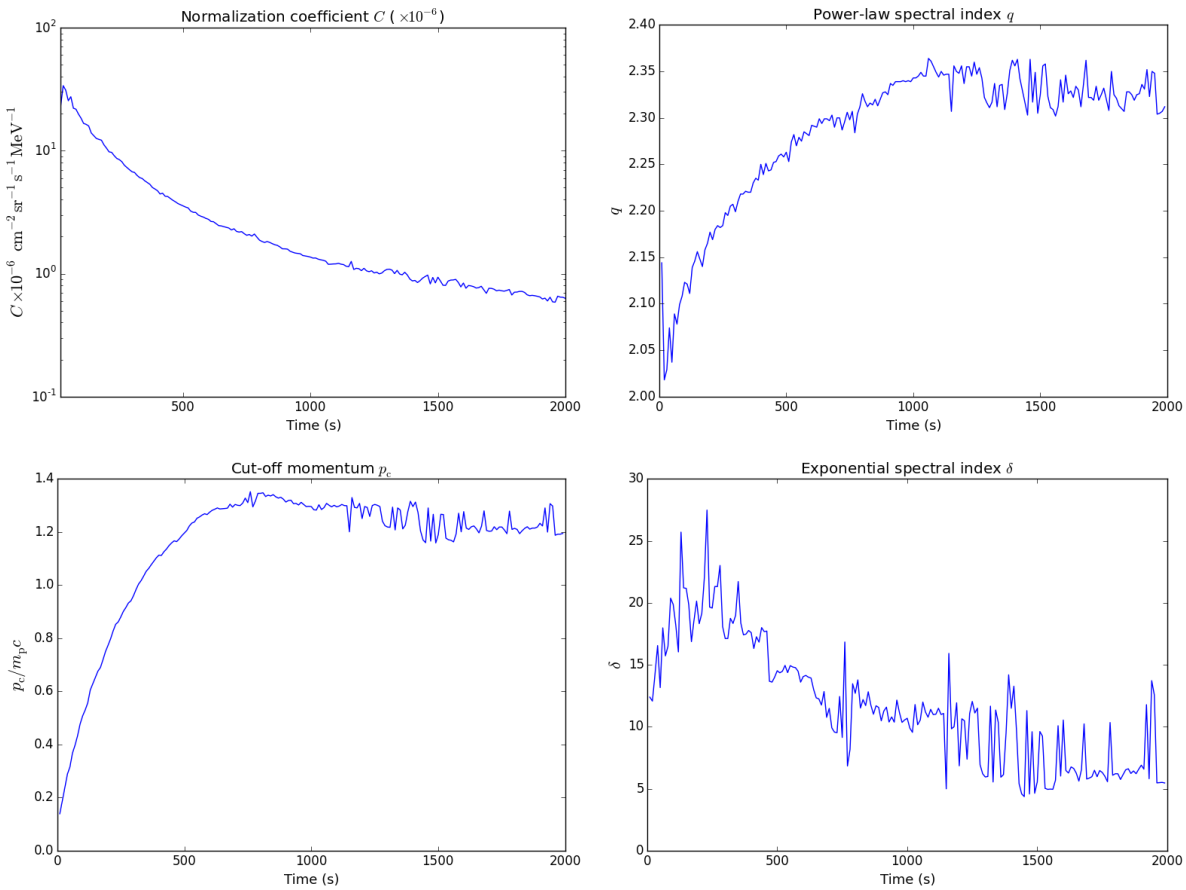

Figure 36: Parameters C, q, p_c and δ versus time obtained by fitting the CSA-modelled energy spectra at the shock, corresponding to field line #106.

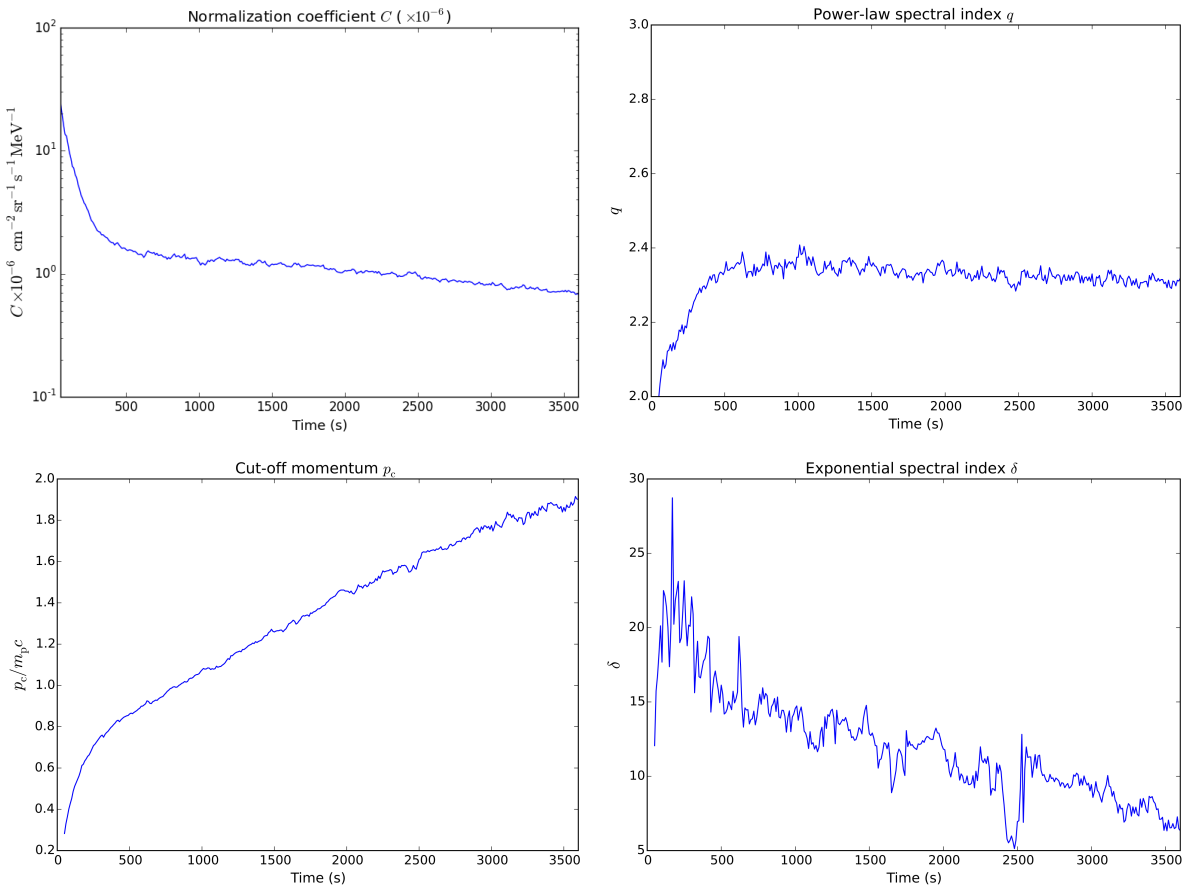

Figure 37: Same as in Fig. 36, but for field line #60.

The particle transport simulations for this event are summarised in Figs. 39 and 40 for the CSA and SaP input, respectively. The numbers of precipitated protons with energies above 500 MeV for different simulations are given in Table 7. It can be seen from Fig. 39 that the radial ($b_f = 0$) magnetic flux tube geometry provides the largest numbers for the precipitated particles and quite stable fluxes for the whole duration of the γ-ray event. This occurs because the shock is efficient in producing the high-energy particles during the whole event and they can be transported back to the Sun rather quickly (the trapping time is short). With a shorter mean free path and/or a super-radial expansion of the flux tube, particles get trapped between the shock and the Sun for longer time especially when the shock is far away from the Sun. Because of the adiabatic cooling, this results in a faster decay of the precipitating high-energy particle flux with time. The total number of precipitated particles decreases as well.

The flux obtained with the SaP-modelled G source functions (Fig. 40) is quite similar to that of the flux simulated with the CSA-modelled particle intensities at the shock for the same values of the transport model parameters. However, the resulting number of precipitated protons (> 500 MeV) differs by several orders of magnitude in these two simulations.

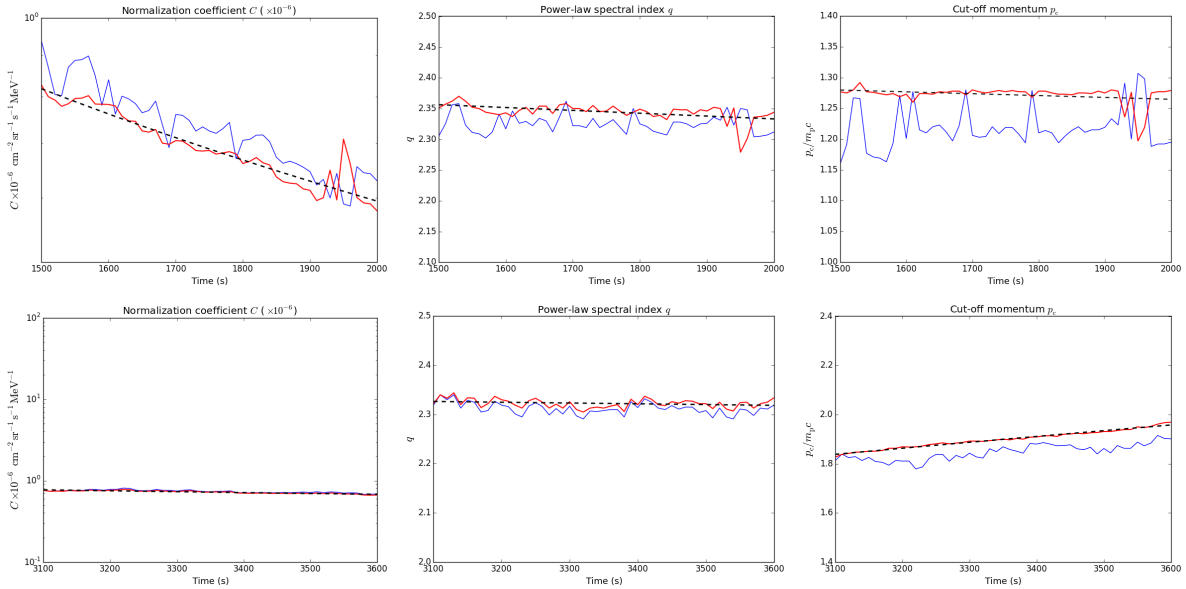

Figure 38: Fitting of the time series (last 500 seconds) of the spectral parameters C, q and p_c, obtained by fitting the particle energy spectra with δ fixed to 10. These time series are shown by red lines. The fits are shown by black dashed lines. The blue lines present, like in Figs. 36 and 37, the time series of the parameters, obtained by fitting the particle energy spectra with δ as one of the fitting parameters. The upper row of plots corresponds to field line #106 and the bottom row of plots corresponds to field line #60.

Table 7: The number of precipitating protons with $E > 500\,\mathrm{MeV}$, obtained in simulations for the 17 May 2012 event, applying the 10% filling factor. The corresponding number derived from the observation of gamma-emission in this event is $N_{\mathrm{obs}} = 0.2 \times 10^{28}$.

b_f	λ_0	CSA	SaP
0	1.6	0.23×10^{32}	0.32×10^{27}
0	0.5	0.71×10^{31}	-
2	1.6	0.11×10^{31}	-
2	0.5	0.27×10^{30}	-

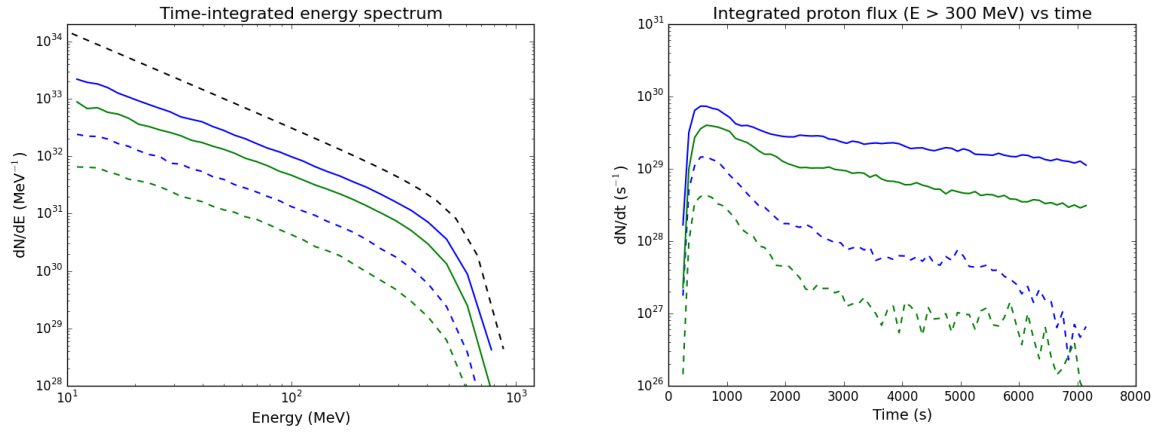

Figure 39: Left panel: Time-integrated energy spectra of protons precipitated at the Sun, resulting from DSP simulations with the particle intensities at the shock provided by CSA for field line #106 (integration was performed over the γ-ray burst duration of 2 hours). Additionally, the time-integrated injection spectrum is shown with black dashed line. Right panel: Flux-tube-cross-section-integrated fluxes of precipitated protons with $E > 300\,\mathrm{MeV}$. The values of the transport model parameters are $\lambda_0 = 1.6 R_\odot$, $b_\mathrm{f} = 0$ (blue solid line); $\lambda_0 = 1.6 R_\odot$, $b_\mathrm{f} = 2$ (blue dashed line); $\lambda_0 = 0.5 R_\odot$, $b_\mathrm{f} = 0$ (green solid line) and $\lambda_0 = 0.5 R_\odot$, $b_\mathrm{f} = 2$ (green dashed line).

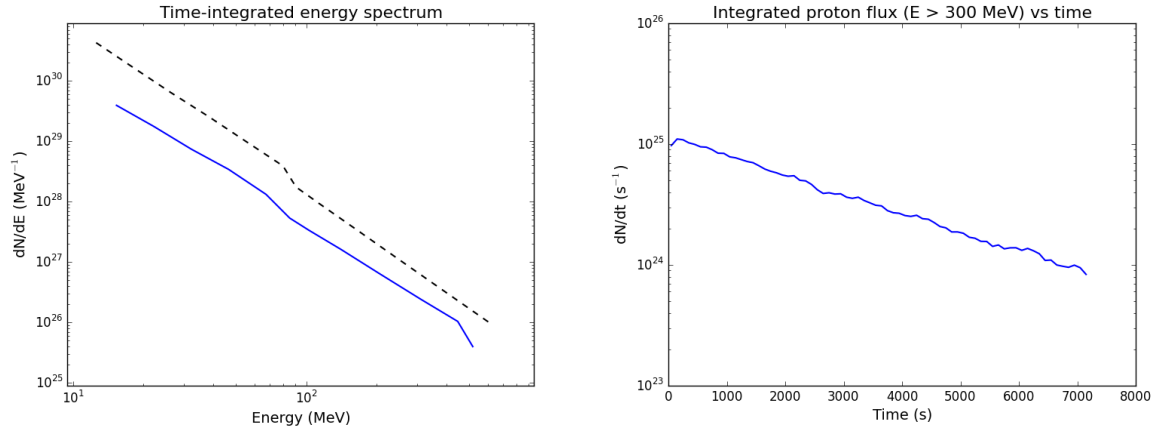

Figure 40: Same as in Fig. 39 but obtained using G-source function from SaP. The values of the transport model parameters in this simulations are $\lambda_0 = 1.6 R_\odot$ and $b_\mathrm{f} = 0$.

5 Discussion and Conclusions

We have modelled particle acceleration at coronal shocks driven by CMEs and proton transport from the shock to the far upstream (towards the 1-AU observer) and to the Sun. The purpose of our study is to find out, whether shock-accelerated protons streaming back from the shock could be responsible for the long-duration gamma-ray events observed by FERMI/LAT. We simulated the shock propagation from the Sun to 1 AU using a two-dimensional MHD model. We also employed the empirical models of the CME-driven pressure front propagation, which allowed us to assess the early evolution of the shock in a system, which does not possess the symmetries assumed in the MHD model.

Our results clearly show that shock acceleration efficiency crucially depends on the modelled proper-

ties of the shock in the corona. Conditions on different field lines vary a lot and while the shock on some field lines is able to produce a relativistic particle event, it fails to do so on others. The most important factor governing the acceleration efficiency in our study was the Mach number of the shock: the higher the Mach number, the more likely is the shock to accelerate protons to relativistic energies.

In our simulations, we focused on two events, which differed in one important aspect: one of them (17 May 2012) was a GLE and the other one was not. Both of the events still showed long-duration gamma-ray events, which might seem contradictory, but actually is not. In the light of our simulations, there are two possible explanations for this: firstly, as the acceleration efficiency of the shock varies a lot from one flux tube to the other, the 1-AU proton event does not necessarily correspond to the best acceleration conditions on the shock surface. Thus, we may well observe a long-duration (pion-decay) gamma-ray event due to shock-accelerated protons without a clear increase observed at 1 AU at energies required for pion production at the Sun. The Earth-based observer sees but a small fraction of the complete picture. Another, more subtle explanation deals with the strength of the turbulence in the foreshock region of the coronal shock. The CSA simulations show that the foreshock is extremely turbulent near the Sun, traps a large fraction (close to all) particles in its vicinity and allows only a minor fraction to escape. While the SaP model contains the possibility to use enhanced foreshock turbulence, it is tuned to reproduce the strength of the observations when the shock crosses observer. Therefore, the source function deduced from the 1-AU observation represents more the fraction of particles that can escape upstream than the fraction that can be transported downstream from the shock. The large discrepancy (several orders of magnitude) between the CSA and SaP modelled numbers of precipitating particles is, thus, partly explained by this effect, as well.

We also note that our estimate of the high-energy proton flux emitted towards 1 AU for the 23 January 2012 event is relying on the extrapolation of the spectrum from below 166 MeV to higher energies, using the SEPEM reference dataset. However, the predicted flux at 1 AU falls well below the values observed in the GOES/HEPAD channels, albeit these would seem to be at or close to background levels, especially at energies above 500 MeV. This implies that if the spectrum at the higher energies would not be quite as steep as the highest energy channels of the SEPEM reference dataset imply, there would be room for some quite substantial increase of the modelled intensities at the HEPAD energies, especially at longer times after the flare. Assuming a harder spectrum than what was deduced here could probably bring the number of precipitated protons up by an order of magnitude, or two, but it would still be several orders of magnitude lower the observed one. Thus, even if the event was fitted more aggressively towards the upper limits set by HEPAD, the main conclusion would still be that the numbers we observe at 1 AU would not be consistent with the Fermi/LAT event, if the same part of the coronal/interplanetary shock is the source of both populations. We suggest that the main reason for the discrepancy is provided by the highly variable shock acceleration conditions at the global coronal shock surface.

The transport model we employ for the downstream plasma has several important simplifications in it. Firstly, it employs a shock completely opaque to protons and, thus, allows downstream-advected particles to reside in the region between the shock and the Sun for as long as they get precipitated. The only loss process we employ is adiabatic cooling of the distribution, when the region between the shock and the Sun expands. On the other hand, we do not include any downstream re-acceleration processes, which could also be important and would act in the opposite direction, helping particles to overcome adiabatic energy losses. Such processes include downstream stochastic acceleration (e.g., Afanasiev et al. 2014) and compressive acceleration in the highly-compressed regions close to the CME core (Kozarev et al. 2013). Therefore, we do not regard our model to be overly optimistic about the prospect of letting shock-accelerated protons precipitate over large time scales.

Regarding the CSA modelling of shock acceleration, one important reservation has to be made: the code makes a simplification to the quasi-linear resonance condition between particles and scattering Alfén waves, $k_{\rm res} = B/(R\mu)$ neglecting the dependence of resonant wave number on particle pitch-angle cosine μ. This simplification, while without proper physical justification, allows one to build the code using the assumption of isotropic scattering, which speeds up the running times easily by a factor of

ten over times obtained when treating the resonance condition in full. We have, however, evaluated the effect of this simplification in HESPERIA Work Package (WP) 6, and shown that in parallel coronal shocks the difference between the two models yields about a factor of 2 in the roll-over rigidity obtained from the model (Afanasiev et al. 2015). On the other hand, the spectrum in CSA also cuts off much more rapidly than in the model employing the complete resonance condition, so we do not regard this to be a very serious problem in the performed modelling. A more complete model to be developed in future, however, should take the full resonance condition into account, also since it affects the foreshock spatial structure as well (Afanasiev et al. 2015). We will undertake the development of such a model in future projects.

Another transport process missing from the CSA model is diffusion perpendicular to the mean magnetic field. This process is easy to implement in a Monte Carlo simulation, but its inclusion will make the addition of two additional spatial dimensions necessary in the model. Therefore, also the requirement for particle statistics in CSA will be tremendously increased to avoid statistical noise in the result, as the number of spatial cells in the model will have to be increased by a factor 100–1000, depending on the coarseness of the grid in the perpendicular direction. This is still beyond the reach of the present computers with reasonable running times of the code. Fortunately, as perpendicular diffusion cannot occur due to slab-mode waves (waves with wave-vectors parallel to the mean field), the enhanced Alfvénic turbulence in the upstream region is not contributing to the perpendicular diffusion of the particles. However, one would expect the downstream plasma to have much more isotropic turbulence which, then, would lead to the migration of particles from one flux tube to the other while they are on the downstream side of the shock. For an opaque shock, like we have assumed, this is not affecting the acceleration of ions at the shock too much since their fate (scattered back to the shock or transported to the far downstream region with no return) would be decided (almost) instantly, giving the particles very little time to diffuse perpendicular to the mean field. Thus, the first step to take the perpendicular transport into account would have to be performed on the downstream side of the shock. This would, actually, most likely facilitate the precipitation of the ions as they could be able to find their way to flux tubes with low mirror ratio.

We note that the total number of >500-MeV protons as simulated by the CSA code is about three orders of magnitude larger than the observational value in both cases we simulated. At first, this might seem to be problematic. However, in addition to the caveats about the resonance condition and the downstream transport modelling discussed above, we point out that the CSA model is set up quite favourably for efficient particle acceleration: we use a seed particle population with a relatively hard suprathermal distribution ($\kappa = 2$) in the model, which guarantees an efficient injection to the acceleration process at all obliquity angles of the shock. Using a thermal population, only, would limit the injection efficiency of the shock especially at obliquity angles greater than $\sim 20^\circ$ quite substantially: according to Battarbee et al. (2013), the injection efficiency in an oblique coronal shock would go down by an order of magnitude if we would use a steeper seed population with $\kappa = 15$. Given all the possible ways to limit the number of precipitating protons in our model, we would regard the result of getting more than enough high-energy protons precipitating at the Sun to be a supporting rather than a countering result for the shock acceleration scenario.

The final shortcoming in the shock models we have employed is their assumption of the open topology of the upstream magnetic fields. Especially if the gamma-ray event occurs during a period of closely spaced CMEs, the second one may drive a shock through a set of large closed loop-like or flux-rope structures, which would alter both the shock acceleration properties and, more importantly, the ability of the particles to escape upstream from the shock. It could also provide an alternative transport scenario in the downstream region, which might be able to overcome the difficulties we have in modelling very long duration gamma-ray events with the present model, as demonstrated by the shorter than observed duration of the modelled 23 January 2012 event. In fact, developing codes capable of modelling particle acceleration and transport in more complicated upstream fields than the radial/Archimedean-spiral fields could be listed as one of the most urgent things needing improvement on the way towards physical space-

weather modelling capabilities.

One of the most difficult things to estimate is the size of the source of near-relativistic protons in the event. While the 3-D modelling of the shock front can be performed in a relatively accurate and detailed manner, high-resolution density and magnetic-field structure of the corona are crucial for the correct determination of the shock properties and, thus, the total number of interacting protons in the event. Therefore, even a fully global 3-D model of coronal shock evolution and particle acceleration might not capture every detail affecting the total number of relativistic protons in the CME system. In this work, we resorted to estimating numbers based on the filling factor of field lines being capable of facilitating proton acceleration to relativistic energies based on an evaluation of shock properties on a large set of field lines. We believe that such statistical method to estimate the total number of interacting protons is the most efficient way to attack the problem.

In conclusion, while the modelling performed in this WP has many caveats, we have still demonstrated that coronal shock acceleration and subsequent diffusive downstream particle transport is a viable option to explain pion-decay gamma-ray events from the Sun observed by FERMI/LAT. Further work on the topic is still needed but our results are motivating this work by indicating that the end result of this vast modelling effort can be positive.

Bibliography

Ackermann, M., Ajello, M., Albert, A., et al. 2014, ApJ, 787, 15

Afanasiev, A., Battarbee, M., & Vainio, R. 2015, A&A, 584, A81

Afanasiev, A., Vainio, R., & Kocharov, L. 2014, ApJ, 790, 36

Aran, A., Jacobs, C., Rodríguez-Gasén, R., Sanahuja, B., & Poedts, S. 2011, SEPEM Technical Report, ESA/ESTEC Contract 20162/06/NL/JD, available at http://www.am.ub.es/ blai/publications.html, 1

Aran, A., Lario, D., Sanahuja, B., et al. 2007, A&A, 469, 1123

Aran, A., Sanahuja, B., & Lario, D. 2006, Advances in Space Research, 37, 1240

Atwood, W. B., Abdo, A. A., Ackermann, M., et al. 2009, ApJ, 697, 1071

Battarbee, M. 2013, PhD thesis, University of Turku, Finland

Battarbee, M., Laitinen, T., & Vainio, R. 2011, A&A, 535, A34

Battarbee, M., Vainio, R., Laitinen, T., & Hietala, H. 2013, A&A, 558, A110

Crosby, N., Heynderickx, D., Jiggens, P., et al. 2015, Space Weather, 13, 406

Gold, R. E., Krimigis, S. M., Hawkins, III, S. E., et al. 1998, Space Sci. Rev., 86, 541

Hasselmann, K. & Wibberenz, G. 1970, ApJ, 162, 1049

Heras, A. M., Sanahuja, B., Lario, D., et al. 1995, ApJ, 445, 497

Heras, A. M., Sanahuja, B., Smith, Z. K., Detman, T., & Dryer, M. 1992, ApJ, 391, 359

Jiggens, P. T. A., Gabriel, S. B., Heynderickx, D., et al. 2012, IEEE Transactions on Nuclear Science, 59, 1066

Jones, F. C. & Ellison, D. C. 1991, Space Sci. Rev., 58, 259

Kozarev, K. A., Evans, R. M., Schwadron, N. A., et al. 2013, ApJ, 778, 43

Kunow, H., Wibberenz, G., Green, G., Müller-Mellin, R., & Kallenrode, M.-B. 1991, Energetic Particles in the Inner Solar System, ed. R. Schwenn & E. Marsch, 152

Lario, D., Decker, R. B., Roelof, E. C., Reisenfeld, D. B., & Sanderson, T. R. 2004, Journal of Geophysical Research (Space Physics), 109, A01107

Lario, D., Sanahuja, B., & Heras, A. M. 1998, ApJ, 509, 415

McComas, D. J., Bame, S. J., Barker, P., et al. 1998, Space Sci. Rev., 86, 563

Ogilvie, K. W., Chornay, D. J., Fritzenreiter, R. J., et al. 1995, Space Sci. Rev., 71, 55

Pomoell, J., Aran, A., Jacobs, C., et al. 2015, Journal of Space Weather and Space Climate, 5, A12

Pomoell, J. & Vainio, R. 2012, ApJ, 745, 151

Rodríguez-Gasén, R., Aran, A., Sanahuja, B., Jacobs, C., & Poedts, S. 2011, Advances in Space Research, 47, 2140

Rodríguez-Gasén, R., Aran, A., Sanahuja, B., Jacobs, C., & Poedts, S. 2014, Sol. Phys., 289, 1745

Rouillard, A. P., Plotnikov, I., Pinto, R. F., et al. 2016, ArXiv e-prints

Sanderson, T. R., Reinhard, R., van Nes, P., & Wenzel, K.-P. 1985, J. Geophys. Res., 90, 19

Sellers, F. B. & Hanser, F. A. 1996, in Proc. SPIE, Vol. 2812, GOES-8 and Beyond, ed. E. R. Washwell, 353–364

Smith, C. W., L'Heureux, J., Ness, N. F., et al. 1998, Space Sci. Rev., 86, 613

Torsti, J., Valtonen, E., Lumme, M., et al. 1995, Sol. Phys., 162, 505

Vainio, R. & Laitinen, T. 2007, ApJ, 658, 622

Vainio, R. & Laitinen, T. 2008, Journal of Atmospheric and Solar-Terrestrial Physics, 70, 467

Vainio, R., Pönni, A., Battarbee, M., et al. 2014, Journal of Space Weather and Space Climate, 4, A8

Wu, S. T., Dryer, M., & Han, S. M. 1983, Sol. Phys., 84, 395